

3-22-2012

# Design and Characterization of a Three-Dimensional Positron Annihilation Spectroscopy System Using a Low-Energy Positron Beam

Stephen M. Jimenez

Follow this and additional works at: <https://scholar.afit.edu/etd>

Part of the [Nuclear Commons](#)

---

## Recommended Citation

Jimenez, Stephen M., "Design and Characterization of a Three-Dimensional Positron Annihilation Spectroscopy System Using a Low-Energy Positron Beam" (2012). *Theses and Dissertations*. 1178.  
<https://scholar.afit.edu/etd/1178>

This Thesis is brought to you for free and open access by the Student Graduate Works at AFIT Scholar. It has been accepted for inclusion in Theses and Dissertations by an authorized administrator of AFIT Scholar. For more information, please contact [richard.mansfield@afit.edu](mailto:richard.mansfield@afit.edu).



**DESIGN AND CHARACTERIZATION OF A THREE-DIMENESIONAL  
POSITRON ANNIHILATION SPECTROSCOPY SYSTEM USING A  
LOW-ENERGY POSITRON BEAM**

THESIS

Stephen M. Jiménez, Captain, USAF  
AFIT/NUCL/ENP/12-M04

**DEPARTMENT OF THE AIR FORCE  
AIR UNIVERSITY**

**AIR FORCE INSTITUTE OF TECHNOLOGY**

**Wright-Patterson Air Force Base, Ohio**

DISTRIBUTION STATEMENT A  
APPROVED FOR PUBLIC RELEASE; DISTRIBUTION UNLIMITED.

## Report Documentation Page

*Form Approved*  
OMB No. 0704-0188

Public reporting burden for the collection of information is estimated to average 1 hour per response, including the time for reviewing instructions, searching existing data sources, gathering and maintaining the data needed, and completing and reviewing the collection of information. Send comments regarding this burden estimate or any other aspect of this collection of information, including suggestions for reducing this burden, to Washington Headquarters Services, Directorate for Information Operations and Reports, 1215 Jefferson Davis Highway, Suite 1204, Arlington VA 22202-4302. Respondents should be aware that notwithstanding any other provision of law, no person shall be subject to a penalty for failing to comply with a collection of information if it does not display a currently valid OMB control number.

1. REPORT DATE <b>22 MAR 2012</b>	2. REPORT TYPE	3. DATES COVERED	
4. TITLE AND SUBTITLE <b>Design and Characterization of a Three-Dimensional Positron Annihilation Spectroscopy System Using a Low-Energy Positron Beam</b>		5a. CONTRACT NUMBER	
		5b. GRANT NUMBER	
		5c. PROGRAM ELEMENT NUMBER	
6. AUTHOR(S) <b>Stephen Jimenez</b>		5d. PROJECT NUMBER	
		5e. TASK NUMBER	
		5f. WORK UNIT NUMBER	
7. PERFORMING ORGANIZATION NAME(S) AND ADDRESS(ES) <b>Air Force Institute of Technology, Graduate School of Engineering and Management (AFIT/EN), 2950 Hobson Way, Wright-Patterson AFB, OH, 45433-7765</b>		8. PERFORMING ORGANIZATION REPORT NUMBER <b>AFIT/NUCL/ENP/12-M04</b>	
9. SPONSORING/MONITORING AGENCY NAME(S) AND ADDRESS(ES)		10. SPONSOR/MONITOR'S ACRONYM(S)	
		11. SPONSOR/MONITOR'S REPORT NUMBER(S)	
12. DISTRIBUTION/AVAILABILITY STATEMENT <b>Approved for public release; distribution unlimited.</b>			
13. SUPPLEMENTARY NOTES <b>The original document contains color images.</b>			
14. ABSTRACT <b>Previous forays by AFIT into positron research have resulted in the development of a new positron annihilation spectroscopy (PAS) technique and the procurement of a low-energy positron beam system. The primary purpose of this research was to design and build a state-of-the-art PAS laboratory at AFIT capable to address a myriad of DoD solid-state and surface physics questions. The main objectives were to acquire and assemble utilities to operate a positron beam, assemble and configure an ultra-high vacuum (UHV) system for samples, design and build an interface with a magnetic field to propagate positrons onto samples, and create a new version of the three-dimensional positron annihilation spectroscopy system (3DPASS). The 3DPASS, which measures coincidence Doppler broadening of annihilation radiation (CDBAR) and two-dimensional angular correlation of annihilation radiation (2D-ACAR), was characterized using a Cu-22Na positron annihilation source made as part of this project. Integration of the 3DPASS with low-energy positron beam will allow for energy-dependent, nondestructive characterization of materials using PAS.</b>			
15. SUBJECT TERMS			
16. SECURITY CLASSIFICATION OF:			17. LIMITATION OF ABSTRACT
a. REPORT <b>unclassified</b>	b. ABSTRACT <b>unclassified</b>	c. THIS PAGE <b>unclassified</b>	
			18. NUMBER OF PAGES <b>131</b>
			19a. NAME OF RESPONSIBLE PERSON

The views expressed in this thesis are those of the author and do not reflect the official policy or position of the United States Air Force, Department of Defense, or the United States Government. This material is declared a work of the U.S. Government and is not subject to copyright protection in the United States.

AFIT/NUCL/ENP/12-M04

DESIGN AND CHARACTERIZATION OF A THREE-DIMENSIONAL  
POSITRON ANNIHILATION SPECTROSCOPY SYSTEM USING A  
LOW-ENERGY POSITRON BEAM

THESIS

Presented to the Faculty  
Department of Engineering Physics  
Graduate School of Engineering and Management  
Air Force Institute of Technology  
Air University  
Air Education and Training Command  
in Partial Fulfillment of the Requirements for the  
Degree of Master of Science in Nuclear Engineering

Stephen M. Jiménez, BS  
Captain, USAF

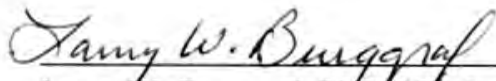
March 2012

DISTRIBUTION STATEMENT A  
APPROVED FOR PUBLIC RELEASE; DISTRIBUTION UNLIMITED.


DESIGN AND CHARACTERIZATION OF A THREE-DIMENSIONAL  
POSITRON ANNIHILATION SPECTROSCOPY SYSTEM USING A  
LOW-ENERGY POSITRON BEAM

Stephen M. Jiménez, BS  
Captain, USAF

Approved:

  
Larry W. Burggraf, PhD, (Chairman)

14 Mar 2012  
Date

  
LtCol Christopher S. Williams, (Member)

8 Mar 12  
Date

  
Maj Benjamin R. Kowash, (Member)

14 Mar 12  
Date

## Abstract

Previous forays by AFIT into positron research have resulted in the development of a new positron annihilation spectroscopy (PAS) technique and the procurement of a low-energy positron beam system. The primary purpose of this research was to design and build a state-of-the-art PAS laboratory at AFIT capable to address a myriad of DoD solid-state and surface physics questions. The main objectives were to acquire and assemble utilities to operate a positron beam, assemble and configure an ultra-high vacuum (UHV) system for samples, design and build an interface with a magnetic field to propagate positrons onto samples, and create a new version of the three-dimensional positron annihilation spectroscopy system (3DPASS). The 3DPASS, which measures coincidence Doppler broadening of annihilation radiation (CDBAR) and two-dimensional angular correlation of annihilation radiation (2D-ACAR), was characterized using a Cu-<sup>22</sup>Na positron annihilation source made as part of this project. Integration of the 3DPASS with low-energy positron beam will allow for energy-dependent, nondestructive characterization of materials using PAS.

## Acknowledgements

I would like to give a special thank you to those who helped with my research: my advisor, Dr. Burggraf and the members of my committee, who provided crucial guidance in completing this project; Eric Taylor, who helped with all aspects of getting equipment installed and operating in Building 470; Brian Crabtree, Chris Harkless, Jan LeValley, and Dan Ryan at the AFIT machine shop without whom none of this research would be possible; Dr. Rod Greaves, who assisted in designing much of the equipment; Bill Martinez and the personnel at the DTRA TEAMS Site at Kirtland AFB, NM who provided critical equipment free of charge to get the system up and running; Dr. Mike Lindsay and personnel at the Air Force Research Laboratory (AFRL) at Eglin AFB, FL who graciously donated the  $^{22}\text{Na}$  sources required for the operation of the positron beam; Maj Paul Adamson, who procured a surface science vacuum chamber from AFRL at Kirtland AFB, NM; Tony Kelly, who wrote the Bash parsing code which significantly decreased the time required to analyze data; the AFIT/ENP lab support folks; Jennifer Meier; my classmates in particular MAJ Quan Lu, Maj(S) Greg Van Dyk, Capt Joel Gearhart, Capt Dan Higgins, Capt Melanie Mace, 2nd Lt Jack FitzGerald, and 2nd Lt Michael Parker; and all those I may have forgotten. Thank you.

Stephen M. Jiménez



# Table of Contents

	Page
Abstract .....	iv
Acknowledgements .....	v
List of Figures .....	ix
List of Tables .....	xi
List of Symbols .....	xii
List of Abbreviations .....	xiii
I. Introduction .....	1
1.1 Background .....	1
1.2 Thesis Goal .....	2
1.3 Positron Overview .....	2
1.4 Positron Annihilation Spectroscopy Techniques .....	6
1.4.1 ACAR .....	7
1.4.2 DBAR .....	9
1.4.3 3DPAMM .....	12
1.5 Positron Beam Technology .....	14
II. Equipment .....	20
2.1 Detectors .....	20
2.2 Electronics .....	23
2.3 Vacuum System .....	24
2.3.1 Vacuum Chamber .....	24
2.3.2 Vacuum Pumps .....	26
2.3.3 Pressure Measurement System .....	27
2.3.4 Source/Sample Manipulator and Holder .....	27
2.4 Positron Beam System .....	28
2.4.1 RGM-1 .....	28
2.4.2 APBS .....	30
2.4.3 Required Utilities .....	30
2.5 Positron Propagation Interface .....	32
2.5.1 Solenoid Coil .....	33
2.5.2 Helmholtz Coils .....	33
2.5.3 Power Supply .....	33
2.6 Sources Used .....	34
2.6.1 <sup>85</sup> Strontium .....	34
2.6.2 <sup>22</sup> Sodium .....	34

	Page
2.6.3 Copper Standard Source .....	35
2.7 Samples Used .....	36
2.8 Shielding .....	36
2.9 Experiment Layout .....	37
III. Laboratory Design Tasks .....	38
3.1 Elevation Components .....	38
3.2 Vacuum System Design .....	39
3.3 Utilities Design .....	40
3.4 PPI Design .....	42
IV. Positron Annihilation Spectroscopy System Characterization and Development .....	45
4.1 Alignment and Source/Sample Holder Calibration .....	45
4.2 Energy Calibration .....	46
4.3 Code Development .....	46
4.3.1 Raw Event File Selection .....	47
4.3.2 Parsing Code .....	47
4.3.3 Relative Efficiency Calculations .....	50
4.3.4 2D-ACAR and CDBAR Analysis Code .....	51
4.4 Cu Sample Coincident 2D-ACAR and CDBAR Experiment .....	52
V. Analysis of Results .....	54
5.1 3DPASS Comparison .....	54
5.2 T-142 Source Configuration Results .....	56
5.3 Raw CuSS 2D-ACAR and CDBAR Results .....	59
5.4 Subpixel Efficiency Correction Results .....	61
VI. Conclusions and Future Work .....	65
6.1 Conclusions .....	65
6.2 Future Work .....	66
Appendix A. PHDs Imager Software Data Format Comparison .....	69
Appendix B. Chilled Water Calculations .....	71
Appendix C. Calculations for the Design of the Positron Propagation Interface .....	73

	Page
C.1 Magnetic Field Calculations .....	73
C.2 Positron Beam Diameter Calculations .....	75
C.3 Power Supply Selection .....	76
C.4 MATLAB® Code for Magnetic Field Calculations .....	76
Appendix D. Procedure for Creating the Copper Standard Source .....	82
Appendix E. Utilities required for RGM-1 and APBS .....	87
Appendix F. Data Parsing Code .....	89
F.1 Bash Script .....	89
F.2 MATLAB® Parsing Code .....	90
Appendix G. Subpixel Efficiency Correction Code .....	97
Appendix H. ACAR/DBAR Analysis Code .....	101
Bibliography .....	112
Vita .....	115

## List of Figures

Figure		Page
1.	Reactions to create positron sources . . . . .	4
2.	$^{22}\text{Na}$ decay scheme . . . . .	4
3.	$^{22}\text{Na}$ decay distributions . . . . .	5
4.	DBAR response to a thermalizing positron in a material . . . . .	6
5.	ACAR Sample Copper Spectra . . . . .	8
6.	One and two detector comparison of DBAR spectra . . . . .	10
7.	Core and valence electron contributions to DBAR . . . . .	11
8.	DBAR energy peak with material defects . . . . .	11
9.	Original 3DPASS configuration . . . . .	12
10.	3DPAMM plots for un-annealed, virgin SiC . . . . .	13
11.	Positron moderation geometries . . . . .	15
12.	Improvements in positron moderation techniques . . . . .	16
13.	Improvements in positron storage techniques . . . . .	17
14.	Diagram of positron beam applications . . . . .	18
15.	PHDs detectors on position translators . . . . .	21
16.	DSSD crystal diagram . . . . .	22
17.	Picture of Spec72 unit . . . . .	23
18.	MDC vacuum chamber with sample and source holder . . . . .	25
19.	Vacuum pump stations connected to vacuum chamber . . . . .	26
20.	Picture of First Point Scientific positron beam system . . . . .	29
21.	Moderator design from RGM-1 . . . . .	29
22.	Recirculating Water Chiller in Building 470 . . . . .	31

Figure	Page
23.	CAD drawing of the positron propagation interface ..... 32
24.	Positron Capsule Design for RGM-1 ..... 35
25.	Picture of the Copper Standard Source ..... 36
26.	Equipment layout ..... 38
27.	Projected histograms of the deviation from colinearity of Cu at 6.65 coordinate ..... 57
28.	Coincident detector response of Cu at 6.65 coordinate ..... 58
29.	Summary of projected histograms using different sample locations ..... 59
30.	CuSS raw 2D-ACAR spectrum ..... 61
31.	Single-crystal Cu 2D-ACAR ..... 61
32.	CuSS raw CDBAR spectrum ..... 62
33.	CDBAR spectrum and lineshape of single-crystal Cu ..... 63
34.	CuSS efficiency corrected 2D-ACAR spectrum ..... 63
35.	CuSS efficiency corrected CDBAR spectrum and DB lineshape ..... 64
36.	Raw and mean efficiency-corrected detector response comparison ..... 65
37.	Plot of magnetic field calculations for PPI ..... 75
38.	Plot of positron beam diameter calculations for PPI ..... 76

## List of Tables

Table		Page
1.	Energy Resolution Data for 3DPASS Using $^{85}\text{Sr}$ 17.5-in from Each Detector .....	48
2.	Comparison of original 3DPASS [30] and 3DPASS built for this research .....	54
3.	Summary of Data Sets Collected Varying Sample Location.....	57
4.	Imager Raw Energy Event Data Format .....	69
5.	Imager Energy Filtered Event Data Format .....	70
6.	Water Cooling Estimates Assuming 22°C Water .....	71
7.	Water Cooling Calculations of FPBS at Agoura Hills, CA with $K=0.264 \text{ kW/gpm-}^\circ\text{C}$ .....	72

## List of Symbols

Symbol		Page
$\beta^+$	Positron .....	2
$e^+$	Positron .....	2
$e^+e^-$	Positron-electron pair .....	3
$\theta$	Deviation from colinearity .....	7
$c$	Speed of light .....	7
$m$	Mass .....	7
$p_{\perp}$	Momentum of the $e^+e^-$ pair in the plane perpendicular .....	7
$\psi_+$	Positron work function .....	15
$\mu_0$	Permeability of free space .....	73

## List of Abbreviations

Abbreviation	Page
PAS	positron annihilation spectroscopy . . . . . iv
UHV	ultra-high vacuum . . . . . iv
CDBAR	coincidence Doppler broadening of annihilation radiation . . . . . iv
2D-ACAR	two-dimensional angular correlation of annihilation radiation . . . . . iv
AFRL	Air Force Research Laboratory . . . . . v
AFIT	Air Force Institute of Technology . . . . . 1
VFRs	vibrational Feshbach resonances . . . . . 1
3DPAMMs	three-dimensional positron annihilation momentum measurements . . . . . 1
AFRL	Air Force Research Laboratory . . . . . 1
Ps	positronium . . . . . 3
PALS	positron annihilation lifetime spectroscopy . . . . . 6
ACAR	angular correlation of annihilation radiation . . . . . 6
DBAR	Doppler broadening of annihilation radiation . . . . . 6
COM	center of mass . . . . . 7
HPGe	high-purity germanium . . . . . 9
DSSD	double-sided strip detector . . . . . 12
PRS	positron reemission spectroscopy . . . . . 18
PAES	positron annihilation induced Auger electron spectroscopy . . . . . 18
REPELS	re-emitted positron energy loss spectroscopy . . . . . 18
LEPD	low-energy positron diffraction . . . . . 18



Abbreviation	Page
PIIDS	positron-induced ion desorption spectroscopy . . . . . 18
AMOC	positron age momentum correlation . . . . . 18
VEPLS	variable energy positron lifetime spectroscopy . . . . . 18
HV	high vacuum . . . . . 20
DSSDs	double-sided strip detectors . . . . . 20
FPGAs	field-programmable gate arrays . . . . . 23
304SS	304 stainless steel . . . . . 24
Cu	copper . . . . . 25
RGM-1	positron source and moderator system . . . . . 28
APBS	advanced positron beam source . . . . . 28
FPBS	First Point Scientific, Inc. positron beam system . . . . . 28
psi	pounds per square inch . . . . . 30
OD	outer diameter . . . . . 30
gpm	gallons per minute . . . . . 31
NPT	National Pipe Thread . . . . . 32
ID	inner diameter . . . . . 32
PPI	positron propagation interface . . . . . 32
CuSS	copper standard source . . . . . 35
MFP	mean free path . . . . . 39
FWHM	full-width at half maximum . . . . . 46
FWTM	full-width at tenth maximum . . . . . 46

# DESIGN AND CHARACTERIZATION OF A THREE-DIMENSIONAL POSITRON ANNIHILATION SPECTROSCOPY SYSTEM USING A LOW-ENERGY POSITRON BEAM

## I. Introduction

### 1.1 Background

The Department of Engineering Physics at the Air Force Institute of Technology (AFIT) has developed a robust program studying nuclear physics of exotic particles, in particular positrons. Previous work has been done looking at positron interactions with materials to include vibrational Feshbach resonances (VFRs) [2] and three-dimensional positron annihilation momentum measurements (3DPAMMs) [30]. This work has created unique capabilities for the further development of positron annihilation studies. Based on previous experimental results and acquisition of new laboratory equipment, a world-class PAS laboratory has been assembled to perform positron research for DoD applications. The design, assembly, and testing of this system will be described throughout this document. The PAS laboratory incorporates two unique pieces of equipment, and low-energy positron beam recently purchased by AFIT and an ultra-high vacuum (UHV) chamber donated by Air Force Research Laboratory (AFRL), Kirtland AFB, NM. With these new tools, future measurements of VFRs and 3DPAMMs of materials will be possible with state-of-the-art resolution.

## 1.2 Thesis Goal

The goal for this thesis is to design and create a state-of-the-art PAS system. The steps to do this are as follows:

- Acquire and design utilities to operate the positron beam system
- Design and assemble an interface system able to propagate positrons from the positron beam system to a sample
- Recreate and improve the 3DPASS as devised by Williams [30] by expanding the momentum field of view
- Characterize the 3DPASS using Cu and  $^{22}\text{Na}$  source configurations
- Create and test data analysis tools to provide 2D-ACAR and CDBAR measurements

The measure of the success of this research is a function of the capability for future AFIT research using a novel 3DPASS system in combination with a high-fluence pulsed positron beam. This system has the capability for non-destructive analysis of defects in solid state materials as well as material surfaces. It has the capability to sensitively measure resonant phenomena at surfaces not accessible by any other technique. Understanding these phenomena have been predicted to hold the key to development of future gamma lasers [21].

## 1.3 Positron Overview

The existence of the positron,  $\beta^+$  or  $e^+$ , was originally proposed by Dirac in 1928 [9] via quantum mechanical calculations and was eventually verified experimentally by Carl Anderson in 1932 [3]. The positron is the antiparticle of the electron, meaning that the positron has equal mass as an electron, but the opposite charge. Before and after thermalization, positrons can interact with matter through several mechanisms.

Positrons can elastically scatter off atoms, excite the target atom, capture an electron to form positronium (Ps), ionize the target atom, annihilate with a free or bound electron, and form compounds by binding with a target atom. For the purposes of this research, the most important interaction mechanisms are the annihilation with a free or bound electron, the formation of Ps and subsequent annihilation, and the formation of a bound state with another atom or molecule.

Positron annihilation results when the rest mass energy of a positron-electron pair ( $e^+e^-$ ) is converted to energy in the form of photons. The most common form of annihilation energy is the emission of two 511 keV photons in opposite directions. Due to the 370-to-1 predominance of two-photon emission over the next most common emission (three-photon), only two-photon annihilation will be considered [19].

Sources of positrons are most commonly created by accelerated particle interactions with nuclei that result in  $\beta^+$  emission, by photon interactions with nuclei and subsequent pair production, or by  $\beta^+$  decays from radioactive isotopes made by bombarding targets with accelerated particles, usually protons. The former methods require particle or photon energies greater than 1022 keV and a favorable reaction to produce positrons or an appreciable pair production cross section of the target nucleus. Figure 1 shows representative favorable reactions for creating positrons [7], some of which are used to create radioactive isotopes that  $\beta^+$  decay.

Regardless of the positron source, positrons have a distribution of energy values after production. An example of this is the radioactive isotope,  $^{22}\text{Na}$ , whose decay scheme is shown in Figure 2 and whose possible energy distributions are shown in Figure 3. The energy distribution of positrons produced by  $^{22}\text{Na}$  is fairly broad, with maximum energy of 546 keV and an average energy of 215.54 keV [10].

The energy distribution of radioactive sources of positrons does not allow for well-conditioned positron experiments due to the variety of ways positrons can interact

1.  $p + {}^{11}\text{B} \Rightarrow {}^{11}\text{C} + n$  ( $E_T = 2.76 \text{ MeV}$ )  
 ${}^{11}\text{C} \Rightarrow {}^{11}\text{B} + e^+$  ( $\tau_{1/2} = 20 \text{ min.}$ )
2.  $p + {}^{13}\text{C} \Rightarrow {}^{13}\text{N} + n$  ( $E_T = 3 \text{ MeV}$ )  
 ${}^{13}\text{N} \Rightarrow {}^{13}\text{C} + e^+$  ( $\tau_{1/2} = 10 \text{ min.}$ )
3.  $p + {}^{15}\text{N} \Rightarrow {}^{15}\text{O} + n$  ( $E_T = 3.53 \text{ MeV}$ )  
 ${}^{15}\text{O} \Rightarrow {}^{15}\text{N} + e^+$  ( $\tau_{1/2} = 2.03 \text{ min.}$ )
4.  $p + {}^{17}\text{O} \Rightarrow {}^{17}\text{F} + n$  ( $E_T = 3.55 \text{ MeV}$ )  
 ${}^{17}\text{F} \Rightarrow {}^{17}\text{O} + e^+$  ( $\tau_{1/2} = 66 \text{ sec.}$ )
5.  $p + {}^{18}\text{O} \Rightarrow {}^{18}\text{F} + n$  ( $E_T = 2.45 \text{ MeV}$ )  
 ${}^{18}\text{F} \Rightarrow {}^{18}\text{O} + e^+$  ( $\tau_{1/2} = 1.87 \text{ hr.}$ )
6.  $p + {}^{19}\text{F} \Rightarrow {}^{19}\text{Ne} + n$  ( $E_T = 4.03 \text{ MeV}$ )  
 ${}^{19}\text{Ne} \Rightarrow {}^{19}\text{F} + e^+$  ( $\tau_{1/2} = 18 \text{ sec.}$ )
7.  $p + {}^{26}\text{Mg} \Rightarrow {}^{26}\text{Al} + n$  ( $E_T = 5.01 \text{ MeV}$ )  
 ${}^{26}\text{Al} \Rightarrow {}^{26}\text{Mg} + e^+$  ( $\tau_{1/2} = 6.5 \text{ sec.}$ )
8.  $p + {}^{22}\text{N} \Rightarrow {}^{22}\text{Na} + n$   
 ${}^{22}\text{Na} \Rightarrow {}^{22}\text{Ne} + e^+$  ( $\tau_{1/2} = 2.6 \text{ years.}$ )

Figure 1. Some of the (p,n) reactions that create  $\beta^+$  emitting radioactive isotopes [7].

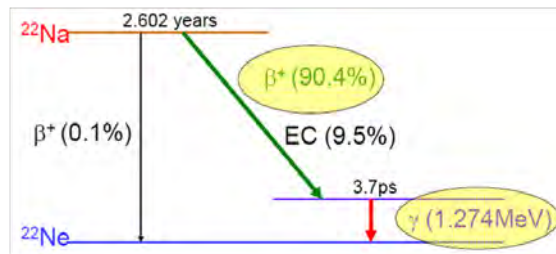
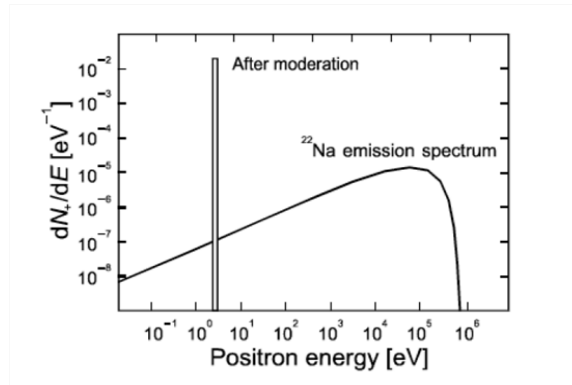


Figure 2.  ${}^{22}\text{Na}$  decay scheme.

with matter. Monoenergetic positrons, especially those of low-energy ( $< 100$  eV), are of particular interest because the probability of isolating some of the positron interaction mechanisms increases at particular energies. For example, Ps formation has a threshold energy on the order of tens of eV. Similarly, the variation of positron energy can reveal VFRs of a material. The VFRs, which lead to increases in annihilation rates in the material, are more prevalent using positrons with energies between 50 meV and many electron volts [15]. Control of positronium annihilation coupled with VFR may have potential in the future to produce a modulated positron source (Burggraf).



**Figure 3.** Energy distributions of  $^{22}\text{Na}$  natural decay emission spectrum and after moderation of a  $^{22}\text{Na}$  source for comparison [2].

Due to the positron's ability to interact with matter and produce consistent energies of annihilation photons, positrons are used to characterize defects in materials. This occurs as the positron penetrates the material (on the order of 100 microns [18]), and annihilates with an electron as shown in Figure 4. As diffusion happens, positrons will be attracted to negatively-charged vacancies or defects in the lattice structure of the material [18]. Positrons can be trapped or stabilized in the vacancy for a short time but will eventually annihilate with electrons of the nearby atoms.

The density and size of these vacancies can be determined via the specific energy and momentum distribution of the annihilation photon spectrum [1, 16, 28].

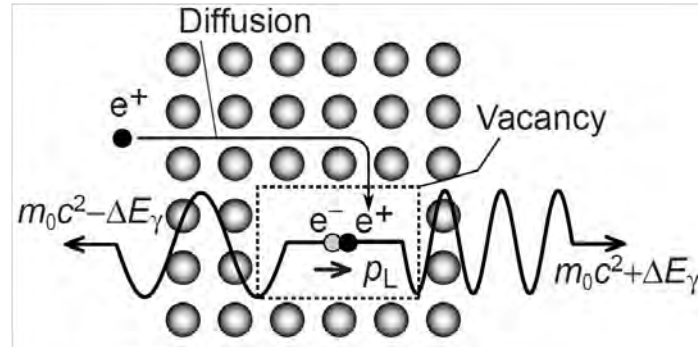


Figure 4. Representation of a positron thermalizing and being trapped in a vacancy-type defect. Note the deviation of the energy of the annihilation photons from the electron rest mass energy by  $\pm\Delta E$  due to the momentum of the annihilating pair,  $p_L$  [28].

#### 1.4 Positron Annihilation Spectroscopy Techniques

PAS techniques involve the detection of one or more of the annihilation photons resulting from  $e^+e^-$  annihilation. The PAS techniques that are most widely used to date are positron annihilation lifetime spectroscopy (PALS), angular correlation of annihilation radiation (ACAR), and Doppler broadening of annihilation radiation (DBAR). PALS usually uses a  $^{22}\text{Na}$  source of positrons and determines the lifetime of a positron in a sample by using the unique 1.274 MeV  $\gamma$ -ray emitted from  $^{22}\text{Ne}^*$  as a start signal and the detection of the 511 keV annihilation photon(s) as the stop signal. The lifetime is the difference in time between start and stop signals. A correction factor of +3.7 ps must be applied to account for the delay in the emission of the 1.274 MeV  $\gamma$ -ray as shown in Figure 2.

The  $e^+e^-$  pair can have intrinsic momentum at the time of annihilation resulting in a change in the energy of the annihilation photons (Figure 4). Due to the con-

ervation of energy and momentum, the momentum of the annihilation photons will be decreased or increased in all three dimensions. ACAR measures the momentum changes in the plane perpendicular to the direction of photon emission. DBAR determines the momentum in the plane parallel. Until recently, the ACAR and DBAR techniques were not combined due to the lack of detectors and electronics that could perform precise, coincident energy and angular momentum. Williams, et al. devised a system that was capable of providing the necessary data and a methodology to extract the three-dimensional momentum vector of the  $e^+e^-$  before annihilation [30]. This technique was termed 3DPAMM. The remainder of this section will briefly discuss ACAR and DBAR techniques and focus on the discussion of the 3DPAMM technique and the characteristics of the 3DPASS. For a more detailed summary of ACAR and DBAR, refer to [30].

#### 1.4.1 ACAR

ACAR determines the momentum of the  $e^+e^-$  pair in the plane perpendicular to the direction of propagation of the photons from the sample to the detectors. The  $e^+e^-$  pair annihilate in their center of mass (COM) reference frame. Applying the laws of conservation of momentum and energy, the deviation from colinearity of the annihilation photons,  $\theta$ , yields the following equation

$$\theta = \frac{p_{\perp}}{mc} \quad (1)$$

where  $c$  is the speed of light,  $m$  is the mass of the  $e^+e^-$  pair, and  $p_{\perp}$  is the momentum component in the plane perpendicular to the photon emission direction [30].

ACAR is accomplished using two detectors on opposite sides of the sample operated in coincidence mode. ACAR can provide one-dimensional (1D) or two-dimensional (2D) momentum densities depending on the type of detectors used. In 2D-ACAR,



two position-sensitive detectors are used. Due to the relationship between angle and momentum from Equation 1, the desired attributes of good 2D-ACAR measurements

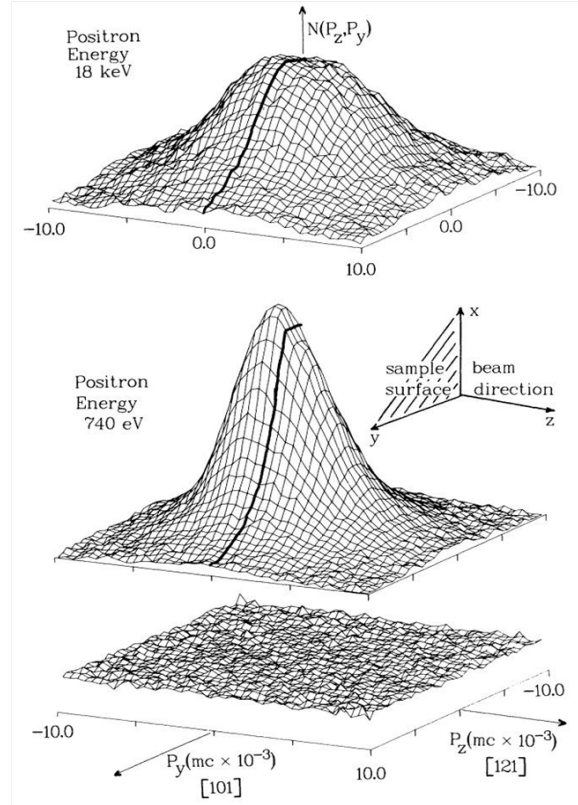


**Figure 5. 2D-ACAR spectra for single-crystal Cu, top: injected with 18 keV positrons, middle: injected with 740 eV positrons, bottom: background spectrum [30].**

are a sufficiently large angular range to encompass momentum features and good angular, and corresponding momentum, resolution. In order to achieve good angular resolution, large detectors must be placed far from the samples, usually on the order of 10 m. The detectors must be large to achieve a large angular range so as to observe a higher angular/momentum region of interest. The detector baselines mean that data collection times are long because isotropic emission of annihilation radiation from the sample decreases as the inverse square of the distance to the detector. Because detectors need to be far from the source, the detectors need to be large (approximately

0.5 m x 0.5 m) to achieve a desired angular range for the experimental setup. To further decrease the data collection time, the large detectors are typically made with NaI scintillators, which are more efficient while still having a better energy resolution than plastic detectors. A method of improving the data collection times of 2D-ACAR is to have a high activity source of positrons to increase the number of annihilation events in the sample.

The measurements of 2D-ACAR provide a momentum density profile that can be seen in Figure 5. The areas of Figure 5 with increased momentum densities correspond to annihilation events with bound state or higher energy electrons. For this experiment, a similar Cu spectrum as in Figure 5 will be collected. However, the positron energy dependence of the peak in the 2D-ACAR distribution is outside the scope of this experiment and will be accomplished in future research.

#### 1.4.2 DBAR

In contrast to ACAR, DBAR determines the momentum of the  $e^+e^-$  pair in the plane parallel to the direction of propagation of the photon from the sample to the detector. There are two types of DBAR measurements: one-detector and two-detector. The latter of these is more often called coincidence Doppler broadening of annihilation radiation (CDBAR). CDBAR greatly reduces the background of the annihilation photopeak by only accepting coincident photons as shown in Figure 6. In either technique, DBAR measures the energy difference or Doppler broadening of the annihilation photons as depicted in Figure 4. DBAR, therefore, requires a detector with good energy resolution such as high-purity germanium (HPGe).

Electrons bound closer to the core of an atom have more energy than the outer shell valence electrons. Because of this, the Doppler broadening of the annihilation photons will be larger when the positron annihilates with the higher angular momentum core

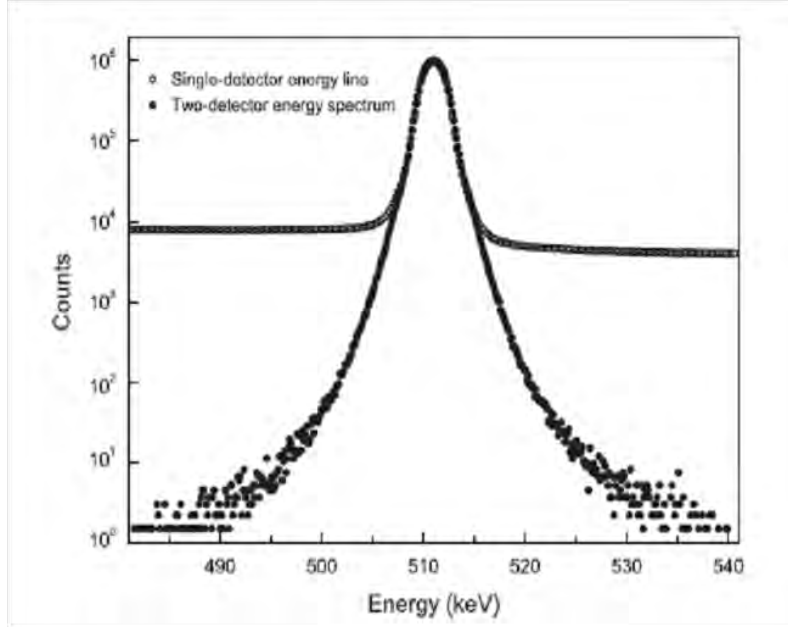


**Figure 6.** Comparison of one and two detector DBAR spectra showing the lower background counts of the two detector system [4].

electrons. This occurs as a result of an overlap of the positron wave function with that of the core electrons. Additionally, the positrons are repelled by the nucleus due to Coulombic repulsion so there is a corresponding preference for annihilation with valence electrons over core electrons. The resulting contribution to the annihilation photopeak can be seen in Figure 7.

The Doppler broadening of the annihilation photopeak has previously been described qualitatively by the S- and W-parameters, which represent the peak sharpness and wings respectively [28]. A summary as to how these parameters are affected by the defects of the material is shown in Figure 8. Typically S and W are chosen to be 0.5 and 0.25 of the normalized total area under the photopeak for a defect-free material. The comparison of the S-parameters and ratio plots of a defect free material to that of a material containing defects are common ways of comparing the materials. However, these methods may be improved by using the 3DPAMM [30].

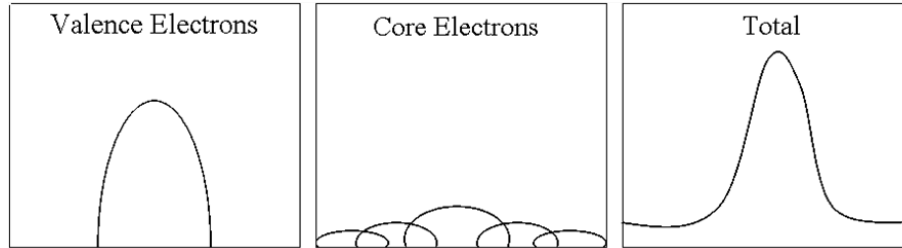


Figure 7. The core and valence contributions to the annihilation photopeak in a DBAR spectrum [31].

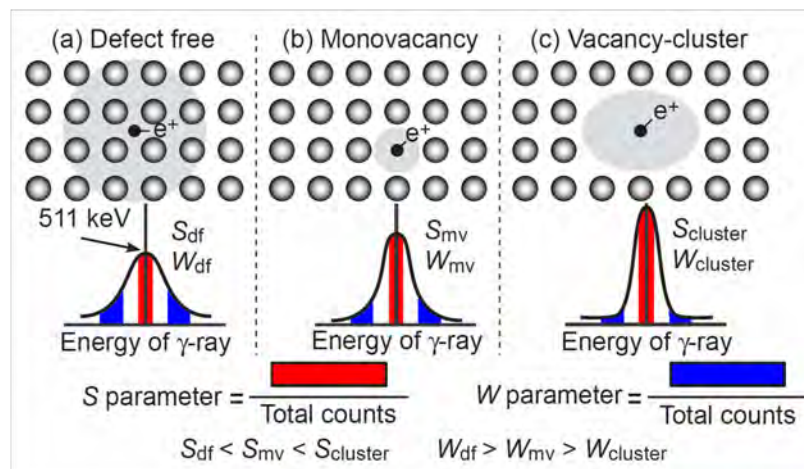


Figure 8. The energy of the annihilation photopeak is described by the S- and W-parameters, which vary depending on the number and quality of the defects within a material [28].

### 1.4.3 3DPAMM

3DPAMM combines the 2D-ACAR and CDBAR techniques to provide a correlated, three-dimensional momentum vector of the  $e^+e^-$  pair before annihilation. In order to take a correlated set of the three dimension of the  $e^+e^-$  momentum vector, a 3DPASS was constructed by Williams, depicted in Figure 9, consisting of two position-sensitive detectors, a coincident electronics suite, and a custom-made vacuum chamber [30]. The detectors were a 5 x 5 Ortec HPGe double-sided strip detector (DSSD) and a 16 x 16 PHDs DSSD of which only the center 8 x 8 strips were used. As such, the angular resolution was set to 0.5 mrad with an angular range of 15 x 15 mrad. The electronics suite, which provided timing coincidence and waveform information, was a Spec32 manufactured by PHDs Co. The energy resolutions of the Ortec and PHDs DSSDs were  $1.76 \pm 0.24$  and  $1.49 \pm 0.17$  keV, respectively. The vacuum chamber was capable of achieving a minimum pressure of one torr [30].

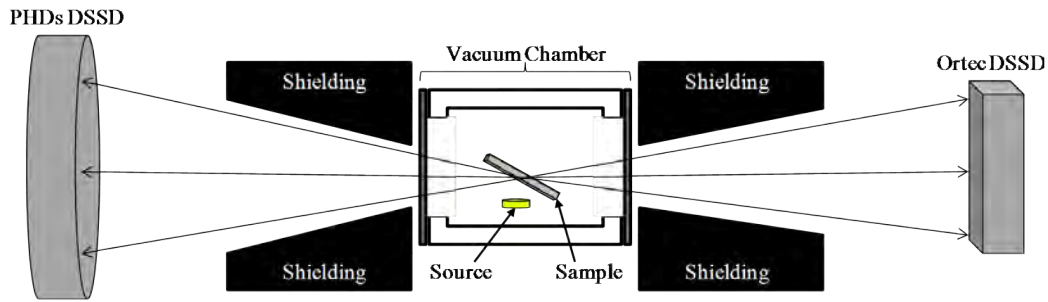


Figure 9. Top view of the final 3DPASS configuration used in experiments by [30], where each detector is  $2.00 \pm 0.01$  m from the center of the sample (not to scale).

The correlated momentum measurements allowed for a more detailed analysis of the isotropy of the annihilation spectrum. The 2D-ACAR data was first analyzed to determine whether there were any symmetric isotropies in momentum space. Figure 10 highlights some symmetric isotropies of 6H SiC measurements taken by Williams

[30]. Next, the CDBAR data was analyzed to provide a CDBAR profile that is characteristic of the whole material and a CDBAR profile that limits the energy data to only symmetric isotropies if they are present. A comparison of these profiles is shown in Figure 10. The black profile in the right hand plot is the CDBAR plot

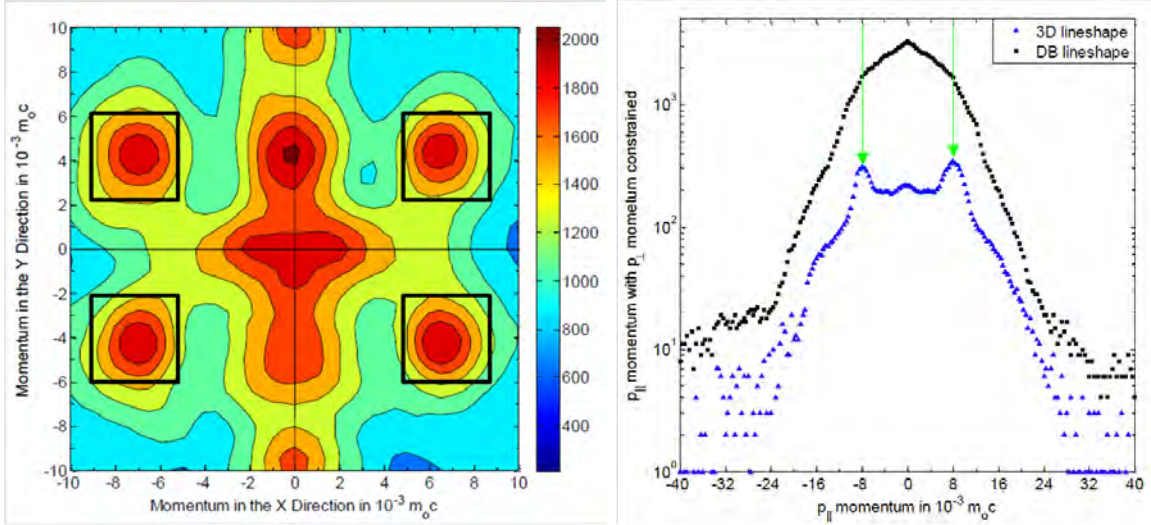


Figure 10. 3DPAMM plots of the CDBAR spectrum (left) shows the  $p_{\parallel}$  component for virgin, un-annealed 6H SiC with the  $p_{\perp}$  component constrained by the momentum peaks in the 2D-ACAR spectrum (right) centered at (5:9,2:6), (5:9,-2:-6), (-5:-9,2:6), and (-5:-9,-2:-6).  $\Delta = 0.3$  keV was used to define the 3D momentum lineshape width of the  $p_{\parallel}$  component. Black squares indicate the unconstrained DB lineshape and blue triangles represent the constrained, 3D momentum lineshape [30].

and shows indications of shoulder and neck features. The blue data set represents the 3DPAMM spectrum that results by constraining the original CDBAR plot by the 2D-ACAR isotropies in the left hand plot. The 3DPAMM spectra enhances some of the shoulder and neck features from the CDBAR spectra.

The 3DPAMM technique suffers from the same limitations as the 2D-ACAR and CDBAR methods. HPGe detectors are used to satisfy the energy resolution criteria necessary for CDBAR, and the detectors are also position-sensitive so as to provide the angular range and resolution required for 2D-ACAR. The utilization of transient

charge analysis between strips in the HPGe position-sensitive detector allows the detectors to be placed closer to the samples, thereby decreasing the data collection time. This helps to overcome the fact that the HPGe detectors are less efficient than NaI.

## 1.5 Positron Beam Technology

As mentioned in section 1.3, there are three sources of positrons: nuclear reactions, pair production, and radioactive isotopes. Positron beams have been created using all production techniques in a variety of configurations. The most common configurations are based on linear accelerator technologies and radioactive isotopes. Figure 1 shows representative proton-neutron reactions that are used to create radioactive isotopes for positron beams.

The primary purpose of positron beams is to control the positron energy and deliver pulses of positrons increasing the intensity of positrons incident on the location of interest. To achieve this, positrons must be moderated to the desired energy and guided to the target. Positron production, moderation, and propagation onto targets form the basis for all positron beams regardless of configuration.

An objective of this research is to provide a source of low-energy, approximately 1 - 20 eV, positrons, which is best achieved by moderation and trapping strategies using radioactive isotopes such as the Surko method. Therefore, this section focuses on positron beam technology most commonly associated with radioactive isotope based positron beams particularly using the Surko design that is commercially available through First Point Scientific, Inc [13, 14, 23, 24, 25, 26].

The depth at which the positron is able to penetrate the material depends on the density of the material and the positron energy; however, as shown in Figure 3, positrons acquired via  $\beta^+$  decay have a broad energy spectrum. The moderation



of positrons provides a method to control the positron energy in experiments. In order to moderate positrons to a single energy, the positrons must interact with a material to remove energy and be confined by electric and/or magnetic fields to prevent the positrons from interacting with the confining vacuum walls. An acceptable moderating material will have positron interactions with a negative positron work function,  $\psi_+$ , which determines the energy of the emitted positron. Figure 11 shows some of the positron moderation techniques that have been implemented [8].

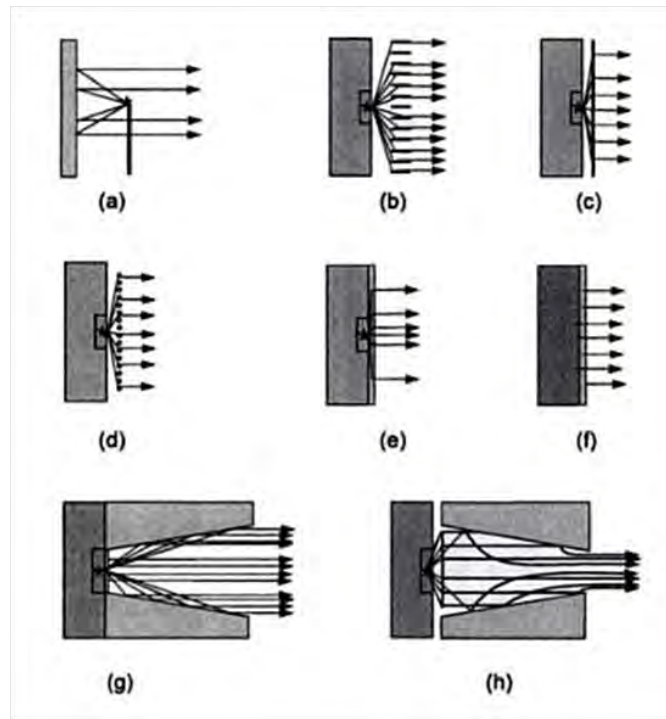


Figure 11. A selection of moderator geometries. The asterisk represents the primary positron source. (a) backscattering, (b) Venetian blind, (c) thin film, (d) mesh, (e) deposited moderator, (f) self-moderating source material on high-Z backing, (g) thin film plus cone, and (h) thin film plus reverse cone [8].

The efficiency of each moderation technique is defined by the number of positrons incident on the moderator divided by the number of positrons incident on the target after leaving the initial moderator to form the beam. Moderator efficiencies have



improved by orders of magnitude in the past 60 years going from  $10^{-8}$  to  $10^{-2}$ , Figure 12. Some recent improvements have been in the development of using solid neon as a moderating material and improving electrostatic fields that assist in extracting positrons after they are moderated. The most recent improvements involve dramatically increasing the number of positrons available by using improved storage techniques. Figure 13 shows comparisons of the notable improvements.

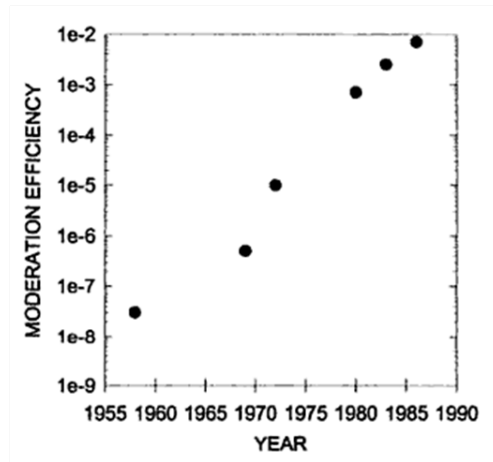


Figure 12. Growth in measured positron moderation efficiencies since 1958 [8].

Despite dramatic improvements to moderation technology, moderators have less than ideal efficiencies (usually less than 1%). Therefore, methods have been developed to enhance the number of positrons incident on the sample. Magnetic transport of the positron beam is most commonly achieved via a series of coils that provide a uniform magnetic field, which guides the positrons in a helical motion onto the sample. Using magnetic transport is not always beneficial for some positron measurements techniques especially those that detect reflected or re-emitted positrons or Auger electrons. In a strong magnetic field, the charged particles of interest would not be allowed to move isotropically, but rather would continue to be propagated in the path dictated by the magnetic field. If re-emission measurements are desired, an

electrostatic focusing lens can be used to maintain the continuity of the positron beam as it is removed from the magnetic field [8].

Improvements in electrostatic transport and focusing techniques have increased the number of positrons of a particular energy per unit area or brightness of the beam [8]. The rotating wall technique radially compresses the positron plasma that makes up the beam by coupling a rotating electric field to the plasma to apply a torque to the plasma. The downside to this technique is that the injected angular momentum heats the plasma. A low temperature is required to maintain the energy profile of the positron plasma. This can be achieved by cyclotron cooling, a buffer gas, or sympathetic cooling using laser-cooled ions. A buffer gas is the most efficient of these methods [24] and is utilized in the positron beam system at AFIT.

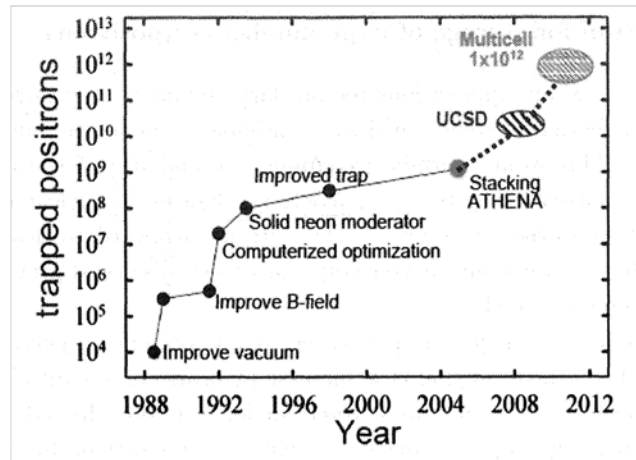
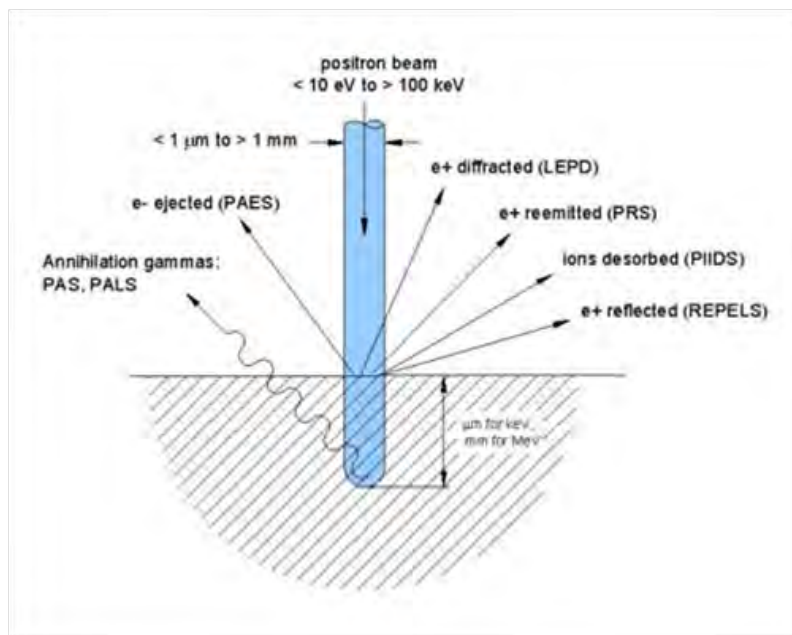


Figure 13. Progress in positron trapping from similar strength sources of 50-100mCi  $^{22}\text{Na}$  using a buffer gas accumulator, including stacking positron plasmas in UHV. The UCSD oval represents parameters achieved for an electron plasma; whereas the multicell oval shows the expected value for a multicell trap [25].

Finally, positron accumulation has been achieved using positron traps, which cool positrons via inelastic scattering. Several methods of trapping have been developed which include trapping by collisions with a buffer gas, trapped ions, trapped electrons,

trapping by electronic dampening chaotic orbits, and field ionization of Rydberg Ps atoms. The most efficiency trapping mechanism uses a N<sub>2</sub> buffer gas which can achieve trapping efficiencies of greater than 30% [12].

Positron beam technology provides distinct advantages versus using isotropic sources in the study of materials by introducing the ability to control positron energy, positron interaction location on the target, and timing of positron interactions. The advantages make a variety of positron measurements possible. Figure 14 shows a



**Figure 14.** A diagram of the potential experiments that can be conducted using a positron beam to interrogate materials [11].

summary of the material diagnostic applications used with positron beams to include positron reemission spectroscopy (PRS), positron annihilation induced Auger electron spectroscopy (PAES), re-emitted positron energy loss spectroscopy (REPELS), low-energy positron diffraction (LEPD), positron-induced ion desorption spectroscopy (PIIDS), positron age momentum correlation (AMOC), variable energy positron lifetime spectroscopy (VEPLS), PALS, DBAR, and ACAR [11, 14]. At AFIT researchers

plan to use energy-selected positrons to study 3DPAMM, but also to study surface-absorbed molecules using Feshbach resonance-enhanced PIIDS, also not previously done.

## II. Equipment

This section discusses the equipment that was designed or used to recreate the original 3DPASS, expand its momentum range, and combine it with a low-energy positron beam. The new 3DPASS based on the design by Williams is comprised of two identical position sensitive detectors, a digitizing, coincident electronic suite, and a high vacuum (HV) system with a source-sample holder [30]. The positron beam system, the design of the cooling water and pressurized air utilities, and a beam propagation system designed to interface the positron beam with the vacuum chamber are discussed. The sources and samples to be used in this research are subsequently detailed to include planchet sources and the positron beam system sources. Finally, a brief overview of the shielding and experiment layout is provided.

### 2.1 Detectors

The detectors used in the 3DPASS are HPGe double-sided strip detectors (DSSDs) manufactured by PHDs Co. The two identical detectors are shown in Figure 15. These detectors replace the detectors used by Williams [30]. The HPGe crystal provides the capability of achieving the energy resolution necessary for CDBAR measurements; whereas, the DSSD design, along with interpolation methods, provides the position sensitivity required for 2D-ACAR measurements.

Each detector contains one HPGe cylindrically planar crystal with a diameter of 9 cm and an active depth of 11 mm. The crystal also has two sets of sixteen amorphous Ge contacts allocated on the front and rear of the crystal with the front set being orthogonal to the rear strips. Each strip has a width of 4.75 mm with a gap of 0.25 mm between each strip, Figure 16. Half of the strips corresponding to one side of the crystal are operated as the DC side, while the other side of the crystal is the AC



**Figure 15.** Pictures of the PHDs double-sided strip detectors (DSSDs) used in the three-dimensional positron annihilation spectroscopy system (3DPASS). Detector 0 is on the left and Detector 1 is on the right. Both are mounted on a 3-axis position translator designed to align the detectors to the vacuum chamber.

side. The designation of AC side versus DC side does not correspond to AC or DC currents; rather, the designation is a naming convention for the detector strips.

The detectors, labeled as NP4-AFIT (Detector 0) and AFIT2010 (Detector 1), are individually monitored and controlled by separate power controllers, which set the detector operating settings. To achieve full depletion of the semiconductor, the HPGe crystals must be kept at low temperatures and have high voltages applied across the crystal. The power controllers set the voltage biases to -600 V and -580 V for Detector 0 and Detector 1 respectively. These values were determined by the manufacture to be the optimum operating voltages for each detector. The HPGe crystals are kept at a low temperature (approximately 65 K) by a mechanical cooler and maintained thus by insulating the crystal in a  $10^{-9}$  torr vacuum achieved by an ion pump. It is important to note that the temperature diodes are inoperable for both detectors due to damage incurred in an unplanned power outage; therefore, the power controllers must be operated in superuser mode. This mode requires the user to manually turn

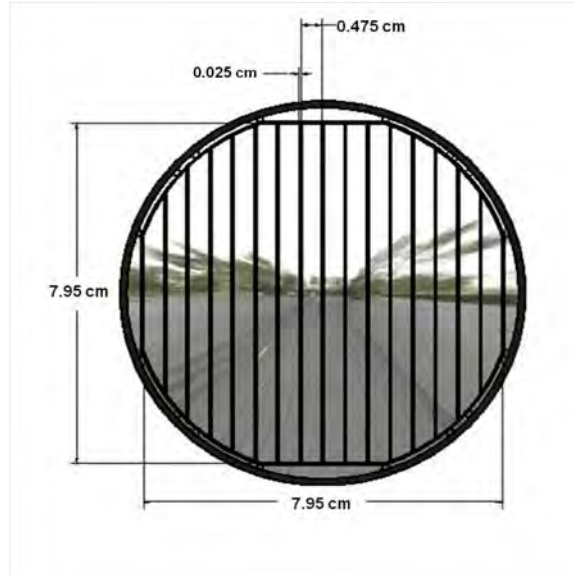


**Figure 16. Diagram of DSSD crystal with one side of charge collection strips illustrated.**

on the preamps and high voltage for each detector. The detector performance may be degraded by the failure of the temperature diodes, but a comparable data set for the time before the outage is not available.

Each detector is mounted on a dampened, three-dimensional position translator that was made by the AFIT machine shop. The basis for the translation system is a pair of Unistrut<sup>®</sup> rails that allow the detectors to be roughly translated from 1 - 3 m from the center of the vacuum chamber, Figure 15. The top part of the position translator consists of four 7-in supports and four aluminum plates. The purposes of the top part of each mount are to connect the detector to the railing system, to elevate the detector to the sample height in the vacuum chamber, and to provide finer positioning of the detectors in three axes. There is a maximum movement of 1-in in either direction in plane parallel to the ground and 3-in in the vertical axis. Dampening, provided between the last plate and the base of the detector, is required to minimize the microphonic noise in the HPGe detector produced by vibrations.

## 2.2 Electronics

A specialized electronic suite, Spec72, is used to collect and filter the signals which can come from any of the sixty-four channels of the PHDs DSSDs. The Spec72, shown in Figure 17, is a custom-made electronic system manufactured by PHDs Co. that is capable of providing coincident digital data acquisition for up to seventy-two channels in coincidence. The basis of the Spec72 consists of one motherboard with a 20 ns clock cycle and nine daughter boards. The seventy-two channels are evenly distributed among the daughter boards, each with 12-bit analog-to-digital converters, eight input channels, and two field-programmable gate arrays (FPGAs). The waveforms from the preamplifiers of the DSSDs are digitized per user-defined settings in the PHDs software, Imager. The Imager software is used to program the FPGAs and record information for each channel from the Spec72 based on the time integral of the signal pulses from the detector. All signals within a coincidence timing window are logged



**Figure 17. Picture of Spec72 digital electronics processing unit and power controllers for each detector. Each of the cables plugged into the top of the unit carries a signal from either one of the DSSD channels or one of the other detectors.**

as a single event in the output file(s).

Data can be recorded into three file options: energy-filtered events, raw energy



events, and raw data. For this experiment, the raw energy event files are used to calculate correlated 2D-ACAR and CDBAR momentum spectra. These files log each signal and include the order of arrival, the number of clock cycles after the trigger, the calibrated energy, and the FOMs for the previous adjacent strip (or “predecessor”) and succeeding adjacent strip (or “successor”) [22]. Table 4 in Appendix A shows the data formats. The FOMs are calculated via a proprietary method developed by PHDs Co. However, each FOM is proportional to the transient charge of a strip that is adjacent to the full-energy strip. The transient charge is the amount of charge detected by the adjacent strip as a hole-electron pair travel to the full-energy strip.

## 2.3 Vacuum System

The vacuum system provides an environment that maximizes the number of positron interactions with the samples. This is achieved by decreasing the number of gas particles available to interact with positrons between source and sample target. For the experimental setup, the vacuum system consists of a vacuum chamber, several vacuum pumps, a vacuum measurement system, and a source/sample holder and manipulator. Overall, the vacuum system is capable of an ultimate pressure on the order of  $10^{-11}$  torr; however, a minimum pressure of  $1.1 \times 10^{-5}$  torr was achieved.

### 2.3.1 Vacuum Chamber

The vacuum chamber, pictured in Figure 18, is a MDC surface science chamber, product reference number SSAC-12D, that has been modified to have an adjustable support stand and a custom made 14-in CF port with five 4.5-in CF ports. These modifications and many of the available vacuum flanges and fittings are the result of a donation from AFRL at Kirtland AFB, NM via the efforts of Maj Paul Adamson. All parts of the chamber, flanges, and fittings are made of 304 stainless steel (304SS)

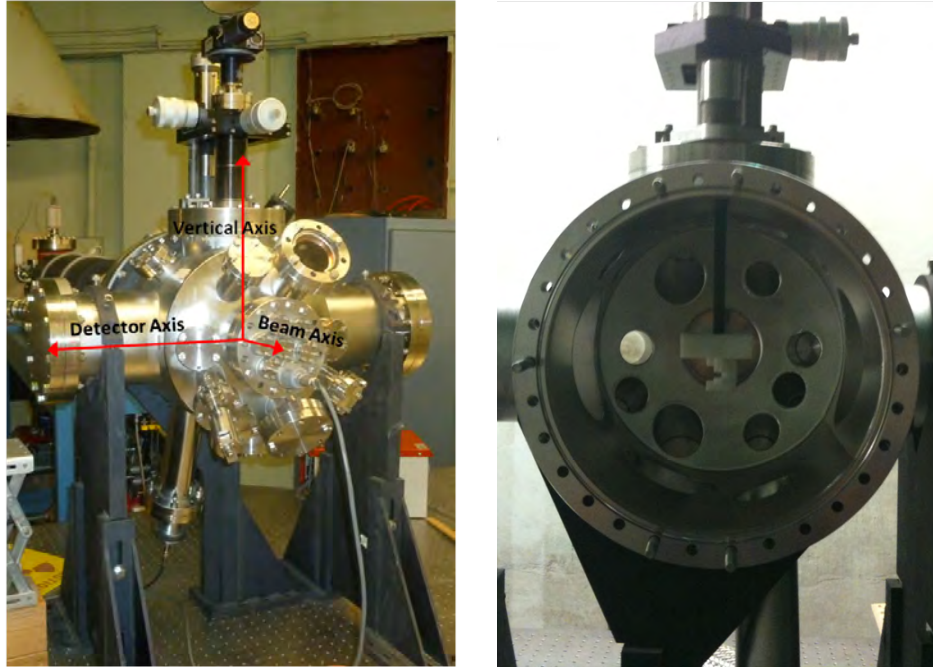


**Figure 18.** Pictures of the MDC surface science vacuum chamber equipped with vacuum gauges and leak valves attached to the chamber and the axis definition used for this setup (left) and the inside of the chamber with the sample/source holder attached to sample manipulator (right).

with CF seals. With the exception of one 2.75-in CF flange, all of the gaskets are made of copper (Cu) but can be replaced by Viton<sup>®</sup> gaskets. With Cu gaskets and no leaking, the chamber is capable of holding a minimum vacuum pressure of  $10^{-11}$  torr.

The orientation of the vacuum chamber has the 8-in port, which has the shortest focal length and attaches the XYZ $\theta$ -manipulator, mounted vertically and the 14-in port facing the positron beam. The remaining 8-in ports, with focal lengths of 12-in and 13.5-in, face Detector 0 and Detector 1 respectively. To decrease the attenuation of the annihilation photons seen by the detectors, these ports are each equipped with a 304SS flange that has been modified by the AFIT machine shop by boring a hole through most of the center of the flange. The dimension of the hole are a thickness of 10 mil (0.01-in) around a 0.5-in radius at the center of the flange. There is also

a manual all-metal leak valve, part number VZLVM29 made by Kurt J. Lesker Co., that is used to backfill the vacuum chamber when needed.

### 2.3.2 Vacuum Pumps

Two turbo pumping stations with a total of four vacuum pumps are used to decrease the number of particles in the environment surrounding the source and sample configuration in the 3DPASS. The first pumping station is a Pfeiffer HiCube 80 Eco turbo pumping station, which has a Pfeiffer HiPace 80 turbomolecular pump with a Pfeiffer MVP-015 diaphragm pump that acts as a backing pump. Also, an electronics drive unit and display unit are built into the system. The Pfeiffer pumping station is connected to the vacuum chamber via a 4.5-in CF flexible tube to a 4.5-in CF flange on the vacuum chamber. The Pfeiffer station can be isolated from the vacuum chamber via a 4.5-in manual gate valve. This setup can be seen in Figure 19.



Figure 19. Pictures of the Pfeiffer HiCube 80 Eco turbo pumping station (left), Varian V-70LP turbo pumping station (right), connecting hardware, and the MDC vacuum chamber.

Similarly, the Varian pumping setup contains a main pump, backing pump, and electronics control unit. A Varian V-70LP turbomolecular pump with Varian 949-9411 diaphragm backing pump is mounted on a special electronics rack with a Varian V-70 electronics control unit. A series of reducing flanges and 2.75-in CF tubing connect the pumping setup to the vacuum chamber as depicted in Figure 19. The Varian pumps can be isolated by a 2.75-in gate valve. Under ideal circumstances, both turbomolecular pumps are capable of an ultimate pressure of  $10^{-11}$  torr.

### 2.3.3 Pressure Measurement System

Three components make up the entirety of the pressure measurement system: a Varian XGS-600 vacuum gauge controller equipped with a convection board and an IMG board, a Varian IMG-300 inverted magnetron gauge, and a Varian ConvecTorr thermocouple pressure gauge. The IMG-300, which has an operating range from  $10^{-3}$  to  $10^{-11}$  torr, outputs a small radial magnetic field of approximately 10 gauss at 4-in from the gauge. Therefore, it is mounted at the farthest possible point from the source and sample, which corresponds to a focal length of 13.75-in on the bottom of the vacuum chamber. The operating range of the thermocouple is from atmospheric pressure to  $10^{-4}$  torr. Having no potential to interfere with the positrons interacting with the sample, the ConvecTorr gauge is mounted approximately 7.5-in from the center of the chamber.

### 2.3.4 Source/Sample Manipulator and Holder

A 4-axis (X, Y, Z, and  $\theta$ ) intravacuum manipulator is mounted on the top port of the vacuum chamber. The X, Y, Z, and  $\theta$  ranges of the 4-axis manipulator is  $\pm 0.5$ -in in the X and Y directions, 6-in in the vertical or Z axis, and  $2\pi$  radians for  $\theta$ . The base of the XYZ $\theta$ -manipulator has a 2.75-in CF flange with a Viton<sup>®</sup> gasket. The

design of the 8-in to 2.75-in reducing flange is such that the pressure applied to a Cu gasket is insufficient to properly seal the gasket. This is the limiting factor in achieving a better vacuum.

The source/sample holder is the same polyethylene holder designed by Williams for the original 3DPASS [30]. The holder is modified to attach inverted from the XYZ $\theta$ -manipulator as can be seen in Figure 18. The center of the sample is approximately 1-in from the source with a 45° orientation to the normal vector of the planchet source. Both the source and sample are held in place by polyethylene pieces that clamp the source and samples in place.

## 2.4 Positron Beam System

The low-energy positron beam system produced by First Point Scientific, Inc. is a Penning-Malmberg moderator-trap, which can be seen in Figure 20. The configuration consists of the positron source and moderator system (RGM-1), the advanced positron beam source (APBS), associated support electronics, and LabView control software. This subsection briefly discusses the beam system characteristics and utilities required for operation. For the purposes of this paper, the entire system to include the RGM-1 and APBS is referred to as the First Point Scientific, Inc. positron beam system (FPBS).

### 2.4.1 RGM-1

The RGM-1 houses the specially designed capsules, which are  $^{22}\text{Na}$  positron sources. The RGM-1 uses a two-stage cold head to grow a solid neon moderator on the surface of a cone near the source, Figure 21. The source is shielded in vacuum by Elkonite and externally by lead shot. The maximum source strength that can be accommodated with the RGM-1 is 150 mCi. For a 50 mCi source, the positron flux



Figure 20. Picture of the First Point Scientific positron beam system at AFIT. The positron source moderator (RGM-1) is to the left, and the buffer gas positron trap (APBS) is to the right.

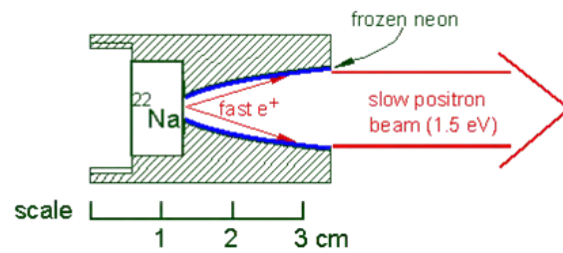


Figure 21. Sketch of the design of the positron moderator in the RGM-1 [23].



is on the order of eight million per second. The solid neon moderator, which is typically grown in 20 minutes via computer control, decays at approximately 4% per day and has a moderation efficiency of 1%. After moderation, the beam is magnetically transported to the APBS. At the APBS entry flange, the beam is less than 3 mm in diameter with an energy spread of 1.3 - 2.5 eV.

### **2.4.2 APBS**

APBS has two pressure stages and three electrostatic stages used to trap and cool the positron beam from the RGM-1. N<sub>2</sub> acts as the buffer gas, and SF<sub>6</sub> is the cooling gas. The low-energy positron beam that comes out of the APBS provides a monoenergetic supply of positrons with energies on the order of 1 to 10's of eV's. A rotating magnetic field compresses the beam diameter to 1 - 1.2 mm, which will allow for scanning of materials as opposed to having an isotropic illumination of the sample. The beam has an energy spread of 0.03 - 0.3 eV with a trapping efficiency of approximately 17 percent.

### **2.4.3 Required Utilities**

The FPBS requires pressurized air and chilled water for operations. Due to the rules of operation in the dome of Building 470 where the system is installed, the utilities are provided to the FPBS via experimental ports located in the dome wall. Pressurized air is needed to operate the pneumatically actuated gate valves that control the positron flux from the RGM-1 to the APBS and the isolation of the vacuum pumps of the FPBS. A 300 liter N<sub>2</sub> tank, located in Room 105 of Building 470, provides a constant pressure of 70 pounds per square inch (psi) to operate the gate valves via 0.25-in outer diameter (OD) nylon plumbing and 0.25-in compression fittings, which are rated to withstand pressures of 250 psi.

The chilled water comes from a 10.6 kW recirculating chiller located in the basement of Building 470, which is pictured in Figure 22 and was a donated to the project by the DTRA TEAMS site at Kirtland AFB, NM. The chiller, manufactured



**Figure 22.** Picture of the Schreiber 300-AC 10.6 kW recirculating water chiller located in the basement of Building 470. Equipment courtesy of the DTRA TEAMS site at KAFB, NM.

by Schreiber, model number 300-AC, provides the chilling water to appropriately cool the electromagnetic coils of the FPBS, the cold head compressor on the RGM-1, and the cryogenic pump compressor on the APBS. The water flow is controlled by separate flow meters and bellows valves to optimize the chilled water provided to each component. A bypass, consisting of two brass ball valves, is located in Room 105 to shut off water flow into the dome when the FBPS is not in operation. The chiller is capable of pumping water that is chilled to a maximum of 50°C at a maximum flow rate and total dynamic head of 50 gallons per minute (gpm) and 160 feet respectively. The estimated flow rate that is needed is 6 gpm with cooling power of 6 kW. Supporting methodology and calculations for the chilled water can be found in Appendix B.



The plumbing for the chilled water is a combination of compression fittings, National Pipe Thread (NPT) fittings, 0.5-in OD nylon tubing, and 0.5-in inner diameter (ID) flexible hose. As a whole, the plumbing system is limited to a pressure of 200 psi.

## 2.5 Positron Propagation Interface

A crucial aspect in mating the FPBS to the vacuum system, described in Sections 2.3 and 2.4, is the ability to propagate the positron beam from the 2.75-in CF output flange of the APBS onto the sample in the vacuum chamber without excessive divergence of the beam diameter. The distance the positrons must travel is approximately 36-in, and they must maintain a beam diameter less than 5 mm. A series of magnetic fields obtained by a solenoid coil, a pair of Helmholtz coils, and a dual output power supply maintain the positron beam continuity onto the sample. These components make up the positron propagation interface, a model of which is pictured in Figure 23. Detailed calculations which were conducted to design the positron propagation interface (PPI) can be found in Appendix C.

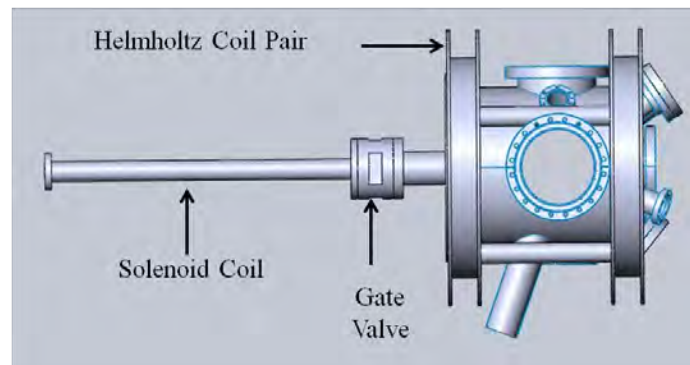


**Figure 23.** CAD drawing of the positron propagation interface between the APBS and the vacuum chamber.

### 2.5.1 Solenoid Coil

The solenoid coil is built around a 304SS, 24-in long, 2.75-in CF to 4.5-in CF reducing nipple. The actual length of the coil when wound is 22.5-in and is made with 0.06-in by 0.13-in HML insulated rectangular Cu wire. To further insulate the nipple from the magnetic field of the solenoid coil, 5-mil Kapton<sup>®</sup> tape is wound around the reducing nipple before coiling the wire. There will be a total of 519 wounds of Cu wire on the vacuum nipple to make the solenoid coil. The minimum magnetic field that is needed to achieve the desired beam spot is on the order of 80 gauss.

### 2.5.2 Helmholtz Coils

Due to the dimensions of the vacuum chamber, the Helmholtz coil pair is wound on a 2-in by 2-in anodized aluminum frame with an ID of 16-in and separation distance of 11-in. To create a uniform magnetic field, the separation distance of the coils must be equal to radius of the coils, which is not the case for this Helmholtz coil pair. Each coil contains 390 winds of 0.065-in by 0.132-in HML insulated rectangular Cu wire. OMEGATHERM<sup>®</sup> 201 thermally conductive silicon paste is spread between each layer of Cu wire to increase the heat dissipation of the coil away from the center. The Helmholtz coils are connected via eight 1-in brass rods and are supported by 0.25-in aluminum plating connected to the optical table.

### 2.5.3 Power Supply

The solenoid and Helmholtz coils are both controlled by the same power supply. A Sorenson XPF60-20DP dual output power supply can output a max power of 420 watts per output. The Helmholtz coils operate at a current of 10 - 11 amps, while the solenoid operates at a 8 - 12 amps. Without adding water cooling, these are the

maximum allowable currents to keep the coils from overheating. These maximum currents correspond to magnetic fields of 140 - 160 gauss for the Helmholtz coils and 60 - 140 gauss for the solenoid coil. At the sample location in the vacuum chamber, the magnetic field will be 120 - 140 gauss, which corresponds to a beam diameter of 2.5 - 3.5 mm. Appendix C shows the sample calculations of the magnetic fields and beam diameter and MATLAB<sup>®</sup> code of the simulation.

## 2.6 Sources Used

A variety of different radiation sources are used in this experiment. Each source is used for a specified purpose. The sources are designated with AFIT numbers that will be used to identify the sources throughout this document.

### 2.6.1 <sup>85</sup>Strontium

<sup>85</sup>Sr is useful for characterizing the energy resolution and efficiency of detectors in PAS techniques. <sup>85</sup>Sr has a characteristic  $\gamma$ -ray at 514 keV, which is very close to the 511 keV photons from  $e^+e^-$  annihilation events. However, the <sup>85</sup>Sr characteristic  $\gamma$ -ray is not subject to the Doppler-broadening of the annihilation photons when compared to the that of a <sup>22</sup>Na source. In this experiment, the <sup>85</sup>Sr source is a standard planchet source designated with the AFIT number T-142, which was assayed to be 90.91  $\mu$ Ci on 01 December 2010.

### 2.6.2 <sup>22</sup>Sodium

<sup>22</sup>Na is a standard source of positrons used due to the well-documented decay scheme, Figure 2; resulting positron energy distribution, Figure 3; and ease of making <sup>22</sup>Na sources. The first type of <sup>22</sup>Na source used is a planchet source with AFIT number T-132 and has an activity of 106.5  $\mu$ Ci assayed on 15 August 2009. The

second type of  $^{22}\text{Na}$  source is not a standard configuration. The small capsule

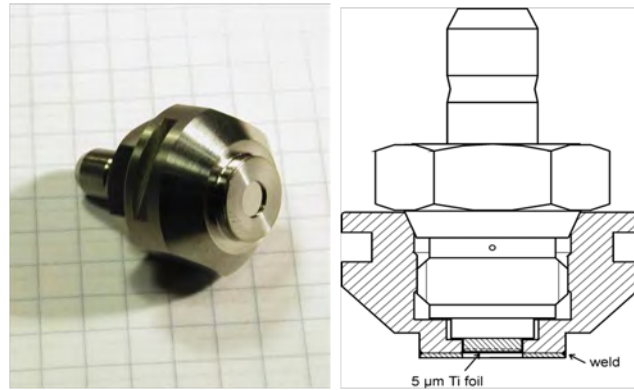


**Figure 24. Positron Capsule Design for RGM-1 component of the First Point Scientific, Inc. Positron Beam System [17].**

design, which is depicted in Figure 24, is manufactured by iThemba LABS in South Africa. The capsule is designed to fit into a Cu holder that mounts in the RGM-1. The two sources of this configuration are courtesy of AFRL at Eglin AFB, FL. Activities of the sources are 1 mCi and 0.1 mCi assayed in October 2006. The capsule sources do not have AFIT numbers as of this publication.

### 2.6.3 Copper Standard Source

A copper standard source (CuSS) was made for this experiment using a carrier-free  $^{22}\text{Na}$  solution, Figure 25. The purpose was to increase the number of positrons that were incident on the Cu samples, which allows for comparison of 2D-ACAR and CDBAR spectra with previous work. Additionally, positrons annihilate with the large number of free electrons in Cu, which equates to a narrow CDBAR and 2D-ACAR and lower  $e^+e^-$  momentums. Drops of the  $^{22}\text{NaCl}$  solution were slowly evaporated onto two Cu 10.0 x 10.0 x 0.4 mm samples via the procedure in Appendix D until the entire 2.2 mL of solution was used. The activity of the CuSS was 23.3  $\mu\text{Ci}$  as of 18



Figure 25. Picture of the copper standard source, T-134P made by Walker [29]. A similar source, T-127L, was made as a calibration and alignment source on 18 Jan 2012 with an initial activity of  $23.3 \mu\text{Ci}$  .

January 2012. The CuSS, designated AFIT number T-127L, provided a source that doubles as a sample that can be used to align the detectors in the 3DPASS [30].

## 2.7 Samples Used

Only one type of sample is to be used in this research, copper. The Cu samples are identical to the samples used in previous work by Williams [30]. Purchased from MTI corporation, the  $10.0 \times 10.0 \times 0.4$  mm samples with a crystal orientation of (100) are used to align the 3DPASS and create the CuSS mentioned in Subsection 2.6.3.

## 2.8 Shielding

The shielding used in this experiment was designed to maximize the detection of the  $e^+e^-$  annihilation photons that originated in the sample. To do this, lead was placed inside the vacuum near the source and outside the vacuum near the detectors. To decrease the detection of annihilation photons from positrons interacting

within the source, sheets of lead were folded into a horseshoe and mounted over the source/sample holder. The horseshoe, which is held in place by gravity, shields the detectors from the source with a thickness of 1.1-in of lead, which attenuates the 511 keV annihilation photons by 90%. A sheet of lead was mounted vertically behind the detectors to decrease the amount of background counts and pile up. Finally, the vacuum chamber provided some attenuation as well. The 8-in flanges that were machined as described in Section 2.3.1 attenuate some of the source annihilation photons; however, the flanges only appreciably attenuate photons that do not interact with machined portion of the flange.

## 2.9 Experiment Layout

Figure 26 shows how the equipment listed above was organized to create the PAS laboratory for this experiment. For the purposes of this experiment, the direction along which the positron beam is to be propagated is defined as the beam axis; and the axis that connects the centers of the detector faces is termed the detector axis. The remaining axis is defined as the vertical axis. All axes are labeled in Figure 18 on the picture of the vacuum chamber.

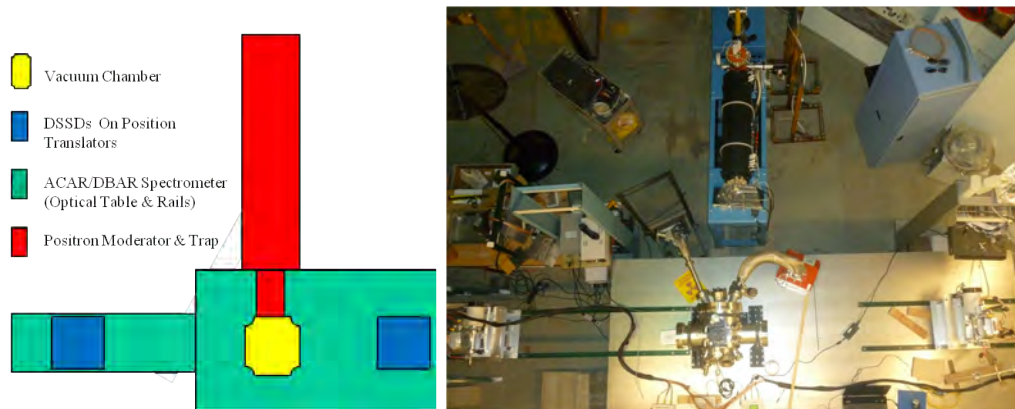


**Figure 26.** A diagram and a picture of the equipment layout for the new positron annihilation spectroscopy (PAS) laboratory, which was designed and built in this experiment.

### III. Laboratory Design Tasks

This chapter describes the design tasks necessary to integrate major components (from Chapter II) into a 3DPASS. First to be discussed is the design of equipment to elevate different components of the PAS laboratory. Next, the ultra-high vacuum (UHV) surface science chamber design and the alignment of the components of the laboratory relative to the chamber are discussed. Finally, the design and supporting calculations of the utilities for the First Point Scientific, Inc. positron beam system (FPBS) are outlined followed by the same information for the positron propagation interface (PPI).

#### 3.1 Elevation Components

Several components needed to be designed to allow for the proper alignment of the equipment listed in Chapter II. The vacuum chamber that was mounted on top of the optical table was the limiting factor in this design due to the inability to lower the chamber to the height of the other components. The first to be designed were the identical detector mounting platforms. Each of these was designed to support approximately 100 lbs with less than 0.05-in deflection of the plates. The design of these mounting platforms was accomplished using SolidWorks<sup>®</sup>. Each mounting system has the ability to be adjusted along three axes. Additionally, a 1/4-20 breadboard was built into the top plate of the platform to allow attachment of equipment that could be used in future research. Finally, the mounting system also included supports for lead sheets placed behind the detectors and the detector cables, which go from the PHDs DSSD preamps to the Spec72.

To align the positron beam with the sample location inside the vacuum chamber, the FPBS was elevated to the height of the vacuum chamber located on the optical

table. The AFIT Machine Shop fabricated eight 2 x 2 x 8-in supports that bolted into the bottom of the RGM-1 and the APBS components of the FPBS. The adjustable feet of the FPBS allowed for the precision alignment of the centerlines of the FPBS beam axis and the vacuum chamber beam axis.

### 3.2 Vacuum System Design

The vacuum system as outlined in Section 2.3.1 was designed to be expandable. For the first iteration, a target ultimate pressure was chosen to be  $10^{-6}$  torr for several reasons. The first was that the vacuum pressure at the emission point of the positrons from the APBS is on the order of  $10^{-6}$  torr. Another reason for choosing this ultimate pressure was the fact that an ion vacuum pump was not readily available nor was it within the budget of this project. Given the two turbo molecular pumps that were available, an achievable vacuum level is on the order of  $10^{-7}$  torr; however, the limit of the lone Viton gasket on the chamber is worse than  $10^{-6}$  torr. The ultimate pressure that was achieved with the current setup was  $1.1 \times 10^{-5}$  torr.

Minimizing the pressure of the vacuum system was an important design task in order to increase the number of positrons from the FPBS incident on the sample. Due to the geometry of the system, the positrons from the FPBS were forced to propagate a distance of approximately 1 m to reach the sample location. In the previous design, the propagation distance was on the order of cms. The mean free path (MFP) of the low-energy positrons of the FPBS was shorter than the mean MFP of positrons from the unmoderated  $^{22}\text{Na}$  sources. This is because the positron MFP is dependent on the material density of the medium in which the positron travels.

One of the more important aspects of the vacuum system was the thickness of the 8-in flanges that faced the detectors. The thickness of the flanges was determined to be 10 mil (0.01-in) for two reasons. One, the AFIT machine shop had the ability



to modify the flanges quickly; and two, a 10 mil thickness was able to withstand the pressures of the desired ultimate vacuum. The diameter of the hole that was bored into each of the 8-in flanges is 1-in. The solid angle from the bored hole to the assumed point source at the center of the vacuum chamber is larger than the solid angle from the center of the vacuum chamber to detectors; therefore, the detectors have a direct line of sight from any point on the detector crystal through the 10 mil thick portion of the flange to the sample location.

A second iteration of the vacuum system was designed to improve the control of the sample, decrease the ultimate vacuum, and decrease the attenuation of annihilation photons to the detectors. The second design involves replacing the current sample/source holder on the top 8-in flange of the vacuum system with a horizontally mounted load lock assembly connected to the 6-in flange on the back of the vacuum chamber. The load lock assembly would be able to hold 2-4 samples and be motorized to rotate between the samples. Additionally, the samples would be able to be adjusted plus or minus 0.5-in in any direction within the chamber.

### **3.3 Utilities Design**

Designing the compressed air and chilled water utilities to operate the FPBS invalid extensive calculation and setup. Operation of the FPBS requires 240V power, building water, and pressurized air. Appendix E shows the breakdown for each utility for the components of the FPBS. Although Building 470 has central water and pressurized air, the dome lab space did not have access to these utilities. The only approved method to bring water and air into the dome is through the experimental rabbit ports that connected the lab area to Room 105 in Building 470. With a means of getting air and water into the dome, the remainder of this section will discuss the design and construction of the water and air utilities done for this research.

The first task in designing the water and air utilities was to figure out the cooling water requirements so an appropriate sized chiller could be procured. Temperature and flow rate measurements were taken on the FPBS located in Agoura Hills, CA at First Point Scientific, Inc. The data was used to calculate the total chilling power necessary operate the beam system, which was determined to be approximately 6 kW based on the supporting calculation in Appendix B. Money was not available to purchase a chiller with the minimum cooling power, and building water was not able to be piped from the soft water tank located in the basement due to insufficient pressure. A 10.6 kW recirculating chiller was found and donated by the DTRA TEAMS site in Kirtland AFB, NM. The operating safety requirements of the chiller required it to be placed in the basement. Three-phase, 240 V power was installed to operate the chiller. After installation, the chiller was flushed five times and filled with softened water from the building water supply.

The task that remained was to design the plumbing that would go from the chiller to the four components of the FPBS in the dome. The plumbing system had nearly identical supply and return lines that went from the basement through ports in the floor into Room 105 and then into the dome. The lines to and from the basement are made of polyester reinforced flexible PVC hose connected by two 3-way brass valves that created a bypass such that water flow into the dome can be turned off when the beam is not in operation. The water flow enters the dome via another run of reinforced hose. The supply water flow is then split into four nylon tubing lines, which are each equipped with a bellows valve on the supply line and a flow meter on the return line to monitor and control chilled water flow to an individual component. After the flow meters, the four return lines are combined and exit the dome to Room 105. The total length of plumbing needed to reach all components of the FPBS was approximately 200 feet. The design of the plumbing of the chilled water was limited

by the pressure and temperature ratings of the polyester reinforced flexible PVC hose, which are 250 psi and approximately 160°C, respectively.

The design of the pressurized air utility was driven by the 70 psi necessary to pneumatically activate the gate valves of the FPBS. Three pressurized bottles of dry N<sub>2</sub> gas were bought to provide the pressurized air. N<sub>2</sub> was used because of the added benefit of being used as a backfill gas for the vacuum chambers in the laboratory when not in use. The deliver system of the pressurized nitrogen is a combination of 0.25-in nylon tubing and compression fittings with a maximum pressure rating of 250 psi.

### 3.4 PPI Design

The positron propagation interface was designed to maintain a small diameter positron beam from the output flange of the FPBS to the sample location in the vacuum system. The finalized design relies on calculations (Appendix C), that account for several competing aims:

- Minimize positron beam diameter at the sample location
- Satisfy the geometry requirements of the vacuum chamber and optical table
- Operate in high vacuum (HV) to UHV environment
- Minimize cost of the components to build the interface

The physical dimensions of the vacuum chamber and optical table were the primary limiting factors in the design of the PPI. The most cost-effective way of maintaining the beam integrity with minimal divergence was building a series of air-cooled electromagnetic coils. At the point of emission from the FPBS, the positrons are emitted from a vacuum on the order of 10<sup>-6</sup> torr and are required to travel 24-in to reach

the input flange of the vacuum system and an additional 10-in to reach the sample location. A design using a solenoid coil and a Helmholtz coil pair was chosen to satisfy the geometry constraints of the 3DPASS vacuum chamber and optical table.

The solenoid coil was designed to provide a uniform magnetic field to propagate the positrons from the output flange to the vacuum chamber input flange. The coil was made 24-in long from UHV-capable material, which was a 1.5-in OD 304SS reducing nipple. After winding of the coil, the active part of the solenoid coil was 22.5-in in length.

A Helmholtz coil pair was the best option to provide a relatively uniform magnetic field in the MDC surface science vacuum chamber. The coil pair was designed to fit around the chamber, which forced the dimensions to be 16-in ID of each 2 x 2-in coil with a inner spacing of 11-in between the coils. The coils are not a true Helmholtz coil pair because the separation distance between the coils does not equal the radius of each coil. Because the separation distance of the coil pair is larger than the radius of an individual coil, the magnetic field will not be uniform between the coils. Rather, there will be a dip in the magnetic field strength at the center of the coil pair similar to a double hump.

The heat created by running current through the coil wires needs to be dissipated so the coils can operate continuously or at a high duty cycle. To improve the speed of heat transfer from the center of the coils, rectangular Cu wire was chosen to wrap the coils because the rectangular wire creates fewer air gaps between the wounds of the wire. The air gaps act as insulators, which have a lower heat transfer coefficient than the Cu wire. To further decrease the number of air gaps in the coils, silicon thermal conductive paste was applied between the layer of wire wounds within the coils. The paste, which has a higher heat transfer coefficient than air, increased the operating times of the coils.

With the coil dimensions and materials set, an iterative design process was used to optimize the other characteristics of the electromagnetic coils. The design constraints for the Helmholtz coils was the amount of Cu wire that could be bought for under \$3000, which was a purchasing limitation. Two 1800 ft rolls of 0.065 x 0.132-in rectangular Cu wire were purchased for this price. Therefore, each coil of the Helmholtz pair would hold 390 wounds on the 2 x 2-in frame. The wire for the solenoid was not constrained so could have 173 winds per layer with a minimum of 2 layers.

The next step of the design process was to satisfy the necessary design constraint that the magnetic field at the sample location be approximately 120-140 gauss. Using an initial current of 10 A, the power and magnetic fields were calculated for the solenoid coil and Helmholtz coil pair. The magnetic field calculation allowed the positron beam diameter to be approximated. The initial calculation resulted in a positron beam diameter of approximately 4 mm, which was smaller than the sample dimensions to be used in the experiment. The power result was used to estimate the heat transfer to air cooling the coils. With the beam diameter heat transfer requirements satisfied, a power supply was procured that would have dual outputs, be able to provide the wattage to drive each coil, and be cost effective. The Sorenson power supply that was bought has a limit of 420 W output per channel.

Based on the power calculations, the amount of heat generated by the coils was calculated using the assumption that the ambient temperature is 25°C. To endure safe operation of the coils, the heat created by each coil must dissipate to the air. The magnetic field and heat calculations were repeated until the optimal operating ranges were determined by balancing the maximum heat able to be dissipated by air cooling and optimizing the magnetic field at the sample by varying the coil design and current applied.

## IV. Positron Annihilation Spectroscopy System

### Characterization and Development

This chapter describes the methodology and procedures that went into developing and characterizing the 3DPASS. First is the discussion of the detectors and sample location alignment and calibration. Next, the energy calibration of the detectors is discussed followed by a discussion of the code development. Finally, the procedures for collecting the 2D-ACAR and CDBAR data spectra of Cu samples is mentioned.

#### 4.1 Alignment and Source/Sample Holder Calibration

Precise alignment of the detector centers relative to the sample location in the vacuum chamber was crucial to centering the resulting 2D-ACAR momentum space vectors. A leveling laser was mounted to the breadboard of the Detector 0 mounting plate. The laser was centered using a caliper such that the beam was also perpendicular to the detector face. The laser was carefully rotated  $180^\circ$  ensuring the beam remained level and perpendicular to Detector 0. Semi-translucent plastic sheets were mounted on each of the 8-in CF flanges of the vacuum system. Each sheet had a pinhole located at the center of the flange to allow for the laser to transmit through the vacuum chamber. The mounting system of Detector 0 was adjusted until the laser went through both plastic pinholes. Next, the mounting system of Detector 1 was adjusted until the laser beam was centered on the detector face.

The  $XYZ\theta$  source manipulator was calibrated with the source/sample holder attached. The actuators of the manipulator were adjusted along the detector and vertical axes, which correspond to the plane parallel to the detector faces. As the laser beam touched the edges of the source or sample windows of the holder, the corresponding numbers, which correspond to a physical location in the chamber, on the

actuators were recorded. The average of the two values in each direction determined the center location for each window. The center values for the source holder were determined to be 0.725 in the vertical axis and 5.0 in the beam axis. The values for the vertical and detector axis location for the center of the sample holder were 0.765 and 6.65, respectively.

## 4.2 Energy Calibration

The energy resolution for the PHDs detectors was determined by using the  $^{85}\text{Sr}$  source, T-142. A 30-hour data set was taken with T-142 located 15 in from each detector along the center line. The spectrum for each channel was then calibrated using the energy calibration feature of the Imager software. This calibration was then verified with a second 30-hour data set. These results yielded full-width at half maximum (FWHM) and full-width at tenth maximum (FWTM) values for the 32 channels in each detector, which can be seen in Table 1. Detector 0 had an average FWHM of  $1.92 \pm 0.21$  keV and an average FWTM of  $3.71 \pm 0.27$  keV, whereas Detector 1 reported a FWHM of  $1.84 \pm 0.16$  keV and a FWTM of  $3.72 \pm 0.28$  keV. The energy calibration data sets were limited to 30 hours due to the Imager software stopping data collection after that duration of time. Raw event energy data was not collected for these data sets. Two additional 24-hour data sets, which did collect raw event data, were taken using T-142 located in the center of the chamber while at vacuum to verify the energy resolution while at full vacuum.

## 4.3 Code Development

Much like the construction and design of the PAS laboratory, the code developed for this research is designed with future experimentation in mind. As such, the code is dependent on user inputs and is divided into three parts each with a specific purpose:

data parsing, subpixel efficiency calculations, and initial 2D-ACAR and CDBAR analysis. Constrained 2D-ACAR and CDBAR measurements are material- dependent and are outside the scope of the initial code development. In the following subsections, algorithms for the various codes are discussed. Appendices F-H present the actual code for parsing, efficiency calculations, and ACAR/DBAR analysis, respectively.

#### **4.3.1 Raw Event File Selection**

Initially, the PHDs Imager software was set up to output both raw energy event and energy filtered event files. The purpose of this was to determine the feasibility of utilizing the PHDs Co. proprietary interpolation scheme. Three 30-minute data sets, which recorded both data types simultaneously, were taken with a 2.2-m sample-to-detector baseline of the 3DPASS. The raw energy event file was parsed and analyzed for coincident full energy events in each detector. Seven such events were found and compared with the data from the energy filtered event file. The coincident events found in the energy-filtered event file indicated that four full energy events were recorded in coincidence but only listed two of the strips and subpixels combinations instead of four. Therefore, the deviation from colinearity could not be determined from this file type because only one of the two coincident annihilation photon locations was able to be calculated. Despite the larger file sizes, the raw energy event files were used for the remainder of the data analysis for this research. A comparison of the data file types can be found in Appendix A.

#### **4.3.2 Parsing Code**

The parsing code was written in two languages. The first data parser, written in Bash by Mr. Tony Kelly, took advantage of the data format of the raw energy event file as specified in Table 4. The second column of each line indicated whether



**Table 1. Energy Resolution Data for 3DPASS Using  $^{85}\text{Sr}$  17.5-in from Each Detector**

Detector 0				Detector 1			
Channel	FWHM [keV]	FWTM [keV]	Gross Area [counts]	Channel	FWHM [keV]	FWTM [keV]	Gross Area [counts]
0	2.08	4.31	9615	32	2.32	4.52	11708
1	1.88	3.89	14981	33	1.93	3.94	17134
2	1.82	3.75	19237	34	1.97	3.74	21010
3	1.93	3.76	23200	35	1.87	3.77	23934
4	1.84	3.52	24518	36	1.93	3.82	25569
5	1.86	3.53	25802	37	1.92	3.86	27122
6	1.75	3.43	25508	38	1.98	3.80	26821
7	1.79	3.48	25470	39	2.04	3.95	27100
8	1.83	3.46	25820	40	1.84	3.80	27164
9	1.83	3.56	26835	41	1.89	3.88	27104
10	1.79	3.42	25219	42	1.91	3.75	27211
11	1.71	3.46	23763	43	1.86	3.65	26093
12	1.71	3.50	21585	44	1.83	3.65	23576
13	1.96	3.85	17916	45	1.73	3.44	20928
14	1.76	3.72	13949	46	1.83	3.70	16681
15	2.05	4.02	7540	47	2.02	4.19	11624
16	1.84	3.75	11853	48	1.63	3.48	12341
17	1.54	3.20	17863	49	1.57	3.15	18776
18	1.97	3.60	21686	50	1.49	3.28	21678
19	1.93	3.56	25699	51	1.81	3.56	25188
20	1.79	3.44	26333	52	1.92	3.80	26582
21	2.39	4.15	27344	53	1.73	3.46	28296
22	2.20	3.98	27068	54	1.81	3.56	28544
23	2.14	3.80	26642	55	1.70	3.44	28714
24	2.53	4.30	27471	55	1.89	3.62	28136
25	2.18	4.04	28680	57	1.91	3.89	28792
26	1.75	3.54	27636	58	1.70	3.50	28465
27	1.81	3.55	26551	59	1.73	3.50	27065
28	2.00	3.82	24737	60	1.96	3.91	24694
29	2.12	3.95	21404	61	1.82	3.58	22288
30	1.81	3.48	18459	62	1.79	3.60	18517
31	1.77	3.79	11501	63	1.61	4.26	12514

the energy event was coincident in one, two, three, or more strips. The number of strips that were a part of a particular event depended on how many clock cycles (20 ns per clock cycle) the strip fired after a signal was detected in the first strip. For the purposes of this research, only two- and four-strip event were used.

Two versions of the Bash script were written. One parsed two-strip events to be used in relative efficiency calculations, and the other did the same for four-strip events. The effect of limiting data analysis to two- and four-strip events was to account for only full energy events in the DSSDs, which equate to the hole and electron pair created by a photon interaction with the HPGe crystal being coincident in only two or four strips. This thereby ignored the possibility of charge sharing events in adjacent strips. The Bash parser scanned the raw energy event file for events with a 2 or a 4 in the second column and saved them to a file with the extension *.2.phd* or *.4.phd* respectively.

Next, a series of MATLAB<sup>®</sup>scripts, which could parse two- and four-strip events, were written to further parse the data based on energy and timing information. The energy window and coincident timing limit were set to  $511 \pm 30$  keV and 10 clock cycles (200 ns). Next, the files saved from the Bash parser were read in blocks of two or four lines. If the energy and time criteria were met, the block of data was used to calculate the subpixel position number,  $N_{subpixels}$ , via

$$N_{subpixels} = N_{substripsperpixel} \left[ N_{channel} + \frac{FOM_{successor}}{FOM_{successor} + FOM_{predecessor}} \right] \quad (2)$$

where  $N_{substripsperpixel}$  was the user defined number of substrips per pixel,  $N_{channel}$  was the channel/strip number of the event,  $FOM_{successor}$  was the FOM of the adjacent strip or channel with a higher number, and  $FOM_{predecessor}$  was the FOM of the adjacent strip with a lower number. Otherwise, the block was ignored.

After stepping through all of the files in the folder, two matrices were saved.

The first matrix included only the raw energy events that met the energy and timing criteria. The second data matrix for the two strip events included the subpixel location in the AC strip, subpixel location in the DC strip, average energy of the AC and DC strip, and number of clock cycles between the event in each strip. For four-strip events, the subpixel and energy information was listed for Detector 0 followed by the subpixel and energy information for Detector 1 and then by the timing information.

The parsing code monopolized the bulk of the computational power and processing time due to the necessity of reading the data files line by line. The Bash script, which took 5 - 15 minutes to execute, significantly helped to reduce the data processing time for 24 hours of data for four-strip events from eight hours to fifty minutes on average. The processing time for a 24 hours data file for two-strip events took 2.5 - 3 hours. The previous 3DPASS analysis code took more than 10 hours to process 24 hours of data, which parsed the data into 1125 sub pixels versus 9800 sub pixels for this research.

### 4.3.3 Relative Efficiency Calculations

The code that calculated the relative subpixel efficiencies used both two- and four-strip subpixel data to generate relative efficiency matrices for each detector. The subpixel data set of all the events of  $511 \pm 30$  keV was parsed to create a matrix of the total number of events observed in each detector. The subpixel data from the outer strips of each detector crystal were removed because of the lack of either the predecessor or successor FOM. The outer pixels near the curved portion of the circular crystal were removed due to their smaller size and the untested accuracy of the FOMs from adjacent strips. The removal of the outer pixels and strips was termed the filtering mask. A bivariate histogram for each detector was created using a vector that defined the edges of the subpixels. Finally, the histograms and mask

matrices were saved to be loaded and manipulated by the ACAR/DBAR analysis code. User inputs to the efficiency code are available to limit the acceptable energy and time criteria used to create the matrix and to plot the normalized and cumulative histograms.

#### 4.3.4 2D-ACAR and CDBAR Analysis Code

The initial analysis for 2D-ACAR and CDBAR measurements used the subpixel data set for the four-strip events and the same data filtering mask as the relative efficiency calculations. For the 2D-ACAR measurement, the code created and plotted normal and efficiency corrected bivariate histograms for the coincident events that occurred in each detector. Also, the option of plotting one dimensional histograms was available as well as plotting the coincident response of each detector. The detector histogram and mask matrices were loaded, and relative efficiency values were calculated and assigned to each subpixel coincident event in each detector.

Three efficiency methods were investigated. The first was a relative efficiency based on the maximum sub pixel count in each detector. The maximum relative efficiency method resulted in a matrix of values between zero and one. The second method used the mean of the sub pixel counts in each detector, which created a mean efficiency matrix with values greater than zero. The final method normalized the subpixel efficiencies pixel-by-pixel. This allowed each pixel to have a maximum value of one.

The deviation from colinearity was calculated in both X- and Y-directions. A bivariate weighted histogram function, which accounted for the subpixel efficiency values, was used to create the final 2D-ACAR matrix. The subpixel relative corrections were created by multiplying the number of counts of a particular value of the

deviation of colinearity by

$$\frac{1}{\epsilon_0 \epsilon_1} \quad (3)$$

where  $\epsilon_0$  or  $\epsilon_1$  was the relative subpixel efficiencies for Detector 0 and Detector 1.

For the CDBAR measurement, the bivariate weighted histogram was used to correct for subpixel efficiencies via Equation 3 and create the CDBAR data in the format as the plots in Figure 10. Next, the CDBAR data pulled out the diagonal profile from the data using equation 4

$$E_0 + E_1 = 1022 \pm \Delta \quad (4)$$

where  $E_0$  and  $E_1$  were the energy of the coincident detected in Detector 0 and 1 respectively, 1022 is the rest mass energy of a positron and electron in keV, and  $\Delta$  was the width of the line shape extracted from the CDBAR spectrum in keV. The width,  $\Delta$ , was approximated to be the optimized value from Williams, which was 0.4 keV [30].

#### 4.4 Cu Sample Coincident 2D-ACAR and CDBAR Experiment

Cu was chosen to collect annihilation radiation spectra because the 2D-ACAR distribution of the (100) orientation is nearly symmetric about the zero momentum axes as shown in previous work outlined in Chapter I. Two different source configurations were used to collect a copper spectrum. The first configuration used the source/sample holder discussed in Subsection 2.3.4. The holder was populated with the source, T-132 was used to isotropically radiate a highly polished Cu sample as described in Section 2.7. For this configuration, a total of 17 days of data was collected at the 6.65 setting on the beam axis actuator and the detectors 2.2 m from the sample. The data contained 2063 coincident counts. Given the 2.2-m baseline and the use of a five

subpixel interpolation technique, the angular range and resolution of each detector was calculated to be  $31.6 \times 31.6$  mrad and 0.455 mrad, respectively.

The second configuration involved the use of the CuSS as the source and the sample. The CuSS was placed in the sample holder and was re-aligned using the procedure as described in Section 4.1. The XYZ $\theta$ -manipulator was set to 0.765, 6.45, and 5.00 for the vertical, beam, and detector axes, respectively. The CuSS was placed at a 45° angle to the detector axis to mimic the setup from the first configuration and the previous work done by Williams [30]. A data set was taken for 17 days using the CuSS at a distance of 2.0 m from each detector. A total of 37,516 coincident counts were detected in the 17-day period. For the 2.0 m baseline, the angular range increased to  $34.75 \times 34.75$  mrad with a slightly increasing angular resolution of 0.5 mrad. During the 17-day data set, approximately  $5.5 \times 10^6$  counts with energies of  $511 \pm 30$  keV were recorded by one of the two detectors. Efficiency matrices were calculated using the methods outlined above.

## V. Analysis of Results

This chapter comments on the overall performance of the 3DPASS system and the data processing and analysis code. Analysis of the 2D-ACAR and CDBAR measurements of Cu is also presented in two parts. First, the results of the first configuration using the sample/source holder are discussed. The analysis of the second configuration of the CuSS follows and includes a comparisons of the efficiency methods used. Also, the analysis of the CuSS presents comparisons between the original 3DPASS and new 3DPASS used in research.

### 5.1 3DPASS Comparison

When compared to the original 3DPASS, the new system had many improvements, which are summarized in Table 2. However, the count rates of coincident annihilation events were an order of magnitude lower using the new system. The most likely cause of this was a combination of factors. First was the increase in thickness of the steel, through which annihilation photons were required to travel. The thickness was 66%

**Table 2. Comparison of original 3DPASS [30] and 3DPASS built for this research**

Metric [Units]	Original 3DPASS	Current 3DPASS
Ultimate Vacuum [torr]	1.0	$1.1 \times 10^{-5}$
Angular Range [mrad x mrad]	7.5 x 7.5 (Ortec DSSD) 15.0 x 15.0 (PHDs DSSD)	34.75 x 34.75
Angular Resolution [mrad]	0.5	0.5
Vacuum Wall Thickness [in]	0.006	0.010
Energy Resolution [keV]	$1.76 \pm 0.24$ (Ortec) $1.49 \pm 0.17$ (PHDs)	$1.92 \pm 0.21$ (D0) $1.84 \pm 0.16$ (D1)

larger in the new 3DPASS. The attenuation of the 511 keV annihilation photons is increased by 0.7%, which hardly makes up for the decrease in count rates.

The next potential cause was the loss of coincident events due to mechanical vibration of the coolers for each detector. Vibration from mechanical coolers was not a factor in the liquid nitrogen detectors used in the 3DPASS by Williams [30]. In fact, the vibrations in the detector crystal were likely increased due to attaching the detectors to the mounting systems described in Section 2.1. Data was not collected with the detectors mounted and free of the detector mounting systems. Therefore, the contribution of the vibrations to the coincident event count rate were not determined.

The configuration of the detectors also may have contributed to the decreased coincident count rate. As reported previously by Williams and Stevenson, the AC side of the PHDs Co DSSDs has a higher efficiency [22, 30]. However, the detectors were not arranged such that the AC sides faced the vacuum chamber. Rather, the DSSDs were oriented the way they were characterized by the manufacturer. This had the AC side of Detector 1 pointing toward the vacuum chamber and the AC side from Detector 0 facing away from the vacuum chamber. This issue was not considered to be a problem, but in retrospect, this may have caused a decrease in the coincident count rate of the detection system.

Finally, the largest contributor to the decreased coincident count rate was the degradation of the  $^{22}\text{Na}$  source. The  $^{22}\text{Na}$  source used to isotropically radiate the sample was the same source used in previous work [30]. The activity had decreased by 40%, which contributes significantly to the amount of positrons available to interact with the Cu sample.

The energy resolution of the new 3DPASS was also higher than the previous system. The increase in energy resolution of the new 3DPASS anticipates the degradation of the CDBAR measurements. This is possibly the result of the addition of



the mechanical coolers, which add vibration to the detector crystal. It is also possible that the energy resolution in Detector 0 is higher due to the fact that the AC side of the detector was further from the source.

## 5.2 T-142 Source Configuration Results

The analysis of this data using the code in Section 4.3.4 shows a double peak in the deviation from colinearity shown in Figure 27. The double peak appears along the beam axis, which is caused by the number of coincident counts being skewed toward

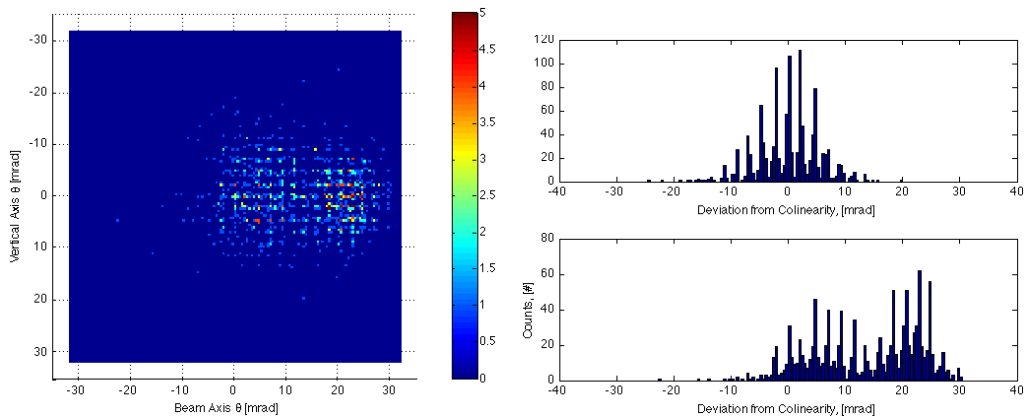


**Figure 27.** Histogram plots of the deviation from colinearity using a Cu sample location of 6.65 and T-142 as the isotropic source (not corrected for sub pixel efficiency). The bivariate histogram is to the left, while the right has the histograms projected onto the vertical axis (top, right) and beam axis (bottom, right).

the positive beam axis direction in both detectors, which is shown in Figure 28. The low coincident count rate and double peak of the of the deviation of colinearity along the beam axis was interpreted as resulting from a misalignment of sample and detectors along the detector axis. To test this, a series of 1 - 2 day data sets were collected at different beam axis locations to verify the misalignment hypothesis. Table 3 shows the settings that were used for this part of the calibration. The results of these tests are shown in Figure 29. The normalized projected histograms of the deviation

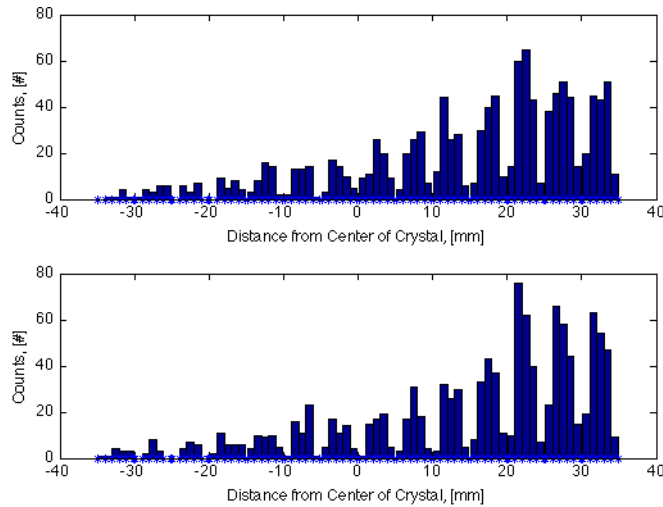


**Figure 28.** Projected histograms of the coincident response of Detector 0 (top) and Detector 1 (bottom) showing the source contamination of the detector (not corrected for sub pixel efficiency).

from colinearity clearly show that the detector data was skewed toward the positive beam axis.

**Table 3. Summary of Data Sets Collected Varying Sample Location**

Beam Axis Sample Location	Duration of Data Set [Days]	Number of Coincident Annihilation Events [counts]	Coincident Event Count Rate [counts/hour]
8.6	1	41	1.71
6.65	17	2063	5.06
5.6	1	211	8.79
4.6	2	455	9.48
4.0	2	443	9.23
3.0	1	234	9.75
2.6	1	270	11.25
6.65 w/ Pb	14	613	1.82

The coincident count rate of the detectors also increases as the source moves closer to the center of the vacuum chamber. A ray trace of the geometry of the system explains this phenomenon. The source is only partially shielded from the detectors.

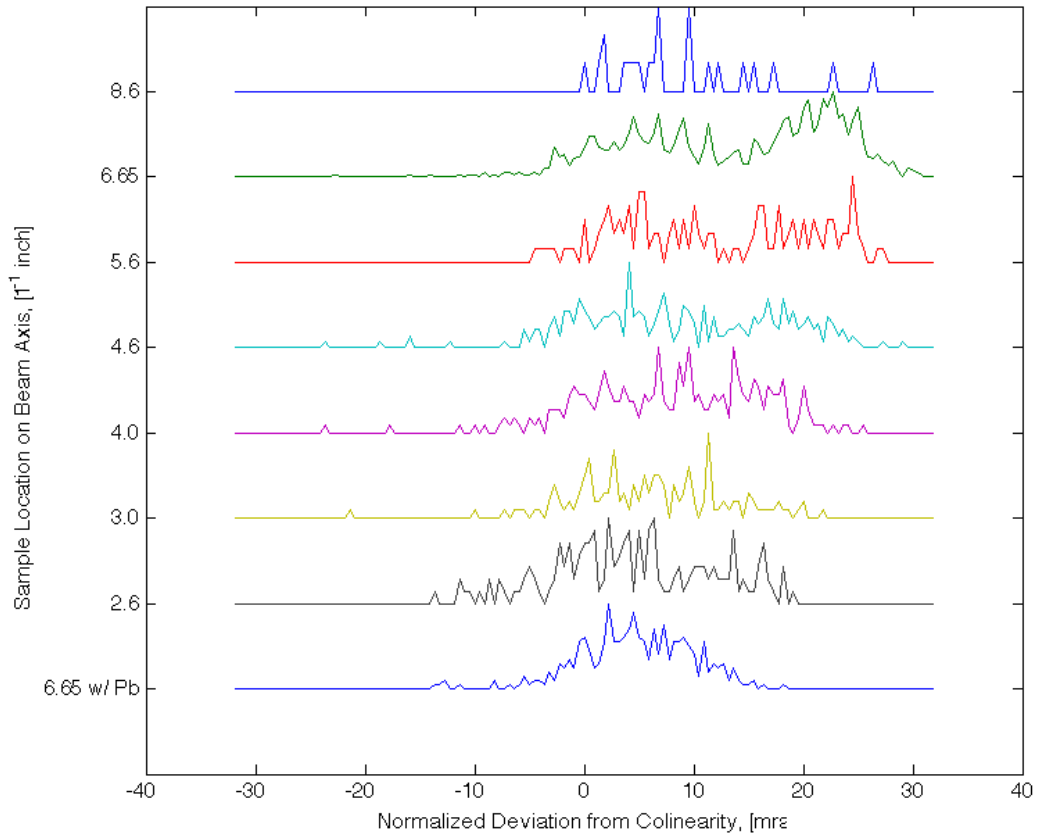


**Figure 29.** Normalized histograms of the deviation from colinearity projected onto the beam axis using a Cu sample and T-142 source placed in the sample/source holder, which was moved to different beam axis locations (not corrected for sub pixel efficiency). The y-axis represents the actuator setting for the XYZ $\theta$ -manipulator in the beam-axis direction, which is in units of  $10^{-1}$ -in.

The 1-in hole bored into the 8-in flanges acts as an aperture that allows annihilation photons to travel with minimal attenuation from the source/sample holder to the detectors. The part of the flange that is not machined is thick enough to attenuate 80% of the 511 keV photons. Therefore, the annihilation events that occurred within the source is contaminating the data. This is termed source contamination and is due to insufficient shielding inside the vacuum chamber near the source. A lead horseshoe placed over the source significantly decreases the contamination; however, this further decreases the count rate of the coincident annihilation events, which is shown in Table 3. The number of coincident annihilation events from Cu were not high enough to perform a timely and statistically significant set of 2D-ACAR and CDBAR measurements. This is the reasoning behind creating the CuSS and moving the detectors closer to the sample location from a distance of 2.2 m to 2.0 m.

### 5.3 Raw CuSS 2D-ACAR and CDBAR Results

The CuSS source improves the number of coincident events analyzed from 4330, which is a sum of all counts from Table 3, to 37,516. The improvement of the count rate makes a better statistical representation of the 2D-ACAR and CDBAR results and decreases the time needed to get statistically significant 2D-ACAR and CDBAR spectra.

The 2D-ACAR data can be seen in Figure 30, which shows the bivariate histogram for the 17-day data set. The 2D-ACAR data compares to published results (Figure 5 and Figure 31); however, the peak is centered slightly in the positive direction of the beam and detector axes. The exact difference between the peak and the origin cannot be determined without looking at a plot that is corrected for the sub pixel efficiencies, which are discussed in Section 5.4.

The CDBAR spectrum using same data set for the 2D-ACAR is shown in Figure

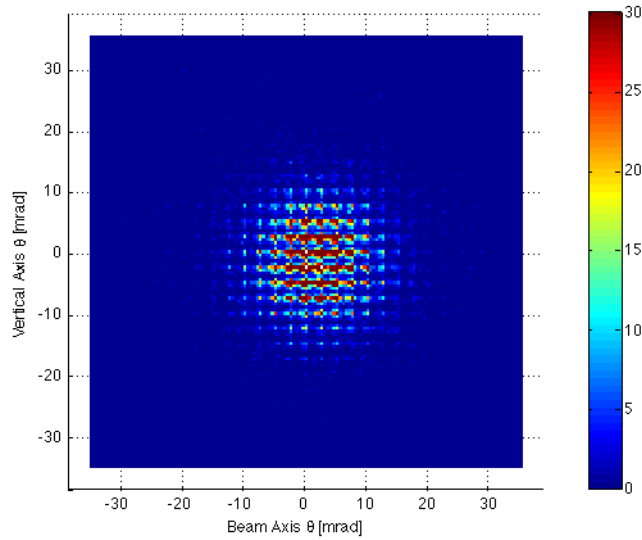


Figure 30. CuSS 2D-ACAR spectrum without subpixel efficiency corrections or data smoothing.

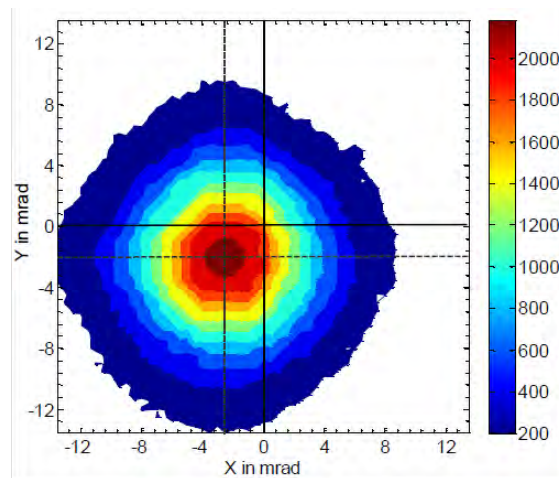
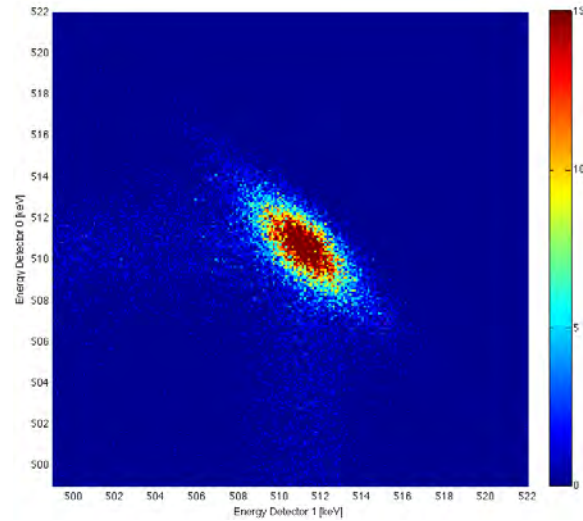


Figure 31. Single-crystal Cu 2D-ACAR contour plots reconstructed from the 3DPAMM data set. X and Y units are in mrad or  $10^{-3} m_0c$  (in momentum space) and Z is the number of counts [30].

32. This spectrum shows the bivariate histogram of the energies of coincident events in each detector. Figure 32 compares well Figure 33 because the density of counts



**Figure 32. CuSS CDBAR spectrum using the same data as the ACAR plots without subpixel efficiency corrections or data smoothing.**

decrease along the diagonal axis, which corresponds to coincident events in both detectors that sum to 1022 keV, or the rest mass energy of a  $e^+e^-$  pair. The DB lineshape also uses a  $\Delta$  of 0.4 keV in Equation 4. This was the optimum value calculated from Williams by minimizing the full-width at one hundredth maximum of the DB lineshape. The uncorrected DB lineshape, which can be seen in the black dots of the bottom plots of Figure 35, does not show the shoulder and neck features that are present in Figure 33.

#### 5.4 Subpixel Efficiency Correction Results

The efficiency of the subpixels decreases the farther the subpixel was from the center of the strip. Also, the subpixel efficiencies decreased as the strip size decreased toward the outer radial bounds of the HPGe crystal. The 2D-ACAR plots of the

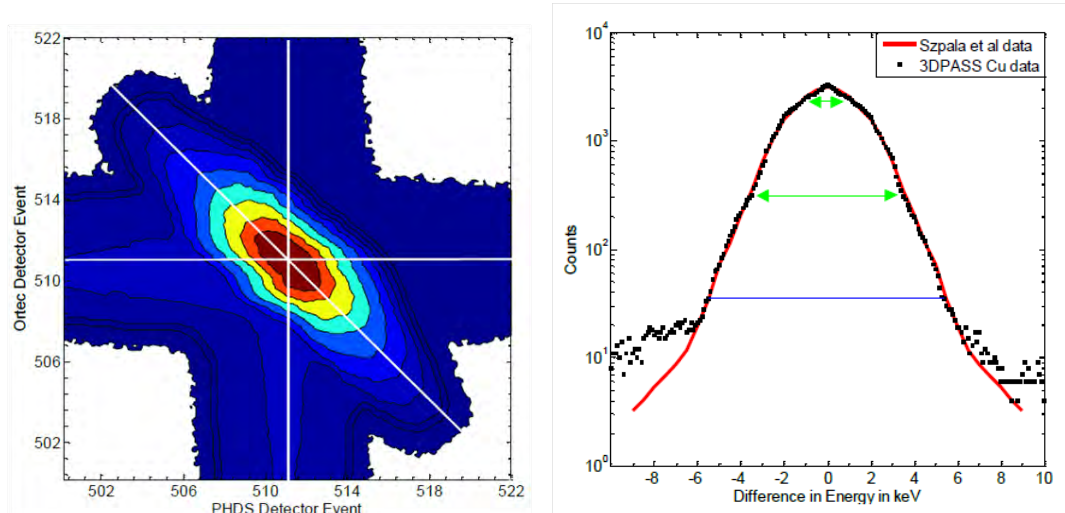


Figure 33. Single-crystal Cu CDBAR spectrum and DB lineshape for  $\Delta = 0.3$  keV compared to Szpala et als Cu DBAR results. (The blue lines indicated the FW(1/100)M in each DB lineshape and the green arrows indicated features observed in the momentum distributions) [30].

CuSS data set that was corrected for subpixel efficiencies using the methods from Section 4.3.4 are shown in Figure 34. The histograms do not show the expected

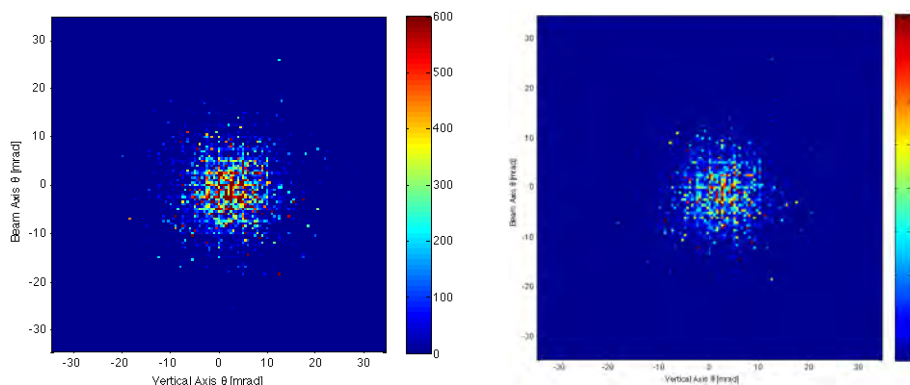
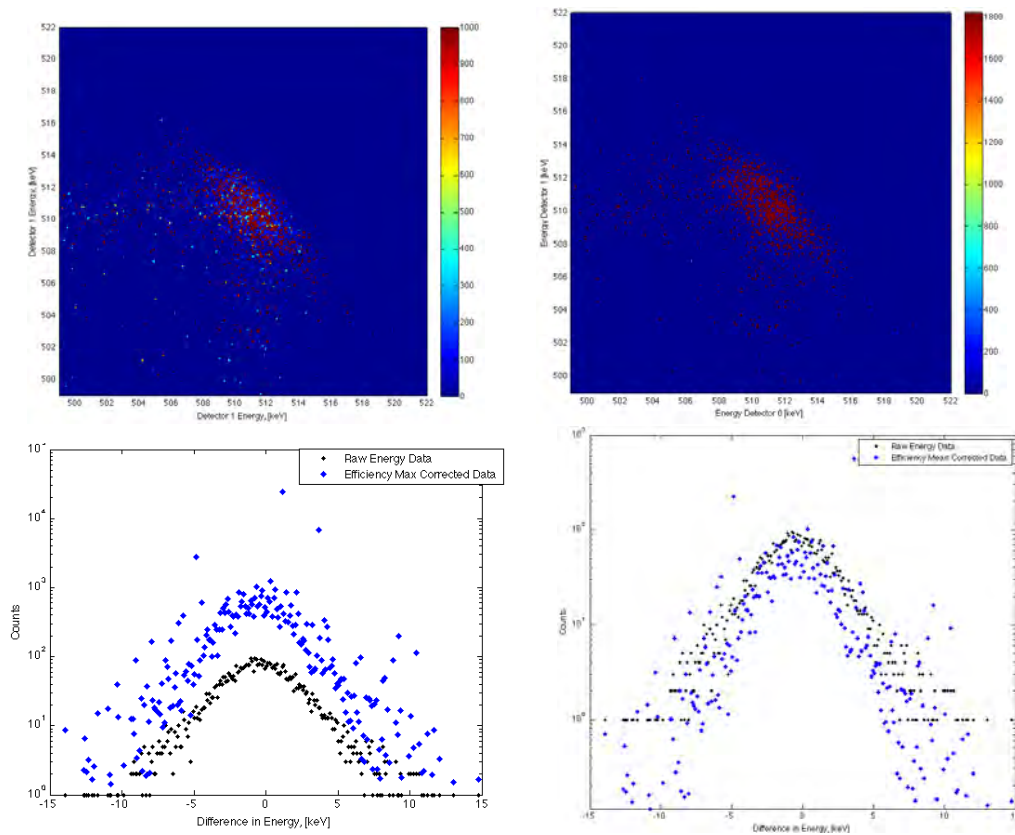


Figure 34. CuSS 2D-ACAR spectrum. Left: shows maximum subpixel efficiency correction method. Right: shows mean subpixel efficiency correction method. Mean and maximum methods are linearly proportional.

uniformly decreasing peak as shown in Figures 5 and Figure 31.

Similarly to the 2D-ACAR results, the efficiency-corrected CDBAR spectrum does

not compare well to published results. Figure 35 shows amplified error in the relative



**Figure 35.** CuSS CDBAR spectrum and DB lineshape for  $\Delta = 0.4$  keV. Left: shows maximum subpixel efficiency correction method. Right: shows mean subpixel efficiency correction method. Mean and maximum methods are linearly proportional.

efficiency corrected spectrum, which is introduced by the low number of counts in some subpixels. Additionally, the only difference between the maximum and mean efficiency correction technique is the magnitude of the number of counts for a given subpixel location. The data itself does not change. Similar results are observed for all relative efficiency correction schemes used in this research.

When the coincident responses for each detector are projected onto the vertical and beam axes, Figure 36, the result is that the center eight strips, which are the full-length strips, have a uniform response as expected; however, the outer strips are



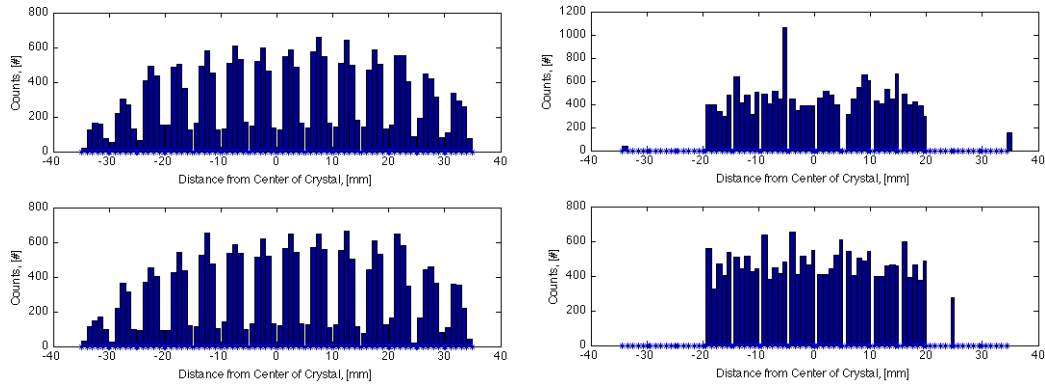


**Figure 36.** Comparison between raw detector response of coincident events from CuSS (left) and the subpixel efficiency corrected detector response of the same events using the mean efficiency method (right). The plots show the beam axis projections for Detector 0 (top) and Detector 1 (bottom).

not uniform or are near zero. This means that the efficiency technique, which was developed using square pixel arrays, does not work for the non-square pixel arrays that result from using the entire PHDs DSSDs crystal. The methods for accounting for the subpixel efficiency did not have enough counts per subpixel to correctly account for the efficiency loss at the edges of a strip.

## VI. Conclusions and Future Work

### 6.1 Conclusions

All of the utilities and support equipment that were necessary to get the First Point Scientific, Inc. positron beam system operational were acquired. A water chilling system was devised and constructed which can provide a maximum of 10.6 kW of cooling power and withstand water pressures of 200 psi and less. Bottled dry N<sub>2</sub> was procured to provide pressurized air and backfill for vacuum systems. Most importantly, two capsule <sup>22</sup>Na sources were acquired via donation. Without the capsule sources, the positron beam system can not be operated. Although the FPBS was never turned on during this research, all of the tools were assembled to be utilized by the next project, which is set to begin in April 2012.

The second objective was to design and build an interface to propagate positrons from the FPBS to the sample location within the vacuum chamber. The design aspect of this goal was achieved as described in Section 3.4 and Appendix C. The construction of the PPI took longer than expected due to the difficulty in obtaining permission to buy the thermal compound necessary to wind the coils. As such, the coils were wound but not attached to the FPBS and vacuum chamber. Therefore, the magnetic fields generated by the PPI could not be measured and characterized for this research.

The third objective was to recreate and characterize the 3DPASS. The system was successfully constructed and characterized but not optimized. The results from the Cu source and sample showed that the system was aligned properly and that the subpixel interpolation scheme, which was a slight variation from the method developed by Williams, worked as designed. The efficiency correction scheme requires further development. The correction worked well for the center eight strips of the AC

and DC sides of each detector, but did not correctly account for the remaining strips that were not equal in length to the center eight. Limitations were encountered developing alternative methods due to the low statistics achievable in each channel with the sources available.

Finally, the data processing and analysis code was written in a flexible manner to be expandable for future improvements. The code improved the data parsing times as mentioned in Section 4.3.2.

## 6.2 Future Work

This research has assembled and created all the tools necessary to create a modern PAS laboratory capable of providing 3DPAMM using a low-energy positron beam. In light of this, there are many possibilities for future work using the PAS laboratory and work that can be done in support of development and improvement of the system.

The final integration of the FPBS into the PAS laboratory should be accomplished. This requires several key tasks including a detailed measurement of the magnetic fields of the PPI using a gauss meter, measurement of the positron beam diameter at the sample location using a CCD camera, detailed measurements of the positron energy profile at the sample location, and optimization of the chilled water flow rates to allow for continuous operation of the FPBS.

The 3DPASS should be used to take 3DPAMMs of other materials to compare with published 2D-ACAR and CDBAR measurements. Some previously characterized materials that can be used to validate the current setup are 6H SiC, which can be used to compare with measurements as made Williams [30]; silver-doped and pure lithium tetraborate, to compare with work done by personnel at AFIT [6, 27]; and URb<sub>2</sub>Si<sub>2</sub> [5, 20] or single-crystal uranium, which would show the ability of the system to provide a detailed characterization of high  $Z$  materials. Also, a comparison of 3DPAMMs

taken on similar materials using different positron sources should be accomplished using an intravacuum isotropic source and the FPBS.

Future work on the improvements of the PAS laboratory should be done as time and money allow. A new sample holder with an optional slot for an intravacuum source or magnet should be developed to be integrated with the vacuum system. It should preferably have a load-lock assembly to provide efficient exchange of samples and sources. At a minimum, the current XYZ $\theta$ -manipulator should be machined to allow for the use of a Cu gasket at the interface with the vacuum chamber. Currently, only a Viton<sup>®</sup> gasket can be used which limits the ultimate vacuum of the chamber. Additionally, the vacuum can be improved by using adding an ion pump to the chamber system. Another potential improvement is the addition of water cooling to the electromagnetic coils in the PPI. This would allow the coils to be operated at higher currents, which would decrease the spot size of the positron beam at the sample.

Other additions can be made to the 3DPASS that would further the scientific breadth of experiments to be conducted in the PAS laboratory. An electron energy spectrometer would allow for PAES measurements to be accomplished. An extra HPGe detector behind the current DSSDs would allow for coincident Compton rescue measurements, which would increase the overall efficiency of the 3DPASS. Each of these additions would require modifications to the analysis code and potentially the PPI to provide optimal measurements.

Finally, some computer models are needed to compare with experiments done using the PAS laboratory. Quantum mechanical models should be developed in parallel to experiments done. These model calculations should be designed to map the electronic wave function of the material lattice in question, any vacancy defects of the

material, and the positronic wave function, which together can make  $e^+e^-$  momentum approximations to be compared with 3DPAMMs.

Also, a detailed MCNP or GEANT4 simulation should be written to model the PAS laboratory. At a minimum, a standard model of the geometry of the vacuum setup, FPBS, and detectors needs to be written to provide an estimate of necessary count times given the input of different materials. The above models would provide theoretically sound characterizations of the PAS laboratory and its components, which could then be experimentally reinforced.

## Appendix A. PHDs Imager Software Data Format

### Comparison

The Imager software created by PHDs Co. has three possible data logging formats: raw data, raw energy event data, and energy filtered data. Table 4 and Table 5 show the raw energy event and energy filtered data formats used in this research.

**Table 4. Imager Raw Energy Event Data Format**

Data column	Data type
1	Sequential number of hit within event
2	Total number of hits in event
3	Number of clock cycles since trigger (first hit)
4	Channel number of hit
5	Calibrated energy deposition
6	Predecessor FOM
7	Successor FOM

**Table 5. Imager Energy Filtered Event Data Format**

Data column	Data type
1	Event Number (Starting at 0)
2	Total number of hits in event
3	AC Channel number of hit
4	AC slot or subpixel number of hit
5	DC channel or strip number of hit
6	DC slot or subpixel number of hit
7	Crystal interaction depth
8	Average energy of the event
9	Calculated AC predecessor FOM
10	AC predecessor FOM
11	AC successor FOM
12	Calculated AC successor FOM
13	Calculated DC predecessor FOM
14	DC predecessor FOM
15	DC successor FOM
16	Calculated DC successor FOM

## Appendix B. Chilled Water Calculations

This appendix outlines the methodology and calculations used to determine the cooling power requirements of the compressors and water-cooled electromagnetic coils of the FPBS. Cooling power estimates are necessary to provide safe and continuous operation of the FPBS and to determine the size of the recirculating chiller that can satisfy these requirements.

The water cooling requirements as estimated by the manufacturer, First Point Scientific, Inc. are listed in Table 6. To verify these values, flow rate and temperature

**Table 6. Water Cooling Estimates Assuming 22°C Water**

FPBS Component	Flow Rate	Pressure
Units	gpm	psi
Coldhead Compressor	0.75	30
Cryopump Compressor	0.75	30
Trap Magnet	1.00	60
TGM-1 Magnet	0.75	30

measurements of the supply and return lines of the FPBS operating in Agoura Hills, CA were taken. The chilling power requirements were calculated for each component of the FPBS using the acquired measurements and the basic equation

$$P = K \dot{f} \Delta T \quad (5)$$

where  $P$  equals the water cooling power,  $K$  is a conversion constant that accounts for specific weight and specific heat of the cooling liquid and conversion factors to get desired outputs,  $\dot{f}$  is the flow rate of the water, and  $\Delta T$  is the change in temperature of the supply and return coolant lines. The sum of the chilling power requirements (5.82 kW) was increased by 20% as a safety factor. Additionally, the chiller needed



to have a total dynamic head of at least 100-ft to pump the chilled water into the dome. The chiller chosen was a Schreiber 300-AC with 10.6 kW of chilling power. This chiller satisfied all the chilling power requirements and was donated from the DTRA TEAMS site. The measurements and power chilling calculations are shown in Table 7.

**Table 7. Water Cooling Calculations of FPBS at Agoura Hills, CA with  $K=0.264$  kW/gpm-°C**

FPBS Component	Measured Flow Rate	Supply Temperature	Return Temperature	Chilling Power
Units	gpm	°C	°C	kW
Coldhead Compressor	0.8	30.6	18.6	2.54
Cryopump Compressor	0.5	33.6	19.2	1.77
Trap and RGM-1 Magnets	1.6	22.2	18.6	1.52

## Appendix C. Calculations for the Design of the Positron Propagation Interface

This appendix outlines the details of the calculations used in the design of the positron propagation interface (PPI). The PPI ensures that positrons created by the First Point Scientific, Inc. positron beam system (FPBS) make it to the sample located in the vacuum chamber system for use in the three-dimensional positron annihilation spectroscopy system.

### C.1 Magnetic Field Calculations

The magnetic fields used in designing the PPI are derived from the Biot-Savart Law,

$$\vec{B} = \frac{\mu_0 I}{4\pi} \oint \frac{d\vec{s} \times \hat{\xi}}{\xi^2} \quad (6)$$

where  $\mu_0$  is the permeability of free space,  $I$  is the steady state current in a wire of differential of the arc length,  $d\vec{s}$ , and  $\xi$  is the vector difference from a point in the field to a point on the wire. When considering a current through a circular loop, the corresponding  $\vec{B}$  is rotationally symmetric so only the axial component  $\hat{z}$  defines  $\vec{B}$ .

There are three regions that are modeled in the design of the PPI. The first is an approximation of the magnetic field from the positron beam system, which has an operating magnetic field of approximately 900 gauss. This is modeled by a single current loop. The second region is the solenoid region between the positron beam system and the entrance to the vacuum chamber. The third region is a near-perfect Helmholtz coil pair that surrounds the vacuum chamber and guides the positrons onto the sample. Solving the Biot-Savart law for each region yields the following equations:

$$\begin{aligned}\vec{B}_{loop} &= \frac{\mu_0 I a^2}{2} (z^2 + a^2)^{-\frac{3}{2}} \hat{z} \\ \vec{B}_{solenoid} &= \frac{\mu_0 N I}{2\ell} \left( \frac{z_1}{\sqrt{a^2 + z_1^2}} - \frac{z_2}{\sqrt{a^2 + z_2^2}} \right) \hat{z} \\ \vec{B}_{coilpair} &= \frac{\mu_0 N I a^2}{2} \left\{ \left[ \left( z + \frac{d}{2} \right)^2 + a^2 \right]^{-\frac{3}{2}} + \left[ \left( z - \frac{d}{2} \right)^2 + a^2 \right]^{-\frac{3}{2}} \right\} \hat{z}\end{aligned}$$

where  $z$  is the axial distance from the current loop or coil,  $a$  is the radius of the loop or coil,  $N$  is the number of loops in the solenoid or Helmholtz coil,  $\ell$  is the length of the solenoid coil,  $d$  is the separation distance of the Helmholtz coil pair, and  $z_1$  and  $z_2$  are the axial distance to the edges of the solenoid coil.

Applying these equations to the geometry of the FPBS and vacuum chamber yields the MATLAB<sup>®</sup> code found in Section C.4 below. This code produces a plot of the total magnetic field,  $\vec{B}_{total}$ , which is the sum of the magnetic fields for the APBS, solenoid, and Helmholtz coil pair. A sample plot can be seen in Figure 37.

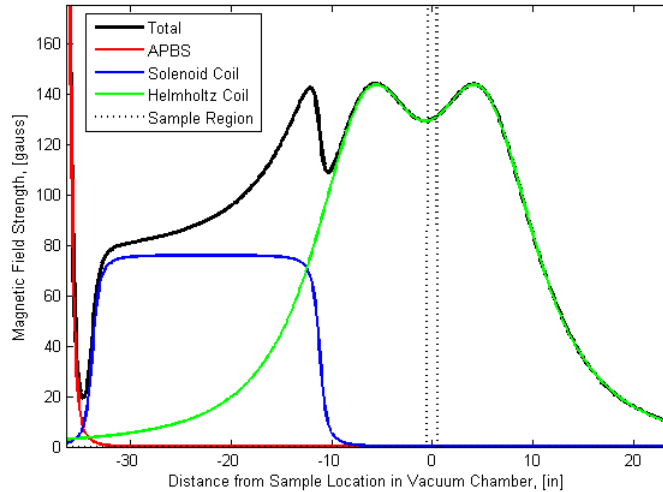


**Figure 37.** Plot of magnetic field calculations for the PPI using a 10 A current in the solenoid coil (173 wounds in 2 layers) and the Helmholtz Coil (390 wounds in each coil).

## C.2 Positron Beam Diameter Calculations

The magnetic field of the PPI determines the positron beam diameter. The relationship can be approximated by

$$d_f = d_i \sqrt{\frac{|\vec{B}_i|}{|\vec{B}_f|}} \quad (7)$$

where  $|\vec{B}_i|$  and  $d_i$  indicate the magnitude of and the beam diameter in the initial magnetic field.  $|\vec{B}_f|$  and  $d_f$  correspond to the same values in the final magnetic field. Given the range of the diameter of the positron beam reported in 2.4.2, the beam diameter at various locations can be calculated using Equation 7 above. This yields Figure 38, which shows the magnitude of the beam diameter at different points along the propagation of the positron beam.

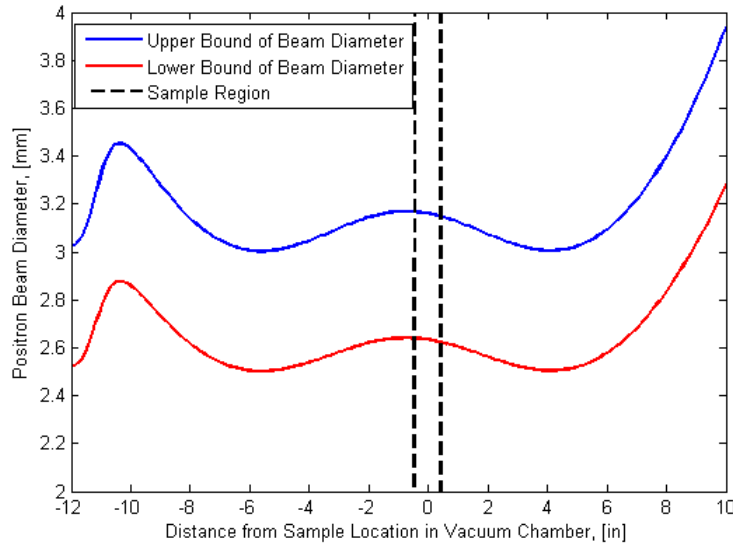


**Figure 38.** Plot of positron beam diameter calculations for the PPI using a 10 A current in the solenoid coil (173 winds in 2 layers) and the Helmholtz Coil (390 winds in each coil).

### C.3 Power Supply Selection

Another consideration in designing the PPI was the amount of power needed to overcome the voltage drop due to the resistance of the Cu wire. The power,  $P$ , was calculated using

$$P = \frac{I^2 L \rho}{A}$$

where  $A$  is the cross sectional area of the wire,  $\rho$  is the resistivity of Cu, and  $L$  is the length of the wire. Given the length of wire used in each coil, the resistance is  $1.7 \Omega$  in each Helmholtz coil and  $0.36 \Omega$  in the solenoid. Since the operating outputs of the power supply is limited to 420 W per channel, equation C.3 is modified to determine the maximum current that can be delivered to the coils, which is 11.1248 A and 20 A for the Helmholtz coil pair and solenoid respectively. The solenoid coil is limited by the maximum current of the power supply.

The final aspect of the design of the electromagnetic coils for the PPI is the dissipation of the heat created by the current flowing through the coils. The exact values are based on the maximum heat that can be dissipated from the coil via air cooling. The primary methods of doing this is via conduction from the coil to the anodized-Al frame and convection to the air.

### C.4 Matlab® Code for Magnetic Field Calculations

This MATLAB® file is used to calculate the magnetic fields that depend on the design the Helmholtz and solenoid coils. The file is also used to estimate the beam diameter at the sample location due to the magnetic fields. The code is able to calculate the number of turns of rectangular Cu in each coil that is possible given

the amount of copper wire that was purchased. Finally, this code estimates the heat dissipation of the Helmholtz coils.

```

1 % Purpose: To Calculate the B-Field of the APBS to the AFRL Vacuum...
    Chamber
%         interface
% Version: 1.0 on 30 Nov 2011 by smj - Build Basic B-Field Calcs
%         : 1.1 on 25 Jan 2012 by smj - Added Plots and Beam ...
    Diameter Calcs
%% Magnetic Field Calculation for APBS to Vacuum System Interface
6 close all;
Tesla2gauss = 10^(-4); % Converts Teslas to gauss
in2m = 2.54/100; % Converts inches to meters
mu0 = 4*pi()*10^(-7); % Permeability of Free Space
SampleLoc = 36.375*in2m;
11 % Sets up distance vector from APBS to some distance past the ...
    vacuum
% chamber
z = 0:0.1:60;
z = z*in2m;
% Helmholtz Coil Pair Settings
16 HCoilOffset = 35.635*in2m; % Linear location of center of coil ...
    pair in m
HCoilr = (16.1875+2)*in2m/2; % Mean Radius of one coil in m
HCoilI = 10; % Current in coil wire in amps
HCoildh = 5.75*in2m*2; % Separation distance of Helmholtz coil ...
    pair
% Does not account for width of coils assumes closest sides
21 HCoilN = 390; % Number of loops in each coil
%Solenoid Coil Settings
SolenoidOffset = 13.9*in2m; % Linear location of center of coil in...
    m
Solenoidr = 1.5/2*in2m; % Mean Radius of coil in m
SolenoidN = 173*2; % Number of loops in each coil
26 Solenoidl = 22.5*in2m; % length of the solenoid coil in m
SolenoidI = 10; % Current in coil wire in amps
% APBS Magnetic Field Estimator (Settings are such that the ...
    magnetic field
% is ~900 gauss).
Beamr = 0.2*in2m;
31 BeamI = 725;

% Calculate B-Fields
BBeam = BFieldLoop(Beamr,z,BeamI,mu0);
BHCoil = BFieldHelmholtzCoil(HCoilr,HCoilI,mu0,HCoilN,HCoildh,z-...
    HCoilOffset);
36 BSolenoid = BFieldSolenoid(Solenoidr,SolenoidI,mu0,SolenoidN,...
    Solenoidl,z-SolenoidOffset);
BSum = BBeam + BHCoil + BSolenoid;

% Plots B-Fields
ind = find(z<(SampleLoc+0.01) & z>(SampleLoc-0.01));

```

```

41 SampleInd = zeros(1,length(z));
   SampleInd(ind) = max(BSum);
   z4plot = (z-SampleLoc)/in2m;
   figure('Color','w');
   plot(z4plot,BSum,'-k','LineWidth',2);
46 hold on;
   plot(z4plot,BBeam,'-r');
   plot(z4plot,BSolenoid,'-b',z4plot,BHCoil,'-g',z4plot,SampleInd,'-r...
       ');
   axis([min(z4plot) max(z4plot) 0 175*Tesla2gauss]);
   xlabel('Distance from Sample Location in Vacuum Chamber, [in]');
51 ylabel('Magnetic Field Strength, [Tesla]');

   figure('Color','w');
   plot(z4plot,BSum/Tesla2gauss,'-k','LineWidth',2);
   hold on;
56 plot(z4plot,BBeam/Tesla2gauss,'-r');
   plot(z4plot,BSolenoid/Tesla2gauss,'-b',z4plot,BHCoil/Tesla2gauss,'...
       -g',z4plot,SampleInd/Tesla2gauss,'-r');
   axis([min(z4plot) max(z4plot) 0 175]);
   xlabel('Distance from Sample Location in Vacuum Chamber, [in]');
   ylabel('Magnetic Field Strength, [gauss]');
61 %% Helmholtz Coils Calculation of Number of Loops

   wCuH = 0.132; % Width of Cu Wire in inches
   hCuH = 0.065; % Height of Cu Wire in inches
   aCoil = 2; % Height & Width of Helmholtz Coil Cross Section in ...
       inches
66 dCoilH = 16.375;
   NperLayer = floor(aCoil/wCuH);
   distCuWireHCoil = 0;
   for n = 1:floor(aCoil/hCuH);
       distCuWireHCoil = distCuWireHCoil + (dCoilH + (n-1)*hCuH)*pi()*...
           *NperLayer/12;
71   if distCuWireHCoil > 1800
       disp(n);
       disp(distCuWireHCoil);
       end
   end
76 %%% so can get up to 26 layers => 390 wounds total/Helmholtz Coil

   %% Solenoid Coil Calculation of Number of Loops Possible
   wCuS = 0.13; % Width of Cu Wire in inches
   hCuS = 0.06; % Height of Cu Wire in inches
81 lCoil = 22.5; % Length of Solenoid Coil
   dCoils = 1.5;
   NperLayer = floor(lCoil/wCuS);
   distCuWireS = 0;
   for n = 1:6;
86   distCuWireS = distCuWireS + (dCoils + (n-1)*hCuS)*pi()*...
       NperLayer/12;
       if distCuWireS > 350

```

```

        disp(n);
        disp(distCuWireS);
    end
91 end
    %%% So Can get up to 4 layers of wounds => 700 wounds total

    %% Beam Diameter Calculation
    BeamDMax(1) = 1.2; % Maximum Starting beam diameter in mm
96 BeamDMin(1) = 1.0; % Minimum Starting beam diameter in mm
    for n = 2:length(BSum)
        BRatio = sqrt(BSum(n-1)/BSum(n));
        BeamDMax(n) = BeamDMax(n-1)*BRatio;
        BeamDMin(n) = BeamDMin(n-1)*BRatio;
101 end
    SampleIndD = SampleInd*max(BeamDMax)*15;
    figure('Color','w');
    plot(z4plot,BeamDMax,'-b',z4plot,BeamDMin,'-r',z4plot,SampleIndD,'...
        -k');
    axis([min(z4plot) max(z4plot) 1 12]);
106 xlabel('Distance from Sample Location in Vacuum Chamber, [in]');
    ylabel('Positron Beam Diameter, [mm]');
    %%% This is a model that estimates the beam diameter.

    %% Power calculations
111 I = 7:0.1:11.5; % Current vector in A
    rho = 1.712 * 10^(-6); % Resistivity of Cu in ohm*cm

    % Solenoid Coil
    AreaS = wCuS*hCuS*2.54^2; % cross sectional area of Solenoid coil ...
        in cm^2
116 LengthS = 350*12*2.54; % max length of used in solenoid coil in cm
    SurfAreaS= lCoil*pi()*dCoilS*2.54^2; % Surface area estimate of ...
        coil in cm^2

    PowerS = (rho*LengthS/AreaS)*I.^2;

121 % Solenoid Coil
    AreaH = wCuH*hCuH*2.54^2; % cross sectional area of one helmholtz ...
        coil in cm^2
    LengthH = 3600*12*2.54; % max length of Cu wire used in both ...
        helmholtz coils in cm
    SurfAreaH = 2*aCoil*pi()*2.54^2*(dCoilH + dCoilH + aCoil) + 4*pi()*...
        *((dCoilH + aCoil)^2 - dCoilH^2);
    % Surface area estimate of both helmholtz coils in cm^2
126 PowerH = (rho*LengthH/AreaH)*I.^2;
    PowerMax = ones(1,length(I))*420;
    figure('Color','w'); plot(I,PowerS,'-b',I,PowerH,'-k',I,PowerMax,'...
        -r');
    axis([min(I) max(I) min(PowerS) max(PowerH)]);
131 xlabel('Current in Coil or Coil Pair, [A]');
    ylabel('Power of Coil or Coil Pair, [W]');

```



```

%% So max power that is achieved for HCoil is when I = 11.1248 A
136 %% Temperature Change in Coils
Tamb = 25; %Room Temperature in degrees Celsius
kCu = 401; %Thermal Conductivity of Cu in [W/m/deg C]
DeltaTH = PowerH./SurfAreaH/hCu + Tamb;
DeltaTS = PowerS./SurfAreaS/hCu + Tamb;
141 figure('Color','w'); plot(I,DeltaTS,'-b',I,DeltaTH,'-k');
axis([min(I) max(I) min(DeltaTS) max(DeltaTH)]);
xlabel('Current in Coil or Coil Pair, [A]');
ylabel('Temperature Change Coil or Coil Pair, [^\circ C]');
146 %% Heat Transfer by Convection and Conduction from the Helmholtz ...
    Coil through the Al Frame to the Air
hAir = 10; %Thermal Conductivity of Cu in [W/m/deg C]
SurfAreaAirH = 2*pi()*aCoil*(dCoilH + aCoil); % Surface area of ...
    the Helmholtz coil that contacts the air
DeltaTAirH = PowerH./SurfAreaH./hAir + Tamb;
151 %% Heat Transfer by Conduction from the Helmholtz Coil to Al frame
kAl = 250; %Thermal Conductivity of Cu in [W/m/deg C]
SurfAreaAlH = SurfAreaH - SurfAreaAirH; % Surface area of the ...
    Helmholtz coil that contacts the Al frame
ThickFrameAlH = 0.25*2.54/100; % thickness of the Al frame in m
156 DeltaTAlH = PowerH./SurfAreaAlH./kAl.*ThickFrameAlH + Tamb;

%% Heat Transfer by Convection from the Solenoid Coil to the Air.
SurfAreaAirS = SurfAreaS;
DeltaTAirS = PowerS./SurfAreaS./hAir + Tamb;
161 figure('Color','w'); plot(I,DeltaTAirS,'-b',I,DeltaTAirH,'-k', I, ...
    DeltaTAlH, '-r');
axis([min(I) max(I) min(DeltaTAlS) max(DeltaTAirH)]);
xlabel('Current in Coil or Coil Pair, [A]');
ylabel('Temperature Change due to Power from Coil or Coil Pair, ...
    [^\circ C]');

```

```

1 function B = BFieldLoop(r,z,I,mu0)
% Purpose: This code calculates the B-field due to a current, I, ...
    through a
% loop of radius, r, at a point along the z-axis, z, away from the...
    origin,
% which is at the center of the loop.
6 B = mu0*I/2*r^2*(z.^2+r^2).^(-3/2);
end

```

```

function B = BFieldSolenoid(r,I,mu0,N,l,z)
% Purpose: This code calculates the B-field due to a current, I, ...
    through a

```

```

3 % pair of solenoid coil of radius, r; number of turns, N,; and ...
  length, l,
  % at a point along the z-axis, z, away from the origin, which is ...
  at the
  % center of the loop.

mu1= (z+l/2)./(((z+l/2).^2+r^2).^(1/2));
8 mu2= (z-l/2)./(((z-l/2).^2+r^2).^(1/2));
  B = mu0*I/2*N/l*(mu1-mu2);

end

```

```

function B = BFieldHelmholtzCoil(r,I,mu0,N,dh,z)
% Purpose: This code calculates the B-field due to a current, I, ...
  through a
  % pair of Helmholtz coils of radius, r; number of turns, N,; and ...
  separation
4 % distance, dh, at a point along the z-axis, z, away from the ...
  origin,
  % which is at the center of the loop.

B = mu0*I/2*N*r^2*(((z+dh/2).^2+r^2).^(-3/2)+((z-dh/2).^2+r^2)...
  .^(-3/2));
9 end

```

## Appendix D. Procedure for Creating the Copper Standard Source

The procedure that was approved and executed for creating the CuSS begins on the  
next page.

# $^{22}\text{Na}$ Deposition onto Copper Samples Radiation Test Plan

(13 January 2012)

Capt. Stephen M Jiménez

*Air Force Institute of Technology, Wright-Patterson AFB, OH 45431*

## I. INTRODUCTION

This document discusses in details the steps and procedures required to complete  $\text{Na}^{22}$  deposition into capillary tubing. This document also addresses the deposition of  $\text{Na}^{22}$  sandwiched between two 10 mm x 10 mm x 0.5 mm copper samples as well as inside aqueous dodecaborate solutions. All radioactive handling of materials will be conducted within the radiation hood located in the chemical lab in building 470 at Wright Patterson AFB OH. The  $^{22}\text{Na}$  source (T-127) will be deposited from a glass 5 mL vile with a NaCl mixture of 44.3 uCi (17 Apr 2008) initial activity. Current activity of T-127 is 23.3 uCi. The vile contains ~2.2 mL after the creation of diluted samples, which were designated T-127A through K.

The entire solution of the radioactive NaCl will also be placed on two copper samples. The samples will be heated to  $\sim 80^\circ\text{C}$ . Following heat period, the copper samples will be placed on top of the other to form a sandwich configuration. Double sided tape and aluminum foil will secure the sample and in particular ensure no radioactive leakage. Through entire process a Geiger counter (or other form of a radioactive counter) will be used to monitor activity. All radioactive waste will be disposed of properly and all functional radioactive materials will be properly labeled for future safety and verification.

## II. TEST OBJECTIVES

The objectives for this test are to safely deposit approximately 16 uCi of  $\text{Na}^{22}$  onto 2 samples, inside a capillary tube and sandwiched in between two copper samples.

- 1) Copper Samples Radioactive Deposition
  - a. Perform outlined objectives without radioactivity to confirm methodology
  - b. Drip 1.5 mL (15.9 uCi) onto two 10 mm x 10 mm x 0.5 mm near identical copper samples
  - c. Heat sample at  $80^\circ\text{C}$  to evaporate water
  - d. Place copper samples on top of each other (sandwich configuration) and secure with tape
  - e. Scan room for activity to distinguish between radioactive contamination and nonradioactive laboratory waste.
- 2) Dispose of all radioactive and nonradioactive waste appropriately. Properly label functional radioactive material for safety and future verification.

## III. PROPOSED SCHEDULE

All test objectives will be completed 17 January 2012.

#### IV. TEST PRIORITY

If time permits, all outlined tests will be conducted. Due to possible unforeseen equipment failures and scheduling issues the priority of measurements is exactly as numbered in the test objectives section of this test plan, excluding Objective 4 radioactive disposal, which must be accomplished. Timeline may be extended if necessary.

#### V. TEST SETUP

In order to perform described measurement the following equipment will be required.

- 1)  $^{22}\text{Na}$  T-127 44.3 uCi (17 Apr 2008)
- 2) Two 10 mm x 10 mm x 0.5 mm copper samples
- 3) Single Sided Tape
- 4) Multiple 22 Gauge Syringes
- 5) Lead Bricks
- 6) 1 Hot Plate. Make sure to cover hot plates with aluminum foil in order to further separate hot plates from radioactive material. Do not make Al foil disruptive to handling material on top as well as temperature knobs in front.
- 7) Labeled Radioactive Waste Container
- 8) Transfer Tools: Syringes, scissors
- 9) Gloves, Laboratory Coats, and Goggles
- 10) Radiation Detector
- 11) Radioactive waste container (plastic bag with the opening rolled over the edge of its support container)
- 12) Transfer tools to include tweezers and syringes

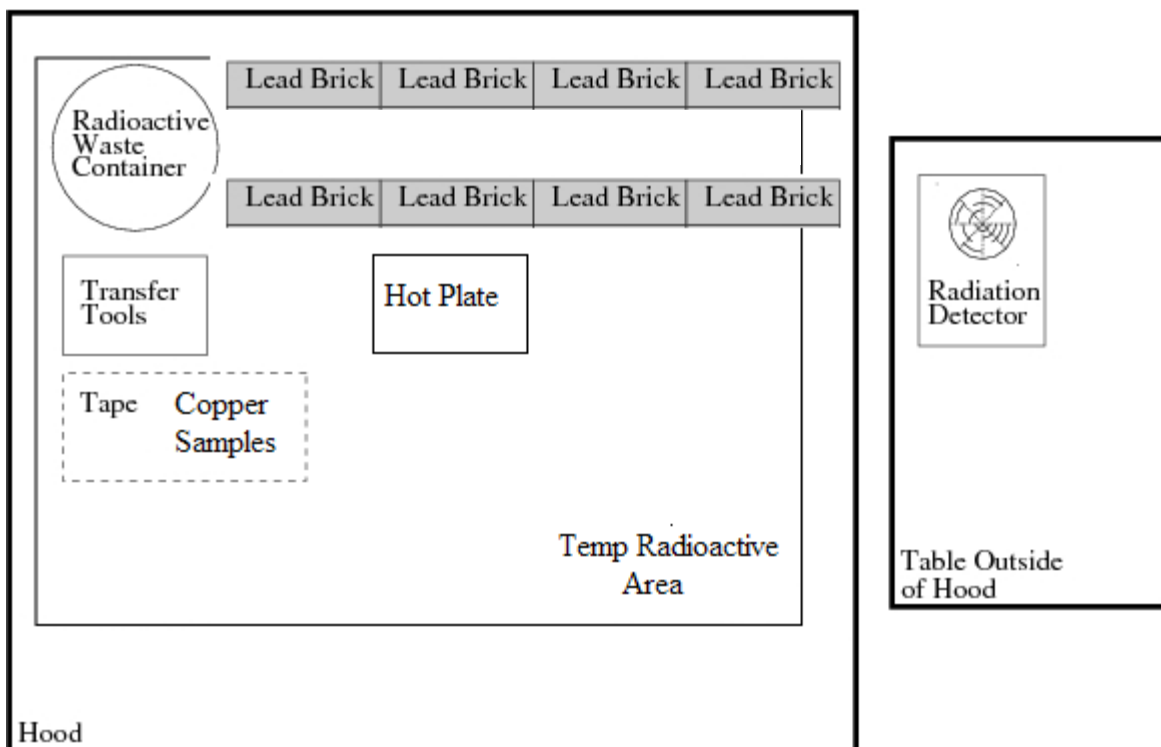


Figure 1. Diagram of Setup

## VI. TEST PROCEDURES

- 1) Copper Samples with radioactive  $^{22}\text{Na}$  will be made by dripping radioactive solution onto a two 10 mm x 10 mm x 0.5 mm copper sample placed on top Aluminum foil wrapped around a hot plate. Following evaporation, samples will be placed on single sided tap and then sandwiched together. Detailed procedures are:
  - a. Perform outlined objectives without radioactivity to confirm methodology. Make any changes to the procedure based on dry runs prior to continuing.
  - b. Bring out two 10 mm x 10 mm x 0.5 mm copper sample and place on top of left most hot plate covered in aluminum foil.
  - c. Bring out T-127  $^{22}\text{Na}$  source (5.0g) vial 44.3 uCi 17 Apr 2008 from in between the lead bricks at the far end of the hood and gently remove cap.
  - d. Insert syringe into  $^{22}\text{Na}$  source and draw 0.3-0.5 mL of solution.
  - e. Gently drip solution on top of 10 mm x 10 mm x 0.5 mm copper samples, which are on the hot plate heated to 80 °C.
  - f. Allow drops to evaporate, on the order of 1 - 2 minutes

- g. Repeat e - f until all the liquid is gone from the syringe and the entire solution is gone.
  - h. Place syringe onto temporary radioactive area and put  $^{22}\text{Na}$  source back in between lead bricks.
  - i. Cool samples, and place on single-sided tape.
  - j. Place copper sample together in a sandwich configuration and secure with tape additional tap.
  - k. Cut edges and affirm with swipes no radioactive materials are present. If radioactivity is present, dispose of in the radioactive waste container.
  - l. Scan room for activity to distinguish between radioactive contamination and nonradioactive laboratory waste.
- 2) Dispose of all radioactive and nonradioactive waste appropriately. Properly label functional radioactive material for safety and future verification.

## VII. SPECIAL REQUIREMENTS

When dealing with radioactive materials, care must be taken to limit exposure. Before handling any radioactivity make sure to follow ALARA (As Low As Reasonably Achievable) procedures. For experimentation 2 pair of gloves and coat are required to prevent exposure to skin. Laboratory goggles are also required to prevent exposure to the eyes. All radioactive handling require at least two people to be present in order to provide additional resources to ensure safety. In case of glove contamination, remove one pair of gloves using single finger and dispose of contaminated glove in the radioactive waste bag.

## VIII. POINTS OF CONTACT

The following people can be contacted should any questions arise.

Capt. Stephen M. Jiménez, E-Mail: [Stephen.Jimenez@afit.edu](mailto:Stephen.Jimenez@afit.edu)

Dr. Larry Burggraf, E-Mail: [Larry.Burggraf@afit.edu](mailto:Larry.Burggraf@afit.edu)

## Appendix E. Utilities required for RGM-1 and APBS

The list of manufacture specified utilities that are required for the operation of the FPBS and components begins on the next page.



### 1. Water cooling, assuming 22°C water:

DEVICE	FLOW	PRESSURE	FITTING
Coldhead compressor	0.75 gpm	30 psi	1/2" Swagelok
Cryopump compressor	0.75 gpm	30 psi	3/8" Swagelok
Trap magnet	1 gpm	60 psi	3/8" Swagelok
RMG-1 magnets	0.75gpm	30 psi	3/8" Swagelok

The best option would be a 60 psi recirculator or house chilled (if it is clean) with separate valves and flow meters so you can set the flow for each device. On my system I only have 30 psi so I cannot run the main magnet continuously at full power. Having water that is slightly cooler than room temperature, say 18°C, is of benefit, but if it is cold enough to cause condensation when the magnets are not running, it will cause problems. Also there can be problems in restarting the compressors if they are too cold, so if you are running chilled water, you need to remember to shut off the water when you switch off the compressors. (Some compressors are supplied with automatic shutoff valves, but these units are not.)

The manufacturer of the compressors recommends "typical municipal quality drinking water, pH of 6 to 8 and total hardness < 85 ppm".

### 2. Electrical power (all 60Hz, single phase)

Device	Current	VAC	Connector
Trap magnet power supply	20 A	208	NEMA L6-20 (turnlock)
Beam tube power supply	10A	110	NEMA 5-15
Coldhead compressor	16.5A	208	NEMA L6-20 (turnlock)
Cryopump compressor	15 A	208	NEMA L6-20 (turnlock)
Instruments	10A	110	NEMA 5-15 x 2

### 3. Compressed Air

70 psi for cycling pneumatic valves, intermittent operation.

### 4. Nitrogen

High purity nitrogen for venting the system, occasional use, bottled gas recommended.

## Appendix F. Data Parsing Code

The parsing and analysis code was written in two languages: Bash script and MATLAB<sup>®</sup>. The Bash script, written by Tony Kelly, took advantage of the raw data format from the PHDs Imager software. The Bash parsing script only saved events that were recorded within the coincidence window for two or four sites. Two sites were looked at for efficiency data parsing, whereas four sites were for positron annihilation data parsing. The MATLAB<sup>®</sup> parsing script would then sort through the Bash output four lines at a time and further parse the data to only include full site events that occurred at the energy on interest and had two site events in each detector. The MATLAB<sup>®</sup> parsing code analyzed the raw data to provide a matrix of the locations and energies of coincident events.

### F.1 Bash Script

```
1 #!/bin/bash
#
# RemoveBackground.sh
#
6 #
# Created by Tony Kelly on 12/9/11.
# Copyright 2011 __MyCompanyName__. All rights reserved.
#
#
11 clear
#
# echo Hello, I am the RemoveBackground Script
16 # echo I am now removing the background events.
# echo ... One moment please ...
# echo
#
# sed -n '/^[1-9].4/p' ${1}.phd > ${1}_4.phd
21 #sed -n '/^[1-9].4.[1-9].[1-9][1-9].[481-541]/p' ...
# Cu_15min_120611_4.phd > Cu_15min_120611_4_E.phd
#
# echo Done!
```

## F.2 Matlab® Parsing Code

```
%%% File Parse for PHDs Spec72 Energy Event Window Raw Files in a
2 %%% Single Folder
%%% Created on 13 Dec 2011 by smj
%%% Based on PMSEAnalysis.m created by Capt Stephen M. Jimenez

function Spec72Parser_MultiRawEventFiles(Material, Energy, deltaE,...
    CaseInd, NumSubs)
7 % % User Inputs
% Material - prefix of the file names desired to be analyzed to
%             include the underscore
%             - e.g.'CuSS_' for Copper Standard Source
% EwinCent - Center of Energy Window (keV) desired
12 % deltaE - +/- of Center of Energy Window (keV)
% CaseInd - suffix of the filed names desired to be analyzed
%             - 2 for 2-strip events or 4 for 4-strip events
% NumSubs - number of subpixel to interpolate the data

17 % Determines file extension to look for depending on whether user
% wants to look at two or four site events.
exten = ['_' num2str(CaseInd) '.phd'];
if CaseInd == 2
    ncol = 4;
22 elseif CaseInd ==4
    ncol = 7;
end

folder = uigetdir('/Users/jimenez/Desktop/CuData');
27 s = dir(folder);
temp = struct2cell(s);
ind = find(strncmp(Material,temp,length(Material)));
temp = temp(ind);

32 % Displays all the *.extn files that are found in the folder
% specified
count = 1;
filenames = [];
disp(['Starting analysis of the following files in ' folder ':']);
37 for i=1:length(temp)
    fname = temp(i);
    fname = cell2mat(fname);
    if strcmp(fname(end-5:end),exten)
        filenames{count} = fname;
42         disp(fname);
        count = count +1;
    end
end
innnput = input('Are these the files you wish to analyze?');
47 % Initilizes final data matrices
Data = zeros(1000,ncol);
```

```

writecount = 1;
DataRow = zeros(1,7);
52 % Goes thru each file, parses it, and combines data into two
% matrices
for i = 1:length(filenamees)
    tempfName = cell2mat(filenamees(i));
57 [tempData, tempDataRow, time1(i)] = Spec72Parser_RawEventv4([...
    folder '/' tempfName],Energy,deltaE,NumSubs);
    blocksize = writecount+size(tempData,1)-1;
    Data(writecount:blocksize,:) = tempData;
    DataRow = [DataRow; tempDataRow];
    disp(['Time to run ' tempfName ' was ' num2str(time1(i)) '.'])...
    ;
62 writecount = blocksize+1;
end

% Saves Subpixel and Raw Data for all the files in two matrices
ParseInfo = [filenamees ' num2cell(time1)']
67 SaveNameRaw = [folder '/' Material 'Raw_Data_Parsed_on_' date '....
    mat'];
SaveName = [folder '/' Material 'Subpixel_Data_Parsed_on_' date '....
    mat'];
indices = find(Data);
Data = Data(indices);
Data = reshape(Data,size(Data,1)/ncol,ncol);
72 save(SaveName,'Data');
save(SaveNameRaw,'DataRow');

end

```

```

%%% File Parser for PHDs Spec72 Energy Event Window Raw File
%%% Created on 1 Dec 2011 by smj
%%% Modifications:
%%% - 3 Feb 2012 by smj: Added NumSubStrips input not hardcoded
5 %%% -
%%% Based on PHDs_EventWindowed_Reader.m created by 2nd Lt
%%% FitzGerald

function [SiteMat, SiteMatRaw, ttt]=Spec72Parser_RawEventv4(...
    filename, EwinCent, deltaE, NumSubStrips)
10 % % User Inputs
% filename - Takes *.phd raw event file from Imager72 Software
%           Format is [Event #, Event Count, Time, Slow Energy,
%           Fast Predecessor, Fast Successor]
% EwinCent - Center of Energy Window (keV) desired
15 % deltaE - +/- of Center of Energy Window (keV)
% NumSubStrips - number of subpixel to interpolate the data

% % Outputs
% SiteMat - matrix of parsed energy and subpixel locations
20 % SiteMatRaw - matrix raw but parsed data

```

```

% ttt          - time to read the entire file

% Calculates File Size
s = dir(filename);
25 filesize = s.bytes;
numlines = ceil(filesize / 28.2);

% Determines Energy Window Boundaries
E_low = EwinCent-deltaE;
30 E_high = EwinCent+deltaE;

% Skips Header
fid = fopen(filename);

35 % Initialize Data Arrays
CaseInd = str2num(filename(end-4)); % Determines which part of
% switch statement that the File will look at.
if CaseInd==2
    OneSiteData=zeros(numlines,4);
40 OneSiteData=zeros(1,4);
elseif CaseInd==4
    TwoSiteData=zeros(numlines,7);
    TwoSiteDataRaw = zeros(1,7);
else
45 disp('NOT A VALID FILE NAME!');
    disp('Run bash3 script named RemoveBackground.sh before ...
        analyzing data.');
```

```

end

linecount = 1;
50 writecount = 1;
writecountr = 1;

tic
%Loop through file. Look at each line (event) individually
55 while feof(fid) == 0

    %Make an array of 7 numbers from the given line
    % & Grab all events associated with first event.

60 line_num = RawEventRead(fid);
    for i = 2:CaseInd;
        line_num(i,:) = RawEventRead(fid);
    end

65 %Check to see if within the given energy range
    if ((line_num(:,5) >= E_low) & (line_num(:,5) <= E_high))

        switch CaseInd
70 case 2 % The case for one-site events
            tBase = max(line_num(:,3));

```

```

%           if (tBase<=10 && line_num(1,3)~=line_num(2,3));
%           % doesn't look at events outside
%           % of 200 ns (10 * time base which is 20 ns).
75           OneSiteDataRow(writecountr:writecountr+1,:)=...
                line_num;
                [Event2] = DPosCalc(NumSubStrips,line_num(:,4)...
                    ,line_num(:,5),line_num(:,6:7));
                if ((Event2(3) >= E_low) && (Event2(3) <= ...
                    E_high))
                    OneSiteData(writecount,:) = [Event2 tBase...
                        ];
                    writecount = writecount + 1;
80           end
                writecountr = writecountr+2;
            end
%           case 4 % The case for two strip charge sharing event
%           % or a one-siteevent in each detector.
85           tBase = max(line_num(:,3));
%           if (tBase<=10 && line_num(1,3)~=line_num(4,3));
%           % doesn't look at events outside
%           % of 200ns (10 * time base which is 20 ns).
%           TwoSiteDataRow(writecountr:writecountr+3,:)=...
                line_num;
90           [Event4] = DPosEng4Calc(NumSubStrips,line_num...
                (:,4),line_num(:,5),line_num(:,6:7));
                if (Event4(3)>=E_low && Event4(3)<=E_high && ...
                    Event4(6)>=E_low && Event4(6)<=E_high)
                    TwoSiteData(writecount,:) = [Event4 tBase...
                        ];
                    writecount = writecount + 1;
95           end
                writecountr = writecountr + 4;
            end
%           otherwise
100        end

        end

        linecount = linecount + line_num(1,2);
        if mod(linecount,10000)==1
105            percent = linecount/numlines*100;
            fprintf('%f percent complete\n',percent);
        end
    end
110 ttt = toc;
    fclose(fid);
    if CaseInd==2
        indices = find(OneSiteData);
        SiteMat = OneSiteData(indices);
115        SiteMatRaw = OneSiteDataRow(2:end,:);

```

```

        ncol = 4;
        extenstr = '_1Site.mat';
elseif CaseInd == 4
120     indices = find(TwoSiteData);
        SiteMat = TwoSiteData(indices);
        SiteMatRaw = TwoSiteDataRow(2:end,:);
        ncol=7;
        extenstr = '_2Site.mat';
else
125     disp('NOT A VALID FILE NAME!');
        disp('How you got here is beyond me!');
end
if isempty(SiteMat)==0
130 SiteMat = reshape(SiteMat, size(SiteMat,1)/ncol,ncol);
end
end

```

```

2  %%% Read Function for the PHDs Spec72 Raw Event File
   %%% Created on 12 Dec 2011 by smj
function [ line_num ] = RawEventRead( fid )
% % User inputs
% fid - file ID number of a file opened in
%       Spec72Parser_RawEventv4.m
7  % % Outputs
% line_num - N by 7 matrix that corresponds to the lines read in
%            from the file associated with the fid, where N is
%            the number of lines that are associated with the
%            same event.
12  line = fgets(fid);
    line_str = textscan(line, '%s %s %s %s %s %s %s');
    for i = 1:numel(line_str)
        line_num(i) = str2double(line_str{i});
    end
17 end

```

```

2  %%% Raw Event Parser for PHDs Spec72 Energy Event Window Raw File
   %%% Created on 14 Dec 2011 by smj
   %%% This file parses out 2-channel events and interpolates the
   %%% subpixel position values from the edge of the current strip.

function [Event] = DPosCalc(NumSubStrips,ChanNum,Energy,FOMMat)
7  % % User Inputs
% NumSubStrips - number of subpixel to interpolate the data
% ChanNum - 1 by n matrix of the channel/strip numbers
% Energy - 1 by n matrix of event energy values
% FOMMat - 2 by n column matrix of FOM predecessor and successor
12 % % Outputs
% Event - 1 by 6 matrix of subpixel position and energy values
%         (X position first, then Y position, then energy) for
%         each detector (Detector0 first, then Detector1)

```

```

17 XInd = find((ChanNum>=0 & ChanNum<=15)|(ChanNum>=32 & ChanNum<=47)...
    ); % AC Channels
YInd = find((ChanNum>=16 & ChanNum<=31)|(ChanNum>=48 & ChanNum...
    <=63)); % DC Channels
if FOMMat(YInd,2)==0
    FOMMat(YInd,2)=0.0001;
22 end
if FOMMat(XInd,2)==0
    FOMMat(XInd,2)=0.0001;
end
YPos = ceil(NumSubStrips*(ChanNum(YInd) + (FOMMat(YInd,2)./(FOMMat...
    (YInd,2)+FOMMat(YInd,1)))));
27 XPos = ceil(NumSubStrips*(ChanNum(XInd) + (FOMMat(XInd,2)./(FOMMat...
    (XInd,2)+FOMMat(XInd,1)))));

EngAvg = mean(Energy);
if (isempty(YPos)==0 && isempty(XPos)==0)
    Event = [XPos YPos EngAvg];
32 else
    Event = zeros(1,3);
end
end

```

```

%%% Raw Event Parser for PHDs Spec72 Energy Event Window Raw File
%%% Created on 14 Dec 2011 by smj
%%% This file parses out 4-channel events to make sure they occur
4 %%% in different detectors and interpolates the subpixel position
%%% values from the edge of the current strip.

function [Event] = DPosEng4Calc(NumSubStrips,ChanNum,Energy,FOMMat...
    )
% % User Inputs
9 % NumSubStrips - number of subpixel to interpolate the data
% ChanNum - 1 by n matrix of the channel/strip numbers
% Energy - 1 by n matrix of event energy values
% FOMMat - 2 by n column matrix of FOM predecessor and successor

14 % % Outputs
% Event - 1 by 6 matrix of subpixel position and energy values
%         (X position first, then Y position, then energy) for
%         each detector (Detector0 first, then Detector1)

19 XInd0 = find((ChanNum>=0 & ChanNum<=15)); % Detector0 AC Chans
XInd1 = find((ChanNum>=32 & ChanNum<=47)); % Detector1 AC Chans
YInd0 = find((ChanNum>=16 & ChanNum<=31)); % Detector0 DC Chans
YInd1 = find((ChanNum>=48 & ChanNum<=63)); % Detector1 DC Chans
if (isempty(YInd0)==0 && isempty(XInd0)==0 && isempty(YInd1)==0 &&...
    isempty(XInd1)==0)
24     if FOMMat(YInd0,2)==0
        FOMMat(YInd0,2)=0.001;
    end
end

```



```

end
if FOMMat(YInd1,2)==0
    FOMMat(YInd1,2)=0.001;
29 end
if FOMMat(XInd0,2)==0
    FOMMat(XInd0,2)=0.001;
end
34 if FOMMat(XInd1,2)==0
    FOMMat(XInd1,2)=0.001;
end
YPos0 = ceil(NumSubStrips*(ChanNum(YInd0) + (FOMMat(YInd0,2)...
    ./(FOMMat(YInd0,2)+FOMMat(YInd0,1)))));
XPos0 = ceil(NumSubStrips*(ChanNum(XInd0) + (FOMMat(XInd0,2)...
    ./(FOMMat(XInd0,2)+FOMMat(XInd0,1)))));
YPos1 = ceil(NumSubStrips*(ChanNum(YInd1) + (FOMMat(YInd1,2)...
    ./(FOMMat(YInd1,2)+FOMMat(YInd1,1)))));
39 XPos1 = ceil(NumSubStrips*(ChanNum(XInd1) + (FOMMat(XInd1,2)...
    ./(FOMMat(XInd1,2)+FOMMat(XInd1,1)))));

Eng0 = (Energy(YInd0) + Energy(XInd0))/2;
Eng1 = (Energy(YInd1) + Energy(XInd1))/2;
if (isempty(YPos0)==0 && isempty(XPos0)==0 && isempty(YPos1)...
    ==0 && isempty(XPos1)==0)
44     Event = [XPos0 YPos0 Eng0 XPos1 YPos1 Eng1];
end
else
    Event = zeros(1,6);
end
49 end

```

## Appendix G. Subpixel Efficiency Correction Code

This appendix shows the MATLAB® code for the detector subpixel efficiency calculations. The efficiency calculations are used to correct the spectrum for inefficiencies in the subpixel interpolation of the strip detectors.

```
%%% Simultaneous 2D-ACAR and CDBAR Experiment Data Analysis tool
%%% for 3DPASS using AFRL Vacuum Chamber and two PHDs high purity
%%% germanium (HPGe) 16x16 double sided strip detectors (DSSDs).
%%% Created on 12 Dec 2011 by smj
5 %%% Based on Williams Dissertation Section 4.9 Simultaneous 2D-
%%% ACAR and CDBAR Experiment

%%% Creates the average relative efficiency matrices for each
%%% detector to be used in the ThreeDPASSCalc3.m
10 %%% Created on 26 Jan 2012 by smj

function ThreeDPASSEfficiencyCalc(Data, EwinCent, deltaE, timevar,...
    subspixel, plotind)
% % User Inputs
% Data - Parsed file output from Spec72 Parser files
15 % EwinCent - Center of Energy Window (keV) desired
% deltaE - +/- of Center of Energy Window (keV)
% timevar - number of 20ns time intervals to limit data.
% subspixel - how many subpixels to use in the program
% plotind - logical if plots are desired to be seen.
20
% Defines number of number of subpixels
NumSubStrips = subspixel*16;
stripwidth = 4.75; % PHDs DSSD strip width in mm
gapwidth = 0.25; % PHDs DSSD gap width in mm
25
% Filter data to include only specific energies
ind = find(Data(:,3)>=(EwinCent-deltaE) & Data(:,3)<=(EwinCent+...
    deltaE));
Data = Data(ind,:);

30 % Filter data to include only time differences
indt=find(Data(:,4)<=timevar);
Data = Data(indt,:);

% Filter Data into separate matrices for each detector
35 ind0 = find(Data(:,1)<=NumSubStrips*2);
ind1 = find(Data(:,1)>NumSubStrips*2);
Det0 = Data(ind0,:);
Det1 = Data(ind1,:);
Det0(:,2) = Det0(:,2)-NumSubStrips;
40 Det1(:,1) = Det1(:,1)-NumSubStrips*2;
Det1(:,2) = Det1(:,2)-NumSubStrips*3;
```

```

% Filter outermost strips from data because they do not have a
% physical momentum
45 ind00 = find(Det0(:,1)<76 & Det0(:,1)>5);
   Det0=Det0(ind00,:);
   ind00 = find(Det0(:,2)<76 & Det0(:,2)>5);
   Det0=Det0(ind00,:);
   ind11 = find(Det1(:,1)<76 & Det1(:,1)>5);
50 Det1=Det1(ind11,:);
   ind11 = find(Det1(:,2)<76 & Det1(:,2)>5);
   Det1=Det1(ind11,:);

% Creates Distance Vector of the center of each subpixel based on
% the total number of subpixels for a single face of the detector
55 [ThetaRefX] = SubPixelCenters(subsperpixel,stripwidth,gapwidth,...
   NumSubStrips,0);
   [ThetaRefY] = SubPixelCenters(subsperpixel,stripwidth,gapwidth,...
   NumSubStrips,0);

% Creates Distance Vector that defines the edges of the subpixels
60 % to be used for the histogram plots
   [DetectDistRef] = SubPixelEdges(subsperpixel,stripwidth,gapwidth,...
   NumSubStrips);
   DetectDistRef = DetectDistRef(subsperpixel+2:end-(subsperpixel+1))...
   ;
   UsableDetectDist = cell(1,2);
   UsableDetectDist{1} = DetectDistRef;
65 UsableDetectDist{2} = DetectDistRef;

% % Detector 0
   Det0(:,1) = ThetaRefX(Det0(:,1));
   Det0(:,2) = ThetaRefY(Det0(:,2));
70 % % Detector 1
   Det1(:,1) = ThetaRefX(Det1(:,1));
   Det1(:,2) = ThetaRefY(Det1(:,2));

75 % Creates a histogram of the number of counts in each subpixel of
% each detector.
   Det0Res = hist3(Det0(:,1:2),'Edges',UsableDetectDist);
   Det1Res = hist3(Det1(:,1:2),'Edges',UsableDetectDist);

80 % Creates a mask of 1's and 0's that determines what pixels to use
% from the detector response histograms
   mask = PHDsMask(size(Det0Res), subsperpixel);

% Masks the subpixels that are not desired from the detector
85 % response histograms.
   Det0Res = Det0Res.*mask;
   Det1Res = Det1Res.*mask;

% Saves the masked detector response histogram and the mask file
90 % to be used by ThreeDPASSCalc3.m

```

```

save([pwd '/Detector0EfficiencyCounts.mat'], 'Det0Res');
save([pwd '/Detector1EfficiencyCounts.mat'], 'Det1Res');
save([pwd '/DetectorMask_' num2str(subsperpixel) '.mat'], 'mask');

95 Det0Res = EffNormCalc(Det0Res, subsperpixel);
   Det1Res = EffNormCalc(Det1Res, subsperpixel);

save([pwd '/Detector0NormalizedEfficiency.mat'], 'Det0Res');
100 save([pwd '/Detector1NormalizedEfficiency.mat'], 'Det1Res');

if plotind
   figure('Color','w','OuterPosition',[12 660 1400 560]);
   subplot(1,2,1); pcolor(DetectDistRef, DetectDistRef, Det0Res);
105 %title('Detector0 - Response');
   shading flat; xlabel('Vertical Axis [mm]'); ylabel('Beam Axis ...
       [mm]');
   colorbar; axis square;
   caxis([0 1]);
   colormap hot;
110
   subplot(1,2,2); pcolor(DetectDistRef, DetectDistRef, Det1Res);
   %title('Detector1 - Response');
   shading flat; xlabel('Vertical Axis [mm]'); ylabel('Beam Axis ...
       [mm]');
   colorbar; axis square;
115 caxis([0 1]);

   figure('Color','w','OuterPosition',[12 100 1400 560]);
   subplot(1,2,1); pcolor(DetectDistRef, DetectDistRef, Det0Res);
120 %title('Detector0 - Response');
   shading flat; xlabel('Vertical Axis [mm]'); ylabel('Beam Axis ...
       [mm]');
   colorbar; axis square;
   caxis([0 1]);
   colormap jet;

125 subplot(1,2,2); pcolor(DetectDistRef, DetectDistRef, Det1Res);
   %title('Detector1 - Response');
   shading flat; xlabel('Vertical Axis [mm]'); ylabel('Beam Axis ...
       [mm]');
   colorbar; axis square;
   caxis([0 1]);
130 end

end

```

```

%%% Creates Mask for a single detector response based on the
%%% number of substrips for the interpolation. To be used in
3 %%% ThreeDPASSEfficiencyCalc.m
%%% Created on 3 Feb 2012 by smj

```

```

function mask = PHDsMask(sizeM, subsperpixel)
% % User Inputs
8 % sizeM - 2 element matrix that tells the size of the matrix to be
%     masked
% subsperpixel - how many subpixels to use in the program

% % Outputs
13 % mask - matrix of sizeM with zeros and ones defining the good
%     parts of the detector to use

NumSubStrips = subsperpixel*16;
mask = ones(sizeM);
18 lside = 1:subsperpixel*3+3;
    wside = 1:subsperpixel+1;
    aside = subsperpixel:subsperpixel*2+2;

%% Remove Top-L Corner
23 mask(lside,wside) = 0;
    mask(aside,aside) = 0;
    mask(wside,lside) = 0;
%% Remove Top-R Corner
28 mask(lside,end+1-wside) = 0;
    mask(aside,end+1-aside) = 0;
    mask(wside,end+1-lside) = 0;
    msl = 1;
%% Remove Bottom-L Corner
33 mask(end+1-lside,wside) = 0;
    mask(end+1-aside,aside) = 0;
    mask(end+1-wside,lside) = 0;
%% Remove Bottom-R Corner
38 mask(end+1-lside,end+1-wside) = 0;
    mask(end+1-aside,end+1-aside) = 0;
    mask(end+1-wside,end+1-lside) = 0;
end

```

## Appendix H. ACAR/DBAR Analysis Code

The ACAR/DBAR analysis code was written in MATLAB®. The analysis code takes the output from the parsing code to plot the momentum data from 2D-ACAR and CDBAR measurements.

```
1  %%% Simultaneous 2D-ACAR and CDBAR Experiment Data Analysis tool
   %%% for 3DPASS using AFRL Vacuum Chamber and two PHDs high purity
   %%% germanium (HPGe) 16x16 double sided strip detectors (DSSDs)
   %%% that also corrects for subpixel efficiencies using average
   %%% relative efficiency matrices that come from
6  %%% ThreeDPASSEfficiencyCalc.m
   %%% Created on 12 Dec 2011 by smj

   %%% Based on Williams Dissertation Section 4.9 Simultaneous 2D-
   %%% ACAR and CDBAR Experiment
11 function ThreeDPASSCalc3(Data, EwinCent, deltaE, timemax, ...
    DetectSourceDist, subperpixel)
    % % User Inputs
    % Data - Parsed file output from Spec72 Parser files
    % EwinCent - Center of Energy Window (keV) desired
16 % deltaE - +/- of Center of Energy Window (keV)
    % timevar - number of 20ns time intervals to limit data.
    % DetectSourceDist - distance to each detector in m
    % subperpixel - how many subpixels to use in the program

21 %%% 2D-ACAR Calculation

    NumSubStrips = subperpixel*16;
    stripwidth = 4.75; % PHDs DSSD strip width in mm
    gapwidth = 0.25; % PHDs DSSD gap width in mm
26 % Filter data to include only specific energies
    ind = find(Data(:,3)>=(EwinCent-deltaE) & Data(:,3)<=(EwinCent+...
        deltaE));
    Data = Data(ind,:);

31 % Filter data to include only time differences
    indt=find(Data(:,7)<=timemax);
    Data = Data(indt,:);

    % Filter outermost strips from data because they do not have a
36 % physical momentum
    ind = find(Data(:,1)~=subperpixel & Data(:,2)~=NumSubStrips+...
        subperpixel & Data(:,4)~=NumSubStrips*2+subperpixel & Data...
        (:,5)~=NumSubStrips*3+subperpixel & Data(:,1)~=NumSubStrips-...
        subperpixel+1 & Data(:,2)~=NumSubStrips*2-subperpixel+1 & ...
        Data(:,4)~=NumSubStrips*3-subperpixel+1 & Data(:,5)~=...
        NumSubStrips*4-subperpixel+1);
```

```

Data = Data(ind,:);

% Creates Distance Vector of the center of each subpixel based on
41 % the total number of subpixels for a single face of the detector
[ThetaRefX0] = SubPixelCenters(subsperpixel,stripwidth,gapwidth,...
    NumSubStrips,0);
[ThetaRefX1] = SubPixelCenters(subsperpixel,stripwidth,gapwidth,...
    NumSubStrips,0);
[ThetaRefY0] = SubPixelCenters(subsperpixel,stripwidth,gapwidth,...
    NumSubStrips,0);
[ThetaRefY1] = SubPixelCenters(subsperpixel,stripwidth,gapwidth,...
    NumSubStrips,0);

46 % Creates Distance Vector that defines the edges of the subpixels
% to be used for the histogram plots
[DetectDistRef] = SubPixelEdges(subsperpixel,stripwidth,gapwidth,...
    NumSubStrips);
DetectDistRef = DetectDistRef(subsperpixel+2:end-(subsperpixel+1))...
    ;

51 DetectDistAvg = (DetectDistRef(2:end)+DetectDistRef(1:end-1))/2;
UsableDetectDist = cell(1,2);
UsableDetectDist{1} = DetectDistRef;
UsableDetectDist{2} = DetectDistRef;

56 % Defines vector with edge bins for the Deviation from
% colinearity of the coincident photons to be used for the
% histogram plots
SubPixelRes = (stripwidth+gapwidth)/subsperpixel/DetectSourceDist;
% % Subpixel Angular not accounting for the 0.25mm gap in [mrad]
61 DevColinRef = min((DetectDistRef-gapwidth/2)/DetectSourceDist)*2:...
    SubPixelRes:max((DetectDistRef+gapwidth/2)/DetectSourceDist)*2;
DevColinEdges = cell(1,2);
DevColinEdges{1} = DevColinRef;
DevColinEdges{2} = DevColinRef;

66 % Load and Format Masked Efficiency Count Matricies
% % one for each detector
load([pwd '/Detector0NormalizedEfficiency.mat']);
load([pwd '/Detector1NormalizedEfficiency.mat']);

71 indr = subsperpixel+1:subsperpixel+1:(subsperpixel+1)*14;
Det0Temp = removerows(Det0Res,indr);
Det0Temp = removerows(Det0Temp',indr)';
Det1Temp = removerows(Det1Res,indr);
Det1Temp = removerows(Det1Temp',indr)';

76 % Load and Format mask file to analyze data
% % if one doesn't exist, then one is created
try
    load([pwd '/DetectorMask_' num2str(subsperpixel) '.mat']);
81 catch
    mask = PHDsMask(size(Det0Res), subsperpixel);

```

```

end
maskTemp = removerows(mask,indr);
maskTemp = removerows(maskTemp',indr)';
86 % Apply Mask to Filter Eff Data
Det0Temp = Det0Temp.*maskTemp;
Det1Temp = Det1Temp.*maskTemp;

91 % Format and Assign relative efficiencies to Coincident events
Det0Eff = zeros(NumSubStrips,NumSubStrips);
Det1Eff = zeros(NumSubStrips,NumSubStrips);
Det0Eff(subsperpixel+1:NumSubStrips-subsperpixel,subsperpixel+1:...
    NumSubStrips-subsperpixel) = Det0Temp;
Det1Eff(subsperpixel+1:NumSubStrips-subsperpixel,subsperpixel+1:...
    NumSubStrips-subsperpixel) = Det1Temp;
96 RelEffs = zeros(size(Data,1),2);
for n = 1:size(Data,1)
    RelEffs(n,1) = Det0Eff(Data(n,2)-NumSubStrips,Data(n,1));
    RelEffs(n,2) = Det1Eff(Data(n,5)-NumSubStrips*3,Data(n,4)-...
        NumSubStrips*2);
end
101 % X-Direction (AC Direction)
% % Positive AC Direction is from Center of either DSSD toward
% % the table, on which the detectors are resting.
XTheta0 = ThetaRefX0(Data(:,1));
106 XTheta1 = ThetaRefX1(Data(:,4)-NumSubStrips*2);
figure('Color','w','OuterPosition',[570 600 600 500]);
subplot(2,1,1);
ncount = histc(XTheta0,DetectDistRef); bar(DetectDistRef, ncount, ...
    'histc');
xlabel('Distance from Center of Crystal, [mm]');
111 ylabel('Counts, [#]');
subplot(2,1,2); ncount = histc(XTheta1,DetectDistRef); bar(...
    DetectDistRef, ncount, 'histc');
%title('Detector1 - VerticalAxis');
xlabel('Distance from Center of Crystal, [mm]');
ylabel('Counts, [#]');
116 figure('Color','w','OuterPosition',[570 600 600 500]);
subplot(2,1,1);
[ncount ncounteff] = hist1dw(XTheta0,DetectDistRef,RelEffs(:,1));
bar(DetectDistAvg,ncounteff,'histc'); %title('Detector0 - ...
    VerticalAxis');
121 xlabel('Distance from Center of Crystal, [mm]');
ylabel('Counts, [#]');
subplot(2,1,2); [ncount ncounteff] = hist1dw(XTheta1,DetectDistRef...
    ,RelEffs(:,2));
bar(DetectDistAvg,ncounteff,'histc'); %title('Detector0 - ...
    VerticalAxis');
xlabel('Distance from Center of Crystal, [mm]');
126 ylabel('Counts, [#]');

```



```

% Y-Direction (DC Direction)
% % Positive DC Direction is from Center of either DSSD toward
% % the table, on which the detectors are resting.
131 YTheta0 = ThetaRefY0(Data(:,2)-NumSubStrips);
YTheta1 = ThetaRefY1(Data(:,5)-NumSubStrips*3);
figure('Color','w','OuterPosition',[570 100 600 500]);
subplot(2,1,1);
ncount = histc(YTheta0,DetectDistRef); bar(DetectDistRef, ncount, ...
    'histc');
136 %title('Detector0 - Beam Axis');
xlabel('Distance from Center of Crystal, [mm]');
ylabel('Counts, [#]');
subplot(2,1,2); ncount = histc(YTheta1,DetectDistRef); bar(...
    DetectDistRef, ncount, 'histc');
%title('Detector1 - Beam Axis');
141 xlabel('Distance from Center of Crystal, [mm]');
ylabel('Counts, [#]');

figure('Color','w','OuterPosition',[570 100 600 500]);
subplot(2,1,1);
146 [ncount ncounteff] = hist1dw(YTheta0,DetectDistRef,RelEfs(:,1));
bar(DetectDistAvg,ncounteff,'histc'); %title('Detector0 - ...
    VerticalAxis');
xlabel('Distance from Center of Crystal, [mm]');
ylabel('Counts, [#]');
subplot(2,1,2); [ncount ncounteff] = hist1dw(YTheta1,DetectDistRef...
    ,RelEfs(:,2));
151 bar(DetectDistAvg,ncounteff,'histc'); %title('Detector0 - ...
    VerticalAxis');
xlabel('Distance from Center of Crystal, [mm]');
ylabel('Counts, [#]');

% % % Coincident Response from the detectors
156 figure('Color','w','OuterPosition',[12 100 560 1000]);
subplot(2,1,1); hist3([XTheta0 YTheta0], [14 14]);
%title('Detector0 - Coincident Response');
shading flat; xlabel('Vertical Axis [mm]'); ylabel('Beam Axis [mm]...
    ');
set(gcf,'renderer','opengl');
161 view(gca,[90 90]);colorbar;axis square;
set(get(gca,'child'),'FaceColor','interp','CDataMode','auto');
subplot(2,1,2); hist3([XTheta1 YTheta1], [14 14]);
%title('Detector1 - Coincident Response');
shading flat; xlabel('Vertical Axis [mm]'); ylabel('Beam Axis [mm]...
    ');
166 set(gcf,'renderer','opengl');
set(get(gca,'child'),'FaceColor','interp','CDataMode','auto');
view(gca,[90 90]); colorbar; axis square;

figure('Color','w','OuterPosition',[12 100 560 1000]);

```

```

171 subplot(2,1,1); hist3([XTheta0 YTheta0], 'Edges',UsableDetectDist)...
    ;
    %title('Detector0 - Coincident Response');
    shading flat; xlabel('Vertical Axis [mm]'); ylabel('Beam Axis [mm]...
        ');
    set(gcf,'renderer','opengl');
    view(gca,[90 90]);colorbar;axis square;
176 set(get(gca,'child'),'FaceColor','interp','CDataMode','auto');
    subplot(2,1,2); hist3([XTheta1 YTheta1], 'Edges', UsableDetectDist...
        );
    %title('Detector1 - Coincident Response');
    shading flat; xlabel('Vertical Axis [mm]'); ylabel('Beam Axis [mm]...
        ');
    set(gcf,'renderer','opengl');
181 set(get(gca,'child'),'FaceColor','interp','CDataMode','auto');
    view(gca,[90 90]); colorbar; axis square;

    Det0 = hist3([XTheta0 YTheta0], 'Edges',UsableDetectDist);
    Det1 = hist3([XTheta1 YTheta1], 'Edges', UsableDetectDist);
186 Det0 = Det0.*mask;
    Det1= Det1.*mask;

    figure('Color','w','OuterPosition',[570 100 560 1000]);
    subplot(2,1,1); pcolor(DetectDistRef,DetectDistRef,Det0);
191 %title('Detector0 - Masked Coincident Response');
    shading flat; xlabel('Vertical Axis [mm]'); ylabel('Beam Axis [mm]...
        ');
    colorbar;axis square;
    caxis([0 35]);
    subplot(2,1,2); pcolor(DetectDistRef,DetectDistRef,Det1);
196 %title('Detector1 - Masked Coincident Response');
    shading flat; xlabel('Vertical Axis [mm]'); ylabel('Beam Axis [mm]...
        ');
    colorbar;axis square;
    caxis([0 35]);

201 figure('Color','w','OuterPosition',[12 100 560 1000]);
    subplot(2,1,1); pcolor(DetectDistRef,DetectDistRef,Det0./Det0Res);
    %title('Detector0 - Coincident Response');
    shading flat; xlabel('Vertical Axis [mm]'); ylabel('Beam Axis [mm]...
        ');
    colorbar;axis square;
206 caxis([0 1.5]);
    subplot(2,1,2); pcolor(DetectDistRef,DetectDistRef,Det1./Det1Res);
    %title('Detector1 - Coincident Response');
    shading flat; xlabel('Vertical Axis [mm]'); ylabel('Beam Axis [mm]...
        ');
    colorbar;axis square;
211 caxis([0 1.5]);

    %% Deviation from Colinearity
    ThetaX = (XTheta0+XTheta1)/DetectSourceDist;

```

```

ThetaY = (YTheta0+YTheta1)/DetectSourceDist;
216 ACARData = [ThetaX ThetaY];

figure('Color','w','OuterPosition',[1170 100 600 500]); subplot...
    (2,1,1);
ncount = histc(ThetaX,DevColinRef); bar(DevColinRef,ncount,'histc'...
    );
%title('Vertical Axis');
221 xlabel('Deviation from Colinearity, [mrad]');
subplot(2,1,2); ncount = histc(ThetaY,DevColinRef); bar(...
    DevColinRef,ncount,'histc');
%title('Horizontal Axis');
xlabel('Deviation from Colinearity, [mrad]');
ylabel('Counts, [#]');
226 figure('Color','w','OuterPosition',[1170 100 600 500]); subplot...
    (2,1,1);
DevColinAvg = (DevColinRef(2:end)+DevColinRef(1:end-1))./2;
[nccount, ncounteff] = hist1dw(ThetaX,DevColinRef,RelEffs(:,1).*...
    RelEffs(:,2)); bar(DevColinAvg,ncounteff,'histc');
%title('Vertical Axis');
231 xlabel('Deviation from Colinearity, [mrad]');
subplot(2,1,2); [nccount, ncounteff]= hist1dw(ThetaY,DevColinRef,...
    RelEffs(:,1).*RelEffs(:,2)); bar(DevColinAvg,ncounteff,'histc')...
    ;
%title('Horizontal Axis');
xlabel('Deviation from Colinearity, [mrad]');
ylabel('Counts, [#]');
236 figure('Color','w','OuterPosition',[1170 600 600 528]);
hist3(ACARData,'Edges',DevColinEdges);
ACARCount = hist3(ACARData,'Edges',DevColinEdges);
%title('ACAR Deviation from Colinearity');
241 shading flat; xlabel('Vertical Axis {\theta} [mrad]'); ylabel('...
    Beam Axis {\theta} [mrad]');
set(gcf,'renderer','opengl');
set(get(gca,'child'),'FaceColor','interp','CDataMode','auto');
view(gca,[90 90]); colorbar; axis square;
caxis([0 15]);
246 [ACARCount2, ACARDatawEff] = hist2dw(ACARData,DevColinRef,...
    DevColinRef,RelEffs);
figure('Color','w','OuterPosition',[1170 600 600 528]);
pcolor(DevColinAvg, DevColinAvg, ACARDatawEff);
shading flat; colorbar; axis square;
251 %title('ACAR Deviation from Colinearity w Efficiency Correction');
xlabel('Vertical Axis {\theta} [mrad]'); ylabel('Beam Axis {\theta...
    } [mrad]');
caxis([0 600]);

ind = find(RelEffs(:,1)~=0 & RelEffs(:,2)~=0);
256 RelEffsFilt = RelEffs(ind,:);

```

```

ACARDataFilt = ACARData(ind,:);
[ACARCount2Filt, ACARDatawEffFilt] = hist2dw(ACARDataFilt,...
    DevColinRef,DevColinRef,RelEffsFilt);
figure('Color','w','OuterPosition',[1170 100 600 500]);
DevColinAvg = (DevColinRef(2:end)+DevColinRef(1:end-1))./2;
261 pcolor(DevColinAvg, DevColinAvg, ACARDatawEffFilt);
shading flat; colorbar; axis square;
%title('ACAR Deviation from Colinearity w Efficiency Correction & ...
    Filtered Pixels');
xlabel('Vertical Axis {\theta} [mrad]'); ylabel('Beam Axis {\theta...
    } [mrad]');
caxis([0 600]);
266 %% CDBAR Calculation
EnergyRes = 0.1;

Evec = (EwinCent-deltaE):EnergyRes:(EwinCent+deltaE);
EvecAvg = (Evec(2:end)+Evec(1:end-1))./2;
271 EvecCell = cell(1,2);
EvecCell{1} = Evec;
EvecCell{2} = Evec;
DBARData = [Data(:,3) Data(:,6)];

276 figure('Color','w','OuterPosition',[1770 100 600 500]);
subplot(2,1,1);
ncount = histc(Data(:,3),Evec); bar(Evec,ncount,'histc');
%title('Detector0 - Energy Plot');
xlabel('Energy, [keV]');
281 ylabel('Counts, [#]');
subplot(2,1,2);
ncount = histc(Data(:,6),Evec); bar(Evec,ncount,'histc');
%title('Detector1 - Energy Plot');
xlabel('Energy, [keV]');
286 ylabel('Counts, [#]');

figure('Color','w','OuterPosition',[1770 100 600 500]);
subplot(2,1,1);
[ncount, ncounteff] = hist1dw(Data(:,3),Evec,RelEffs(:,1)); bar(...
    EvecAvg,ncounteff,'histc');
291 %title('Detector0 - Energy Plot');
xlabel('Energy, [keV]');
ylabel('Counts, [#]');
subplot(2,1,2);
[ncount, ncounteff] = hist1dw(Data(:,6),Evec,RelEffs(:,1)); bar(...
    EvecAvg,ncounteff,'histc');
296 %title('Detector1 - Energy Plot');
xlabel('Energy, [keV]');
ylabel('Counts, [#]');

figure('Color','w','OuterPosition',[1770 600 600 528]);
301 hist3(DBARData, EvecCell);
xlabel('Energy Detector 0 [keV]'); ylabel('Energy Detector 1 [keV]...
    ');

```

```

set(gcf,'renderer','opengl'); shading flat;
set(get(gca,'child'),'FaceColor','interp','CDataMode','auto');
view(gca,[90.5 90]); colorbar; axis square;
306 caxis([0 8]);

[DBARCount, DBARDatawEff] = hist2dw(DBARData, Evec, Evec,RelEffs);
figure('Color','w','OuterPosition',[1770 600 600 528]);
pcolor(EvecAvg,EvecAvg,DBARDatawEff); shading flat; colorbar;
311 shading flat; colorbar; axis square;
%title('DBAR Energy Plot w Efficiency Correction');
xlabel('Energy Detector 0 [keV]'); ylabel('Energy Detector 1 [keV]...
');
caxis([0 1000]);

316 DBARDataFilt = DBARData(ind,:);
[DBARCount2Filt, ACARDatawEffFilt] = hist2dw(DBARDataFilt,Evec, ...
Evec,RelEffsFilt);
figure('Color','w','OuterPosition',[1770 100 600 500]);
pcolor(EvecAvg,EvecAvg,DBARDatawEff); shading flat; colorbar;
shading flat; colorbar; axis square;
321 %title('DBAR Energy Plot w Efficiency Correction & Filterd Pixels...
');
xlabel('Energy Detector 0 [keV]'); ylabel('Energy Detector 1 [keV]...
');
caxis([0 1000]);

delta = 0.4;

326 DBARDataFilt(:,3) = RelEffsFilt(:,1).*RelEffsFilt(:,2);
DBARDataFilt(:,4) = DBARDataFilt(:,1)+DBARDataFilt(:,2)-1022;
DBARDataFilt(:,5) = DBARDataFilt(:,1)-DBARDataFilt(:,2);
indE = find(DBARDataFilt(:,4)>=-delta & DBARDataFilt(:,4)<=delta);
331 DBARDataEFilt = DBARDataFilt(indE,:);

EvecLine = Evec-511;
[DBARCountLine, DBARCountLinewEff] = hist1dw(DBARDataEFilt(:,5),...
EvecLine,DBARDataEFilt(:,3));
EvecLine = (EvecLine(2:end)+EvecLine(1:end-1))/2;
336 figure('Color','w','OuterPosition',[1770 600 600 528]);
semilogy(EvecLine,DBARCountLine,'-k',EvecLine,DBARCountLinewEff,'-...
b');
axis([min(EvecLine) max(EvecLine) 0 1000]);
ylabel('Counts'); xlabel('Difference in Energy, [keV]');

341 end

```

```

%%% Calculates Distances from center of PHDs DSSD to center of
%%% subpixels
%%% Created on 12 Dec 2011 by smj
4
function [DorTRef] = SubPixelEdges(sppixel,stripwidth,gapwidth,...
numpixels)

```

```

% % User Inputs
% sppixel - Number of subpixels per pixel
% stripwidth - strip width of the PHDs Detectors in mm.
9 %           Should be 4.75
% gapwidth - gap width of the PHDs Detectors in mm.
%           Should be 0.25
% numpixels - total number of pixels in one dimension of the
%           PHDs detector. Should be 16*substrips per strip.
14 substripwidth = stripwidth/sppixel;

% Create positive half of the vector then negative half and
% combine.
19 basis(1) = 0;
for j = 2:sppixel+1
    basis(j) = substripwidth*(j-1);
end
basis = basis + gapwidth/2;
24 DorTRef = [];
for n = 1:(numpixels/sppixel/2)
    DorTRef = [DorTRef basis+(n-1)*5];
end
29 DorTRef = sort([-1*DorTRef DorTRef])';

end

```

```

%%% Calculates Distances from center of PHDs DSSD to center of
%%% subpixels
%%% Created on 12 Dec 2011 by smj
4
function [DorTRef] = SubPixelCenters(sppixel,stripwidth,gapwidth,...
    numpixels,offset)
% % User Inputs
% sppixel - Number of subpixels per pixel
% stripwidth - strip width of the PHDs Detectors in mm.
9 %           Should be 4.75
% gapwidth - gap width of the PHDs Detectors in mm.
%           Should be 0.25
% numpixels - total number of pixels in one dimension of the
%           PHDs detector. Should be 16*substrips per strip.
14 % offset - Allows for the centers to be offset if need be.

% Constants
substripwidth = stripwidth/sppixel;

19 % % METHOD ONE
% % Create pos-half of the vector then neg-half and combine.

distance2 = zeros(1,numpixels/2);
distance2(1) = (gapwidth + substripwidth)/2;
24 for i = 2:numpixels/2

```

```

    if (mod(i-1,sppixel)==0)
        distance2(i) = distance2(i-1)+substripwidth+gapwidth;
    else
29     distance2(i) = distance2(i-1)+substripwidth;
    end
end
distance1 = -distance2;
DorTRef = [sort(distance1) distance2]';
DorTRef = DorTRef + offset;
34 clear distance1 distance2
DorTRef = roundn(DorTRef,-3);

%% METHOD TWO
%% Create vector linearly then subtract half of detector width.
39
% HalfDetectorWidth = (stripwidth*16 + gapwidth*15)/2;
% distance = zeros(1,numpixels);
% distance(1) = substripwidth/2;
% for i = 2:numpixels
44 %     if (mod(i-1,sppixel)==0)
%         distance(i) = distance(i-1)+substripwidth+gapwidth;
%     else
%         distance(i) = distance(i-1)+substripwidth;
%     end
49 % end
%
% distance = (distance - HalfDetectorWidth)';
% clear HalfDetectorWidth
% distance = round(distance*10000)/10000;
54 end

```

```

1 % A simple function to create a bivariate weighted histogram
%% Created on 29 Jan 2011 by smj

function [count, wcount] = hist2dw(data, xedges, yedges, weights);
% User Inputs
6 % data - matrix of two columns of x and y values
% xedges - edges of bins desired for x column
% yedges - edges of bins desired for y column
% weights - weights for each x & y pair in data
%
11 % Outputs
% count - unweighted histogram
% wcount - weighted histogram
for i = 1:length(xedges)-1;
    data((data(:,1)>xedges(i))&(data(:,1)<=xedges(i+1)),3)=i;
16 end

for i = 1:length(yedges)-1;
    data((data(:,2)>yedges(i))&(data(:,2)<=yedges(i+1)),4)=i;
end
21

```

```

count = zeros(length(xedges)-1,length(yedges)-1);
wcount = zeros(length(xedges)-1,length(yedges)-1);

26 data = data(data(:,3)>0,:);
data = data(data(:,4)>0,:);

for i = 1:size(data,1)
    wcount(data(i,3),data(i,4))=wcount(data(i,3),data(i,4))+(1/...
        weights(i,1)/weights(i,2));
    count(data(i,3),data(i,4))=count(data(i,3),data(i,4))+1;
31 end

end

```

```

1 % A simple function to create a bivariate weighted histogram
%% Created on 29 Jan 2011 by smj

function [count, wcount] = hist1dw(data, xedges, weights)
% % User Inputs
6 % data - matrix of one column of x values
% xedges - edges of bins desired for x column
% weight - weight for each x in data
%
% % Outputs
11 % count - unweighted histogram
% wcount - weighted histogram
for i = 1:length(xedges)-1;
    data((data(:,1)>xedges(i))&(data(:,1)<=xedges(i+1)),2)=i;
end
16
count = zeros(length(xedges)-1,1);
wcount = zeros(length(xedges)-1,1);

data = data(data(:,2)>0,:);
21
for i = 1:size(data,1)
    wcount(data(i,2),1)=wcount(data(i,2),1)+(1/weights(i));
    count(data(i,2),1)=count(data(i,2),1)+1;
end
26
end

```



## Bibliography

- [1] Ache, Hans J. “New Developments in Positron and Positronium Chemistry”. *Positron Annihilation*, Proceedings of the fifth international conference on positron annihilation, 31–47. Japan Institute of Metals, 1979.
- [2] Adamson, Paul E. *Quantum Mechanical Prediction of Experimental Observables of Positron-Vacancy Complexes in Silicon Carbide*. Ph.D. thesis, Air Force Institute of Technology, 2005.
- [3] Anderson, Carl D. “The Positive Electron”, 1933.
- [4] Baranowski, A., J. Beliczynski, M. Kostrzewa, and M. Szuszkiewicz. “A two-detector spectrometer for measurements of Doppler broadened positron annihilation spectra”. *Nuclear Instruments and Methods in Physics Research Section A: Accelerators, Spectrometers, Detectors and Associated Equipment*, 526(3):420–431, 2004.
- [5] Biasini, M., J. Ruzs, and AP Mills Jr. “Positron annihilation study of the electronic structure of URu<sub>2</sub>Si<sub>2</sub>: Fermi surface and hidden order parameter”. *Physical Review B*, 79(8):085115, 2009.
- [6] Brant, AT, BE Kananan, MK Murari, JW McClory, JC Petrosky, VT Adamiv, Y. V. Burak, PA Dowben, and LE Halliburton. “Electron and hole traps in Ag-doped lithium tetraborate (Li<sub>2</sub>B<sub>4</sub>O<sub>7</sub>) crystals”. *Journal of Applied Physics*, 110(9):093719–093719–7, 2011.
- [7] Chehab, R. “Positron sources”. *CERN EUROPEAN ORGANIZATION FOR NUCLEAR RESEARCH-REPORTS-CERN*, 643–643, 1994.
- [8] Coleman, P. G. *Positron beams and their applications*. World Scientific Pub Co Inc, 2000.
- [9] Dirac, Paul A. M. “The Quantum Theory of the Electron”. *Proceedings of the Royal Society of London. Series A, Containing Papers of a Mathematical and Physical Character*, 117:610–24, 1928.
- [10] Firestone, R. B. *Nuclear Data Sheets for A=22*. Technical report, Lawrence Berkeley National Laboratory, 2005.
- [11] Greaves, R. G. “Positron Probes”. URL [http://www.firstpsi.com/PBT\\_detail.htm](http://www.firstpsi.com/PBT_detail.htm).
- [12] Greaves, R. G. *The creation of high quality positron beams using traps*, 2002.
- [13] Greaves, R. G. and J. M. Moxom. “Compression of trapped positrons in a single particle regime by a rotating electric field”. *Physics of Plasmas*, 15:072304, 2008.

- [14] Greaves, R. G. and C. M. Surko. “Technological applications of trapped positrons”. *AIP Conference Proceedings*, 19–28. IOP INSTITUTE OF PHYSICS PUBLISHING LTD, 1999.
- [15] Gribakin, G. F., J. A. Young, and C. M. Surko. “Positron-molecule interactions: Resonant attachment, annihilation, and bound states”. *Reviews of Modern Physics*, 82(3):2557, 2010.
- [16] Hasiguti, R. R. and K. Fujiwara (editors). *Positron Annihilation*. The Japan Institute of Metals, The Japan Institute of Metals, April 1979.
- [17] Krause-Rehberg, R. “Design of a positron source to be used in ultra-high vacuum”. URL <http://positron.physik.uni-halle.de/source.html>.
- [18] Krause-Rehberg, Reinhard and Hartmut S. Leipner. *Positron Annihilation in Semiconductors*. Springer, 1999.
- [19] Ore, A. and J. L. Powell. “Three-photon annihilation of an electron-positron pair”. *Physical Review*, 75(11):1696, 1949.
- [20] Rozing, GJ, PE Mijnaerends, AA Menovsky, and PF de Chtel. “Positron-annihilation study of the electronic structure of URu<sub>2</sub>Si<sub>2</sub>”. *Physical Review B*, 43(12):9523, 1991.
- [21] Shkolnikov, PL, AE Kaplan, A. Pukhov, and J. Meyer ter Vehn. “Positron and gamma-photon production and nuclear reactions in cascade processes initiated by a sub-terawatt femtosecond laser”. *Applied Physics Letters*, 71:3471, 1997.
- [22] Stevenson, A. W. *Improving the Efficiency of Photon Collection By Compton Rescue*. Master’s thesis, 2011.
- [23] Surko, C. M. “Buffer Gas Trapping”. URL <http://positrons.ucsd.edu/positronframe.html>.
- [24] Surko, C. M. “Accumulation, Storage and Manipulation of Large Numbers of Positrons in Traps I. The Basics”. 511. 2010.
- [25] Surko, C. M. “Accumulation, Storage and Manipulation of Large Numbers of Positrons in Traps II. Selected Topics”. 556. 2010.
- [26] Surko, C. M. and R. G. Greaves. “Emerging science and technology of antimatter plasmas and trap-based beams”. *Physics of Plasmas*, 11:2333, 2004.
- [27] Swinney, MW, JW McClory, JC Petrosky, S. Yang, AT Brant, VT Adamiv, Y. V. Burak, PA Dowben, and LE Halliburton. “Identification of electron and hole traps in lithium tetraborate (Li<sub>2</sub>B<sub>4</sub>O<sub>7</sub>) crystals: Oxygen vacancies and lithium vacancies”. *Journal of Applied Physics*, 107(11):113715–113715–9, 2010.

- [28] Uedono, A. et al. “Vacancy-Type Defects in Ultra-Shallow Junctions Fabricated Using Plasma Doping Studied by Positron Annihilation”. *10th International Workshop on Junction Technology, IWJT-2010*, 149–154. 2010.
- [29] Walker, A. C. *Positron Annihilation Ratio Spectroscopy Study of Electric Fields Applied to Positronium at Material Interfaces*. Master’s thesis, 2011.
- [30] Williams, C. S. “Three Dimensional Positron Annihilation Momentum Measurement Technique Applied to Measure Oxygen-Atom Defects in 6H Silicon Carbide”. 2010.
- [31] Y. C. Jean, P. E. Mallon and D. M. Schrader. *Principles and Applications of Positron and Positronium Chemistry*. World Scientific, 2003.

## Vita

Capt Stephen Jiménez was born in Pueblo, Colorado and raised in Trinidad, Colorado. After graduating as the valedictorian from Trinidad Catholic High School, he attended college at the United States Air Force Academy in Colorado Springs, Colorado. He graduated as a distinguished graduate with his Bachelor's Degree in Mathematical Sciences and Physics and was commissioned into the United States Air Force in May of 2006. Following graduation, he was assigned to the Space Vehicles Directorate of the Air Force Research Laboratory (AFRL/RVB) at Hanscom AFB, Massachusetts, where he studied ionospheric hazards on Air Force systems. Following his assignment at AFRL, he entered graduate school at the Air Force Institute of Technology (AFIT) in August of 2010 and he is currently completing his Master's Degree in Nuclear Engineering. His anticipated follow-on assignment is to the Air Force Technical Applications Center (AFTAC) at Patrick AFB.

# REPORT DOCUMENTATION PAGE

Form Approved  
OMB No. 0704-0188

The public reporting burden for this collection of information is estimated to average 1 hour per response, including the time for reviewing instructions, searching existing data sources, gathering and maintaining the data needed, and completing and reviewing the collection of information. Send comments regarding this burden estimate or any other aspect of this collection of information, including suggestions for reducing this burden to Department of Defense, Washington Headquarters Services, Directorate for Information Operations and Reports (0704-0188), 1215 Jefferson Davis Highway, Suite 1204, Arlington, VA 22202-4302. Respondents should be aware that notwithstanding any other provision of law, no person shall be subject to any penalty for failing to comply with a collection of information if it does not display a currently valid OMB control number. **PLEASE DO NOT RETURN YOUR FORM TO THE ABOVE ADDRESS.**

<b>1. REPORT DATE (DD-MM-YYYY)</b> 22-03-2012		<b>2. REPORT TYPE</b> Master's Thesis		<b>3. DATES COVERED (From — To)</b> Aug 2010 — Mar 2012	
<b>4. TITLE AND SUBTITLE</b>  Design and Characterization of a Three-Dimensional Positron Annihilation Spectroscopy System Using a Low-Energy Positron Beam				<b>5a. CONTRACT NUMBER</b>	
				<b>5b. GRANT NUMBER</b>	
				<b>5c. PROGRAM ELEMENT NUMBER</b>	
				<b>5d. PROJECT NUMBER</b>	
				<b>5e. TASK NUMBER</b>	
<b>6. AUTHOR(S)</b>  Jiménez, Stephen M., Capt, USAF				<b>5f. WORK UNIT NUMBER</b>	
<b>7. PERFORMING ORGANIZATION NAME(S) AND ADDRESS(ES)</b> Air Force Institute of Technology Graduate School of Engineering and Management (AFIT/EN) 2950 Hobson Way WPAFB OH 45433-7765				<b>8. PERFORMING ORGANIZATION REPORT NUMBER</b>  AFIT/NUCL/ENP/12-M04	
<b>9. SPONSORING / MONITORING AGENCY NAME(S) AND ADDRESS(ES)</b> AFOSR/RSA (Dr. Michael R. Berman) 875 North Randolph Street, Room 3112 Arlington VA 22203 Tele: (703)696-7781, DSN: 426-7781, FAX: (703)696-7320, michael.berman@afosr.af.mil				<b>10. SPONSOR/MONITOR'S ACRONYM(S)</b> AFOSR/MOA	
				<b>11. SPONSOR/MONITOR'S REPORT NUMBER(S)</b>	
<b>12. DISTRIBUTION / AVAILABILITY STATEMENT</b>  DISTRIBUTION STATEMENT A. APPROVED FOR PUBLIC RELEASE; DISTRIBUTION UNLIMITED.					
<b>13. SUPPLEMENTARY NOTES</b>					
<b>14. ABSTRACT</b> Previous forays by AFIT into positron research have resulted in the development of a new positron annihilation spectroscopy (PAS) technique and the procurement of a low-energy positron beam system. The primary purpose of this research was to design and build a state-of-the-art PAS laboratory at AFIT capable to address a myriad of DoD solid-state and surface physics questions. The main objectives were to acquire and assemble utilities to operate a positron beam, assemble and configure an ultra-high vacuum (UHV) system for samples, design and build an interface with a magnetic field to propagate positrons onto samples, and create a new version of the three-dimensional positron annihilation spectroscopy system (3DPASS). The 3DPASS, which measures coincidence Doppler broadening of annihilation radiation (CDBAR) and two-dimensional angular correlation of annihilation radiation (2D-ACAR), was characterized using a Cu- <sup>22</sup> Na positron annihilation source made as part of this project. Integration of the 3DPASS with low-energy positron beam will allow for energy-dependent, nondestructive characterization of materials using PAS.					
<b>15. SUBJECT TERMS</b> positron, positron annihilation spectroscopy, angular correlation of annihilation radiation, Doppler broadening of annihilation radiation, low-energy positron beam, three-dimensional positron annihilation momentum measurement					
<b>16. SECURITY CLASSIFICATION OF:</b>			<b>17. LIMITATION OF ABSTRACT</b>	<b>18. NUMBER OF PAGES</b>	<b>19a. NAME OF RESPONSIBLE PERSON</b>
<b>a. REPORT</b>	<b>b. ABSTRACT</b>	<b>c. THIS PAGE</b>			Dr. Larry W. Burggraf
U	U	U	SAR	131	<b>19b. TELEPHONE NUMBER (include area code)</b> (937) 255-3636, x4507; larry.burggraf@afit.edu